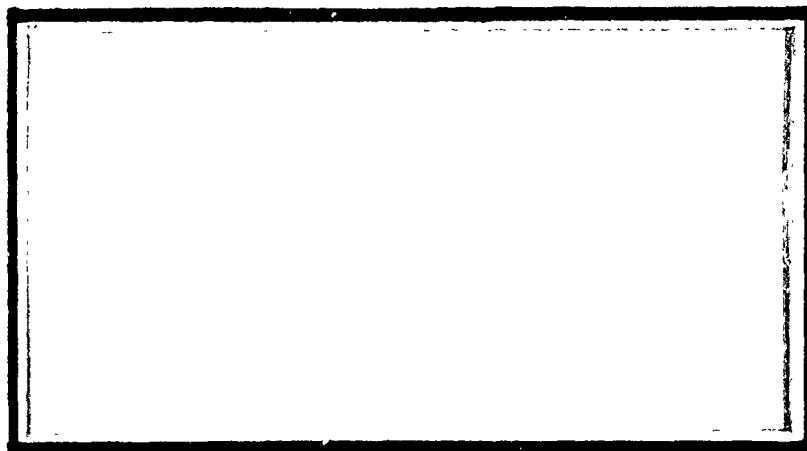
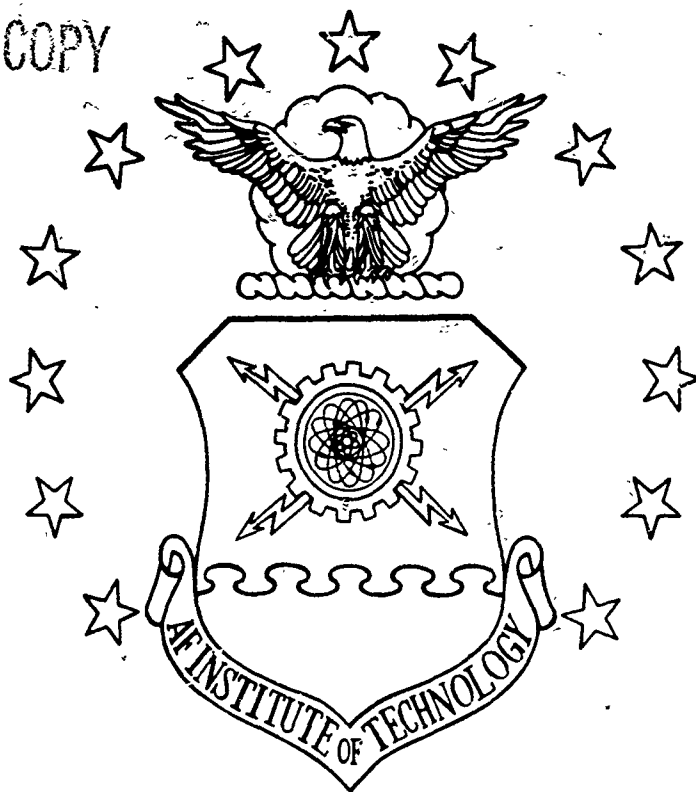


DTIC FILE COPY

AD-A230 388



DTIC  
 ELECTE  
 JAN 08 1991  
 S E D

DEPARTMENT OF THE AIR FORCE  
 AIR UNIVERSITY

**AIR FORCE INSTITUTE OF TECHNOLOGY**

Wright-Patterson Air Force Base, Ohio

DISTRIBUTION STATEMENT A  
 Approved for public release  
 Distribution Unlimited

91 1 3 149

AFIT/GAE/ENY/90D-20

INVESTIGATION OF FATIGUE DAMAGE  
MECHANISMS IN A METAL MATRIX COMPOSITE  
UNDER ELEVATED TEMPERATURE

THESIS

Barry D. Portner  
Captain, USAF

AFIT/GAE/ENY/90D-20

DTIC  
JAN 03 1991

Approved for public release; distribution unlimited

AFIT/GAE/ENY/90D-20

INVESTIGATION OF FATIGUE DAMAGE  
MECHANISMS IN A METAL MATRIX COMPOSITE  
UNDER ELEVATED TEMPERATURE

THESIS

Presented to the Faculty of the School of Engineering  
of the Air Force Institute of Technology

Air University

In Partial Fulfillment of the  
Requirements for the Degree of  
Master of Science in Aeronautical Engineering

Barry D. Portner, B.S.

Captain, USAF

December 1990

Accession For	
NTIS GRA&I	<input checked="" type="checkbox"/>
DTIC TAB	<input type="checkbox"/>
Unannounced	<input type="checkbox"/>
Justification	
By _____	
Distribution/	
Availability Codes	
Dist	Avail and/or Special
A-1	

Approved for public release; distribution unlimited



## *Preface*

Structural performance uncertainties are becoming more critical as we design systems to operate at higher speeds inducing aerodynamic heating and increased stresses. The metal-matrix composites are the alternatives over metals for these applications requiring superior strength, stiffness, and heat resistance. Full design advantages would be gained by a thorough understanding of the behavior of this classification of composites under various environmental conditions. Presently, these studies are limited.

The focus of this study was towards the thorough understanding of fatigue damage mechanisms in the titanium matrix fiber reinforced composite, SCS6/Ti-15-3, at elevated temperatures. Of course, the results of this study is only a small part of the total which will be required to fully characterize this material.

I am indebted to many for helping to make this study more complete than I initially projected. Dr. Mall, my thesis adviser, provided invaluable guidance along the way. Jay Anderson and the other Aero Lab technicians always jumped in to help during a crisis. Mr. Fecke of the Propulsion Lab sponsored this study. Many others in the Materials Labs provided answers to questions which aren't in text books. Most importantly, my wife, who took over many of my family duties so that I could complete this study.

Barry D. Portner

*Table of Contents*

Preface . . . . .	i
List of Figures . . . . .	iii
List of Tables . . . . .	viii
Abstract . . . . .	ix
I. Introduction . . . . .	1
II. Fatigue Testing of Metal Matrix Composites . . . . .	6
III. Experimental Procedures . . . . .	14
Materials . . . . .	14
Specimens . . . . .	15
Fatigue Testing Procedure . . . . .	15
IV. Results and Discussion . . . . .	25
Cycles to Failure . . . . .	25
Tensile Tests . . . . .	28
Evaluation Results . . . . .	32
Strain to Failure . . . . .	61
Average Strain . . . . .	69
Strain Range . . . . .	71
Modulus Curves . . . . .	71
Modulus Degradation as Fatigue Damage . . . . .	82
V. Conclusions and Recommendations . . . . .	89
Appendix A:	
Sectioned Surface Crack Patterns . . . . .	92
Bibliography . . . . .	100
Vita . . . . .	102

*List of Figures*

Figure 1. Block Diagram of the Test Setup . . . . .	16
Figure 2. Thermocouple and Heater Placement Diagram . . . . .	18
Figure 3. Lamp Heater Mounting Arrangement . . . . .	21
Figure 4. Specimen Dimensions & Locations of Periodic Evaluations . . . . .	22
Figure 5. Specimen Sectioning for Micrographic Evaluation . . . . .	23
Figure 6. Fatigue Test Procedures . . . . .	24
Figure 7. Time to Failure . . . . .	26
Figure 8. Cycles to Failure . . . . .	26
Figure 9. Cycles to Failure . . . . .	27
Figure 10. Cycles to Failure . . . . .	28
Figure 11. Tensile Tests at Ambient and 427°C . . . . .	30
Figure 12. Yield Point at the Point of Nonrecoverable Strain. . . . .	31
Figure 13. Locations of Crack Initiation Points . . . . .	34
Figure 14. Fiber-matrix Initiated Cracks Coalescing about a Fiber (375 MPa 0.0208 CPS @ 42,000 cycles) . . . . .	37
Figure 15. Transverse Cracking Between 90° Fibers and to 0° fibers. (375 MPa 0.0208 CPS, 42,000 cycles)	37
Figure 16. Fracture Surface of the 2.0 cps, 375 MPa Specimen . . . . .	38

Figure 17. Matrix Crack Initiating at the 90° Fiber- Matrix Interface Then Propagating to the Surface. (Magnification of Figure 16, Center) . . . . .	38
Figure 18. Coalescing of 0° and 90° Fiber Interface Initiated Cracks. (500 MPa 0.0208 CPS) . . . . .	40
Figure 19. Transverse and Longitudinal Cracking Between 0° and 90° Fibers. (438 MPa 0.0208 CPS) . . . . .	40
Figure 20. Coalescing of 0° and 90° Fiber Initiated Cracks. (542 MPa 0.0208 CPS) . . . . .	42
Figure 21. Inner Ply Cracks Coalescing and Debonding of 90° Fiber-matrix Interface. (438 MPa 0.0208 CPS) . . . . .	42
Figure 22. 90° Fiber-matrix Interface Separation. (438 MPa 0.0208 CPS) . . . . .	43
Figure 23. Transverse Matrix Cracks Initiated off the 0° Reaction Zone. (542 MPa 0.0208 CPS) . . . . .	43
Figure 24. Frequency of Crack Initiation and Fiber Damage. . . . .	44
Figure 25. Crack Propagating From Inner Carbon Core of 0° Fiber. (500 MPa 2.0 CPS) . . . . .	46
Figure 26. Crack Propagating From Inner Carbon Core of 90° Fiber to Titanium Matrix. (500 MPa 2.0 CPS) . . . . .	46
Figure 27. Magnification of Figure 26 (Bottom). (500 MPa 2.0 CPS) . . . . .	48
Figure 28. Cleavage Fracture of Matrix in the Brittle Mode. (375 MPa 2.0 CPS) . . . . .	48

Figure 29. Magnification of Figure 28 (Center). (375 MPa 2.0 CPS) . . . . .	49
Figure 30. Matrix Necking (Plastic Deformation) Due to Fractured Fibers . . . . .	51
Figure 31. Failure Due to Ductile Void Coalescence. (500 MPa 0.0208 CPS) . . . . .	51
Figure 32. Fracture Surface of 427°C Tensile Tested Specimen . . . . .	53
Figure 33. Magnification of Figure 32. Failure by Ductile Void Coalescence. . . . .	53
Figure 34. Fracture Surface of Specimen Tensile Tested at Room Temperature . . . . .	55
Figure 35. Magnification of Figure 34. Failure by Ductile Void Coalescence. . . . .	55
Figure 36. Matrix Crack Propagating to the Left of the Center 90° Fiber (438 MPa 2.0 CPS at 7500 Cycles) . . . . .	57
Figure 37. Crack Progressed Across the Inner 90° Fibers to Both Inner 0° Fibers (438 MPa 2.0 CPS at 10,000 Cycles) . . . . .	57
Figure 38. Damaged Fiber-Matrix Interface Zone. 90° Fibers Debonding with Matrix (438 MPa 2.0 CPS at 12,500 Cycles) . . . . .	59
Figure 39. Edge at Final Fracture at 13,300 Cycles. Compare Fracture with Cracks on Figures 36 through 38 (438 MPa 2.0 CPS) . . . . .	59

Figure 40. Micrograph of a 90° Fiber Cross-Section with Etched Surface Revealing Reaction Zone (500 MPa 2.0 CPS) . . . . .	60
Figure 41. Magnification of Figure 40. Damaged Reaction Zone in the Region of the Crack . . . . .	60
Figure 42. Micrograph of the 0° Fiber Reaction Zone of the Low Frequency 542 MPa Specimen Exposed to Temperature for 3 Hours . . . . .	63
Figure 43. Magnification of Figure 42 (upper right) . . . . .	63
Figure 44. Micrograph of the 90° Fiber-Reaction Zone of the Low Frequency 438 MPa Specimen Exposed to Temperature for 10 Hours . . . . .	64
Figure 45. Reaction Zone Sizes Increase with Increasing Exposure to Temperature . . . . .	64
Figure 46. Maximum Strain to Failure . . . . .	65
Figure 47. Average Strain . . . . .	70
Figure 48. Strain Range . . . . .	72
Figure 49. Changing Modulus Over Cycles . . . . .	74
Figure 50. Changing Modulus Over Time . . . . .	75
Figure 51. Factors Influencing Modulus Behavior . . . . .	77
Figure 52. Creep Response of the Ti-15-3 Matrix material (12:92) . . . . .	78
Figure 53. Dominant Influences on the Modulus Over the Life of the 375 MPa Specimen . . . . .	80
Figure 54. Modulus Curves with Age Hardening Eliminated as a Variable . . . . .	83

Figure 55 Modulus Curves with Age Hardening Eliminated as a Variable . . . . .	84
Figure 56. Specimen Fatigue Damage . . . . .	85
Figure 57. Specimen Fatigue Damage . . . . .	86
Figure 58. Specimen Fatigue Damage Based on Percent Life . . . . .	87

*List of Tables*

Table I. Test Plan	20
Table II. Fatigue Tests Failure Summary	29
Table III. Incidence of Crack Initiation Points and Fiber Damage Locations	35
Table IV. Matrix Failure Modes	54
Table V. Fiber-Matrix Reaction Zone Sizes of Selected Specimens	62

### *Abstract*

This past decade has seen a large growth in interest of superior strength, high temperature, and light weight applications for metal matrix composites. One such type of composite, the titanium matrix fiber reinforced composite, SCS-6/Ti-15-3, is a candidate material which is light weight and excellent for high strength use. However, the ability of this particular composite to maintain strength at elevated temperatures needs to be more fully characterized.

The objective of this study was to investigate the fatigue damage initiation and progression in SCS-6/Ti-15-3 under an environment of fatigue loading at isothermal temperature. This program included two parts. First, an 808 Ultimate Tensile Strength system was set up to accommodate testing at two frequencies of 2.0 and 0.0208 cps at a constant temperature of 427°C. Second, at intervals during the load cycle process, the test specimens were characterized by establishing damage parameters based on changing modulus of elasticity, average strain, strain range, and ultimate tensile strength. Damage progression was documented in the form of failure of the fiber-matrix interface, matrix cracking, fiber breaking, and debonding of the fiber-matrix interface.

Crack initiation locations and growth patterns were peculiar to specific test conditions of frequency and stress level. Also, analysis of the fatigued specimens and test

data revealed matrix failure mechanisms ranging from ductile failure to cleavage fracture. The results of this study clearly show that temperature, frequency as well as stress levels are important design considerations for this composite in fatigue loading applications.

INVESTIGATION OF FATIGUE DAMAGE  
MECHANISMS IN A METAL MATRIX COMPOSITE  
UNDER ELEVATED TEMPERATURE

*I. Introduction*

As aircraft technology advances toward hypersonic flight, aerodynamic heating becomes a crucial issue in the design of the airfoil surfaces as well as structural and engine components. Materials are required that are lightweight and high strength at elevated temperatures. For many years, nickel alloys were the major consideration under study for use on high speed flight construction. These alloys have the ability to maintain their strength at high temperatures but are extremely dense.

The National Aerospace Plane (NASP) program has expended major efforts to develop advanced lightweight materials (1:37-39). One group of lightweight materials being studied is the titanium aluminides which are processed into a metal powder for hot press forming. These titanium aluminide materials sustain moderate strengths at temperatures of 1000°C.

Other advanced materials under development by the NASP program include carbon-carbon composites and metal matrix composites. The carbon-carbon composites feature carbon

fibers embedded in a carbon matrix. These composites resist temperatures up to 1900°C. The metal-matrix composites are made of high strength, low weight fibers such as carbon, boron, or silicon carbide embedded in a metal matrix material.

The titanium metal matrix fiber reinforced composite, SCS6/Ti-15-3 is a candidate material for applications which require high strength, light weight structures in a potentially high temperature environment. This particular composite is presently being considered for high strength, high temperature structural and engine component applications on the National Aerospace Plane and the Advanced Tactical Fighter.

Several studies have been done to characterize the isothermal fatigue behavior of this material. Gayda, Gabb, and Freed have investigated the fatigue behavior of unidirectional composites at constant temperatures of 300°C and 550°C (2:1). Castelli, Ellis, and Bartolotta performed isothermal fatigue tests at 427°C on unidirectional composites (3:1-7). They also investigated fatigue damage of this composite by way of fracture surface evaluation and metallographic examination. Majumdar and Newaz conducted isothermal fatigue tests at 650°C of a [0/±45/90], lay-up composite. In this study, microscopic replica techniques of the test specimen edges were used to document fatigue damage mechanisms (4:2-18). In a more recent study, Pollock and

Johnson performed fatigue tests on  $[0/90]_2$ ,  $[0/\pm 45/90]_2$ ,  $[0_2/\pm 45]$ , and  $[0]_2$  lay-ups at  $650^\circ\text{C}$  at a frequency of 10.0 cps. In this study, fracture surface analysis was conducted to determine fatigue damage mechanisms (5:2).

Consequently, studies of the fatigue behavior of the  $[0/90]_2$  lay-up at isothermal temperatures is extremely limited. The isothermal fatigue behavior of this composite needs to be more fully understood before this material is used in critical component applications on high performance vehicles. Specifically, fatigue damage mechanisms of SCS6/Ti-15-3 need to be characterized at a temperature of  $427^\circ\text{C}$  since its use is anticipated at this temperature.

This study investigated, in a systematic way, the initiation and progression of fatigue damage mechanisms in an 8 ply  $[0/90]_2$  SCS6/Ti-15V-3Cr-3Al-3Sn laminate subjected to fatigue loading at an isothermal temperature of  $427^\circ\text{C}$ . Ten specimens were selected for this purpose. Two specimens were tensile tested: one at ambient temperature, the other at  $427^\circ\text{C}$ . The 8 other specimens were fatigue tested. Four of these specimens were fatigue cycled at a high frequency of 2.0 cps to induce fatigue damage. The other 4 specimens were fatigue cycled at a low frequency of 0.0208 cps to determine thermal effects of the material due to longer exposure times to temperature and compare damage modes with the high frequency specimens. (Hereafter, 2.0 cps will be referred to as high frequency and 0.0208 cps will be referred to as low

frequency.)

The other test parameter to be considered was maximum stress levels for each specimen. Here, low stress levels below the matrix yield point were chosen to reveal matrix characteristics such as age hardening, creep, and strain hardening of the titanium matrix material. They were also selected to characterize matrix crack initiation and progression. Minimum fiber damage was expected at low stresses. The low stress levels selected were 375 and 438 MPa and will here after be referred to as the low stress tests. High stress levels were selected to characterize fiber damage and matrix damage caused by fractured fibers. The stress levels chosen for the high stress tests were 500, 542, and 625 MPa and will be referred to as the high stress tests. To compare frequency effects, specimens of both frequency groups were tested at 375, 438, and 500 MPa.

During the tests the behavior of the specimens were characterized by establishing damage parameters based on changing modulus of elasticity, average strain, and strain range. Damage during the life of each specimen was defined based on modulus degradation. These modulus degradation trends were evaluated to determine damage modes such as fractured fibers and matrix cracking over the life of the specimen. The results were then compared with the physical observations of the fractured surfaces, specimen sections in the region of the fracture, and replicas of the specimen

edges. Damage progression using replica, optical, and Scanning Electron Microscope (SEM) techniques was documented in the form of fiber-matrix interface failure, matrix cracking, fiber breaking, and debonding of the fiber-matrix interface.

## II. Fatigue Testing of Metal Matrix Composites

The phenomenon called *fatigue* will cause a material to fail even at stresses below the yield strength. A fatigue failure characteristically has 3 distinct areas of failure. The first is the initiation of a crack which can be expected to occur at a location of high stress concentration such as a hole or an internal discontinuity in an otherwise homogeneous material. In the case of a fiber reinforced metal composite material, crack initiation usually occurs at the fiber-matrix interface region.

The second characteristic of fatigue failure is the crack propagation pattern. For a composite material, obstructions within the material, such as fibers, may influence the progressive development of a crack. To predict crack development, the characteristics of the fiber and matrix constituents as well as the construction of the composite needs to be understood. Metal matrix fiber reinforced composites are of a layered construction. Each layer is made up of either fibers or metal. A major advantage of this type of composite is the ability to "fabricate in" directional properties by placing the fibers within the matrix in certain directions to meet specific design requirements. Consequently, crack progression patterns will vary depending on the composite construction. The third fatigue failure characteristic is fatigue fracture which occurs without warning.

To determine the fatigue strength of a material under fatigue loads, specimens are subjected to repeated loads which vary between specified maximum and minimum levels while the number of load reversals are counted to destruction. In turn, the results of fatigue life testing can be used to design a component for a finite service life. There are limitations. Clear design criteria, similar to the ones that exist for fatigue of metals, have not yet been established for fiber reinforced composites. However, many important aspects of the fatigue of composites are understood.

Unidirectional fiber reinforced composites possess excellent fatigue resistance in the fiber direction. This is because the fibers of a unidirectional composite, which typically have high fatigue resistance, carry most of the load. Some plies, within a composite laminate, are weaker than others in a loading direction because of the differences in orientation of individual plies. Fatigue damage within a composite occurs in one or more forms such as failure of the fiber-matrix interface, matrix cracking, fibers breaking, and ply delamination. As a result of the damage occurring in individual plies, elastic property values, e.g., strain and modulus, generally decreases (6:224). The nature of the fatigue will vary not only between composites of different constituent materials but also for composites of the same constituent materials and

different construction. Hence, extensive testing is necessary to fully characterize the fatigue behavior of fiber reinforced composites.

Johnson, Lubowinski, and Highsmith (7:1-11) conducted fatigue tests of Ti-15-3 titanium matrix composite containing silicon carbide fibers. These tests were performed on 5 different lay-ups at room temperature and a cyclic frequency of 10.0 cps. The lay-ups they selected for test were  $[0]_4$ ,  $[90]_4$ ,  $[0/\pm 45]_4$ ,  $[0/90]_{2s}$ , and  $[0/45/90]_4$ . They found that the off-axis laminate plies ( $90^\circ$  and  $45^\circ$ ) suffered fiber-matrix interface failures at stress levels as low as 140 MPa which significantly effected the mechanical properties of the composite. The authors proposed that, once the stress in the  $0^\circ$  fibers (fibers in the direction of the load) is determined, a correlation could be made to determine the fatigue life of different laminates containing  $0^\circ$  plies. This model assumed that the stiffer  $0^\circ$  fibers would be the last to fail and therefore dictate fatigue life. They correlated the fatigue life data from the four different laminate types containing  $0^\circ$  fibers to the stress range in the  $0^\circ$  fibers of each specimen with good results. All points, on a plot of maximum  $0^\circ$  stress verses cycles to failure, fell within a single band of about 300 MPa stress range.

This type of model may prove to be useful to consider fatigue life of a composite at a predicted load frequency

under benign environmental conditions. However, corrosive atmospheres and extreme temperature conditions are often imposed on a specimen to simulate environmental conditions for specific design applications. Metal matrix composites are of current interest because they exhibit high strength at elevated temperatures. Consequently, fatigue testing at high temperatures is required to more fully characterize the fatigue behavior of these composites.

Gayda, Gabb, and Freed have investigated fatigue behavior of SCS6/Ti-15-3 unidirectional composite at constant temperatures of 300°C and 550°C (2:1-10). They concluded that the matrix does not, by itself, control the fatigue life of the composite. At high stress levels and at 550°C, fiber-matrix interface crack initiation followed by matrix crack propagation was thought to limit the fatigue life of the composite. They found that, for the fatigue tests conducted at 550°C, the composite showed a pronounced increase in mean strain, due to creep of the matrix, over the life of the tests. For the fatigue tests conducted at 300°C, the mean strain remained constant throughout the life of the tests. They therefore concluded that the effects of creep could be ignored at this temperature. Gayda et al. conducted the fatigue tests of the composite on a stress basis (load controlled). They also performed strain based (strain controlled) tests of the titanium matrix material. They observed that, although the fatigue life of the

composite exceeded that of the matrix alloy on a stress basis, the fatigue life of the matrix exceeded that of the composite on a strain basis.

Realistically, actual in-service use of a composite material often includes mechanically as well as thermally fatigued applications. Fatigue testing, simulating the more complex thermomechanical loading conditions, can be expected to result in a widely differing characterization of fatigue damage than that obtained by mechanical or mechanical-isothermal fatigue tests. Castelli, Ellis, and Bartolotta (3:1-10) investigated the thermomechanical (93°C to 540°C) and isothermal (427°C at 0.167 cps) fatigue behavior of the SCS6/Ti-15-3 composite. They found that the fatigue lives were significantly reduced under full thermomechanical conditions when compared to those obtained under comparable isothermal, in-phase and bi-thermal conditions. Fractographic and metallographic analysis revealed distinct differences in damage modes between the specimens subjected to isothermal, in-phase, and out-of-phase fatigue conditions. Metallographic analysis of the isothermal specimens revealed extensive matrix cracking associated with fiber damage throughout the cross-section of the specimen. On the other hand, the out-of-phase metallography revealed extensive matrix damage associated with minimal fiber cracking. They found that, for the out-of-phase specimens, damage was located exclusively at and near the surface. The

in-phase conditions produced extensive fiber cracking throughout the entire cross-section associated with minimal fiber damage. Castelli et al. also observed that cyclic mean strain significantly increased over the first several thousand cycles and continued to increase gradually throughout the life of the specimens. This suggests that creep cannot be ignored at this temperature of 427°C whereas Gayda et al. (2:10) had shown that at 300°C creep was insignificant.

Majumdar and Newaz (4:1-18) have also conducted thermomechanical (315°C to 650°C) and isothermal (650°C at 2.0 cps) fatigue tests on SCS6/Ti-15-3, [0/±45/90], quasi-isotropic metal matrix composite. They observed that, on a stress basis (load controlled), the thermomechanically fatigued specimens had a shorter life than the isothermally fatigued specimens. They also found that delamination cracking between the plies was prevalent in the thermally and thermomechanically cycled specimens. They suggested this delamination of the plies is sensitive to local fiber volume fractions since the cracks were aligned parallel to the loading direction and appeared to be concentrated between closely spaced fibers. Delamination of the plies of the isothermally tested specimens was considered negligible. Transverse matrix cracking occurred in both the thermomechanically and the isothermally fatigued specimens and originated at the fiber-matrix interfaces. Majumdar et

al. suggested that local strains in the fiber-matrix region may control fatigue life.

More recently, Pollock and Johnson (5:1-11) performed isothermal (at 650°C) fatigue tests at 10.0 cps on a strain basis (strain controlled) on 5 different lay-ups of this same composite:  $[0]_1$ ,  $[0/90]_{1,1}$ ,  $[0_{\pm 45}]_1$ , and  $[0/\pm 45/90]_{1,1}$ . They observed that initial damage occurred in either the fibers or the matrix. High strains and short lives resulted in only multiple fiber failure with no signs of matrix fatigue cracking. Low strains and long lives resulted in extensive matrix cracking with no fiber breakage away from the fracture surface. They suggested that the cyclic life of the composite was governed by the stress in the 0° fibers. For each lay-up tested, the 0° fiber stress, plotted against the cycles to failure, fell within a single band of about 700 MPa maximum stress. They also noted that the 0° fiber stress (room temperature) results from Gayda et al. (2:13) were correlated with the 0° fiber stress (650°C) results of this study and also fell within the same band.

Composites constructed with the  $[0/90]_{1,1}$  lay-up are ideal for design applications requiring biaxial loading -- especially if weight constraints are a consideration. To date, studies of the fatigue behavior of the SCS6/Ti-15-3  $[0/90]_{1,1}$  lay-up is extremely limited. Since the anticipated use of this composite material is up to temperatures of 427°C, full characterization of fatigue damage mechanisms at

this temperature is necessary. In addition, it must be determined whether fatigue damage is characteristically different at diverse frequencies. Hence, this study was conducted to systematically characterize the fatigue behavior under environmental parameters projected for the end use of this particular cross-ply lay-up.

### *III. Experimental Procedures*

The first objective of this study was to establish a sound test program to assure reliable test results. This test program is described in this section and includes a discussion on the makeup of the composite materials, how this composite was processed for the tests, and the fatigue test setup, procedure, and acquisition of test data.

#### *Materials*

A Titanium matrix fiber reinforced composite [0/90]<sub>1</sub>, crossply laminate was selected for this experiment. The complete designator for this composite is SCS-6/Ti-15V-3Cr-3Al-3Sn. The SCS-6 silicon carbide fibers have a nominal diameter of 0.142 mm and make up 38% by volume of the composite. These fibers have an inner carbon core enclosed in a cylinder of bulk SiC with alternating layers of silicon and carbon: the final layer being carbon (8).

The Ti-15-3 titanium matrix is in a stabilized beta (body centered cubic crystal structure) phase in the "as fabricated" condition at room temperature (9). However, exposure to temperatures of 427°C for long periods are likely to cause a metastable beta phase to transform to the alpha phase (hexagonal close-packed crystal structure). Such a transformation age hardens this matrix material and effectively causes an increase in the tensile strength.

### *Specimens*

The composite sheet was nondestructively tested initially for internal fiber damage, gross matrix cracking, and ply delamination using ultrasonic immersion through transmission testing. Ten specimens were then cut with a diamond saw to the nominal dimensions of 158 by 12.7 millimeters.

Final specimen preparation included polishing one edge (the 1.70 by 158 mm surface) from a 45 micron to a final 15 micron diamond slurry to obtain a surface from which replicas might be used to discern crack initiation and growth. All surfaces of each specimen were then microscopically inspected at 50X and 200X magnification. Any surface abnormality, such as fiber pull out and chipped fibers were documented.

### *Fatigue Testing Procedure*

These tests were conducted on an 808 Material Test System (MTS) with a 22 kip load cell capacity. Figure 1 is a block diagram of the test setup. The load cell was thermally isolated from the high temperatures by a cylindrical separator designed for high rate water circulation. The tests were conducted using load control with a load ratio of 0.1, frequencies of 2.0 and 0.0208 cps, with triangular ramping. The specimen orientation during testing was with the 0° fibers parallel to the direction of loading. This orientation was verified initially by insuring that the

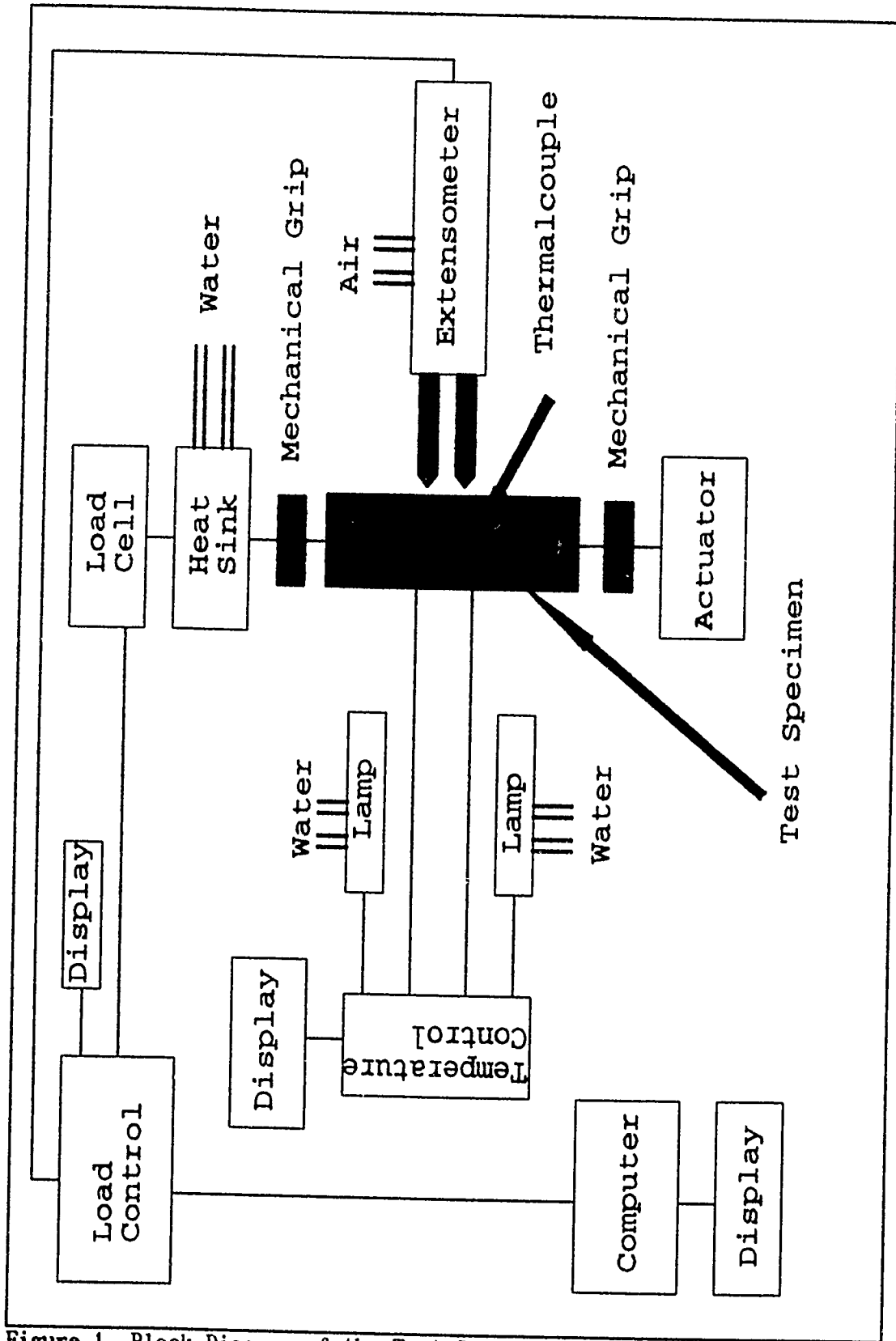


Figure 1. Block Diagram of the Test Setup

system load train was true vertical. Then, for each test setup, a level was applied to the specimen edge as the specimen was installed in the grips in a precise vertical position.

MTS Testware was the software data collection package used for this experiment. This software program was configured to collect 100 data points (load-strain equivalent points) for each cycle. The cycle data was collected for each of the first ten cycles, every 10th cycle to the 100th cycle, every 100th cycle to the 1000th cycle, etc. by a Zenith 248 computer system. Data collection also included reverse retention (data retention) of the last 10 cycles prior to specimen failure and every 10th cycle for the last 100 cycles.

The temperature was controlled by maintaining a constant temperature of 427°C over a gage length of 25.4 mm using a Micricron 823 microprocessor and 2 sets of chromel-alumel thermocouple wires welded to each side of the specimen. Radiant heat was provided by two Radiant Energy Research, Inc. parabolic strip heater lamps with 1000 watt tungsten filaments. Each heat lamp was thermally protected by constant water flow pumped from a conditioning reservoir maintained at 4.4°C. A thermocouple and heater lamp placement diagram is presented in Figure 2. The thermocouple wires were welded 12.7 mm apart to insure minimal thermal gradients within the 25.4 mm gage length

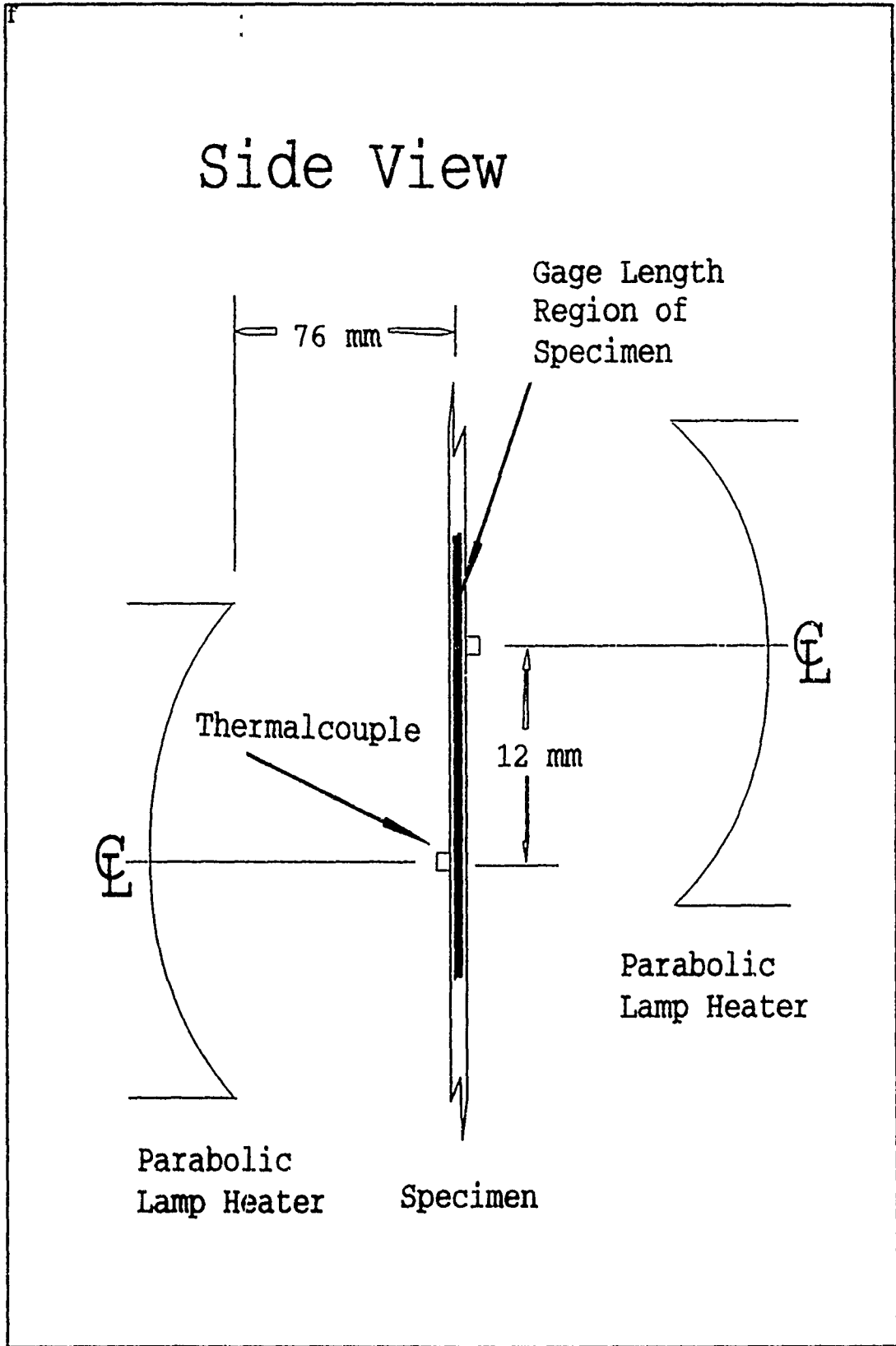


Figure 2. Thermocouple and Heater Placement Diagram

region. The lamps were mounted to the MTS frame column with a special fixture which allowed them to be positioned with 3 degrees of freedom. This lamp and lamp rod mounting arrangement is depicted in Figure 3. An MTS quartz extensometer with a 25.4 mm gage length was mounted to the load frame column. The quartz rods extended 76.2 mm beyond the extensometer radiation heat shields. The extensometer was further protected from the higher temperature with cooling air ducts for forced air convection cooling. Specimen temperature was stabilized prior to strain zero adjustment.

Beyond the initial inspection and evaluation of the specimens previously mentioned, each specimen was periodically evaluated at specified intervals during the fatigue tests. This evaluation included microscopic (50X and 200X magnification) examination of the specimen surface areas identified in Figure 4 using replica techniques.

Each specimen was cycled to failure then sectioned for metallographic examination. The nominal dimensions of the sections were 6.35 by 6.35 mm. The number of sections and locations with respect to the fracture surfaces are presented in Figure 5. Preparation of these sections entailed press mounting with Epomet molding compound and eventual polishing with a 0.05 micron diamond suspension using a Buehler Vibramet I polisher.

A total of ten tests were conducted. Eight specimens

Table I. Test Plan

Fatigue Tests at 427°C				
Frequency	Maximum Stress Levels (MPa)			
2.0 cps	375	438	500	625
0.0208 cps	375 <sup>†</sup>	438	500	542
† Specimen did not fail after 500 hours of test				
Tensile Tests	427°C Stabilized Temperature			
	Ambient Temperature			

were fatigue tested and two were tensile tested. The test plan is presented in Table I. Figure 6 illustrates the test procedures followed in performing a typical fatigue test.

# Top View

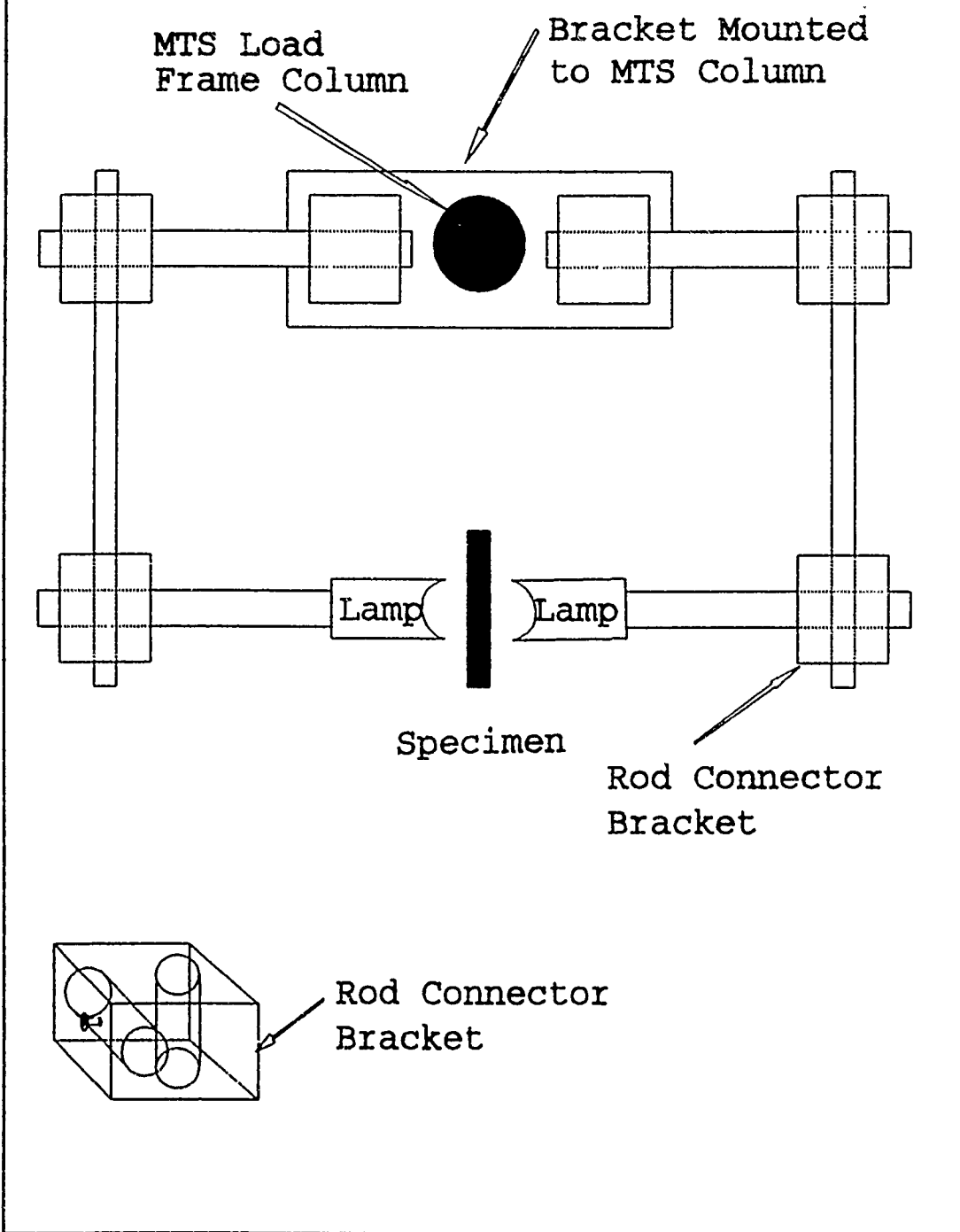


Figure 3. Lamp Heater Mounting Arrangement

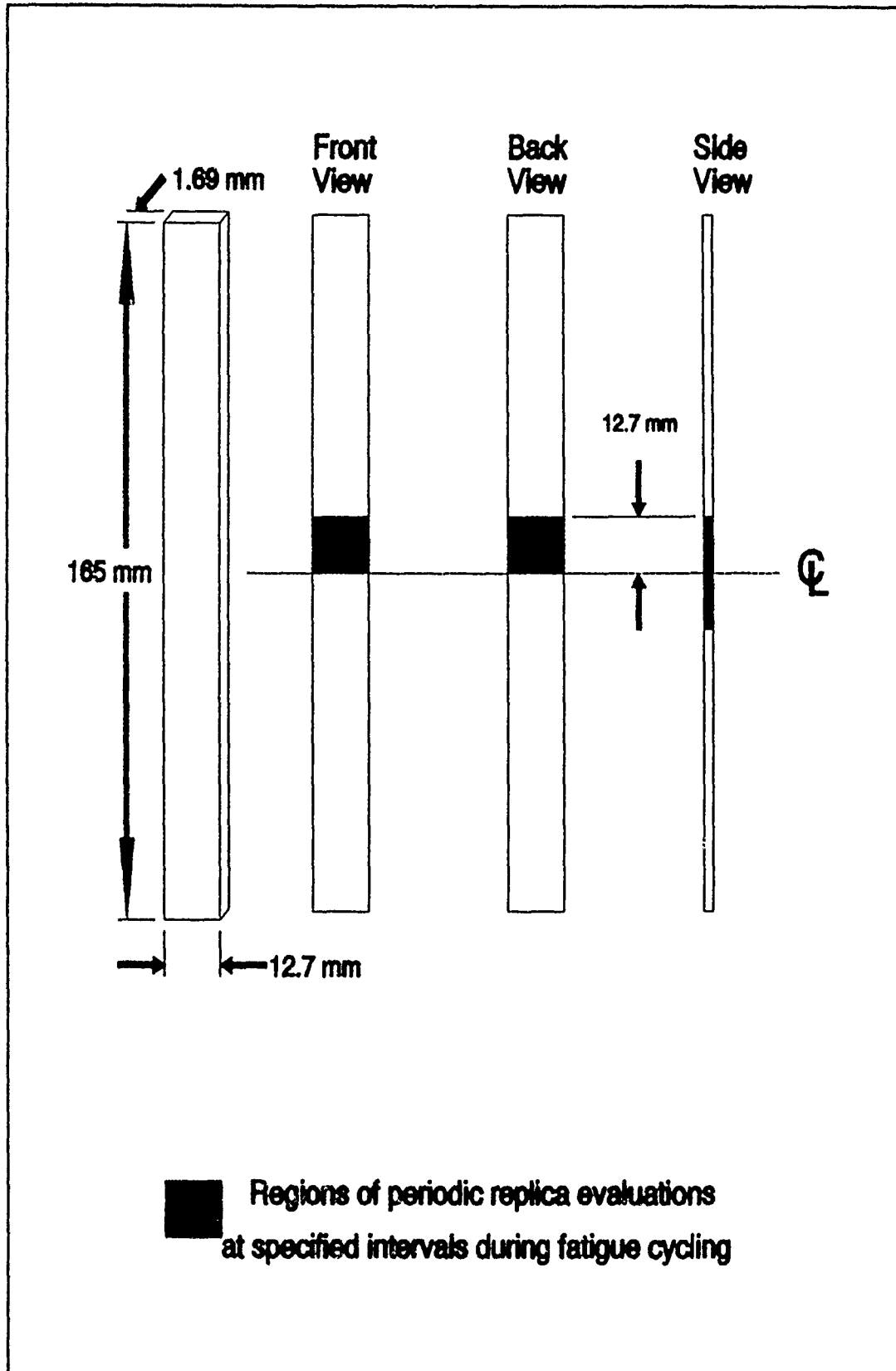


Figure 4. Specimen Dimensions & Locations of Periodic Evaluations

The arrows point to sectioned surfaces selected for microscopic and SEM analysis.

Section dimensions  
6.35 by 6.35 mm

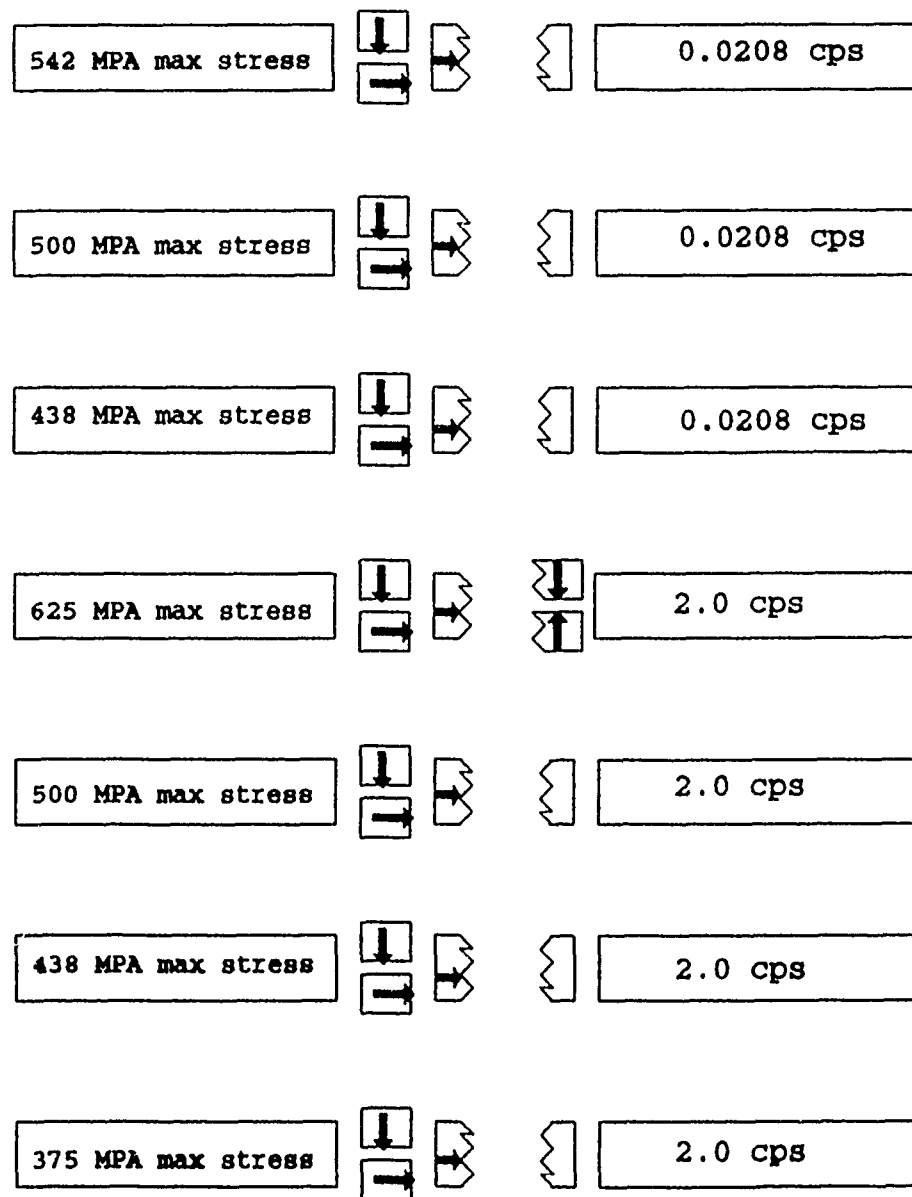


Figure 5. Specimen Sectioning for Micrographic Evaluation

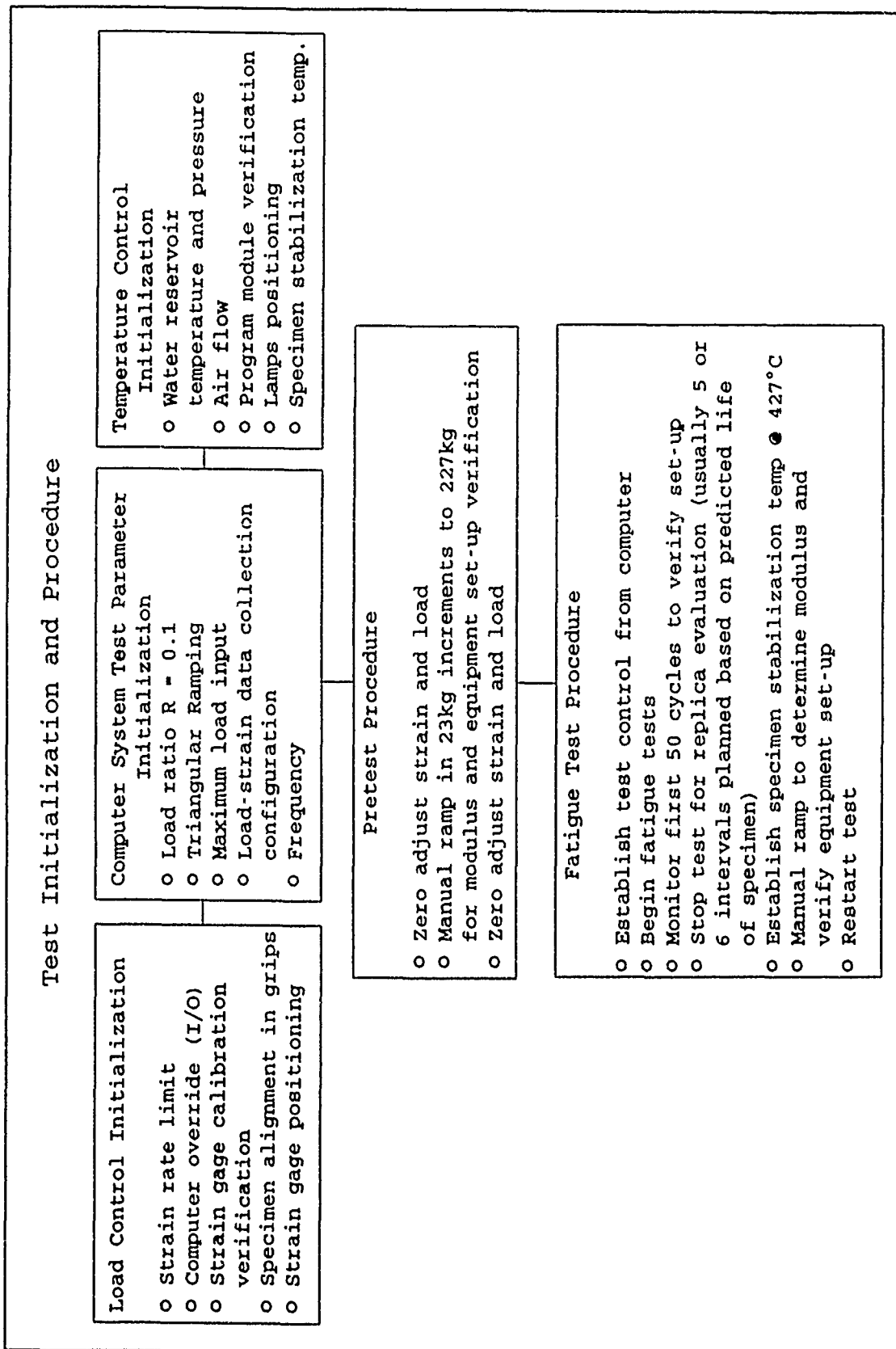


Figure 6. Fatigue Test Procedures

#### *IV. Results and Discussion*

Two methods were applied to evaluate independently the damage modes within each of the specimens during the life of the tests. First, metallographic and fractographic analysis of the sectioned surfaces and fracture surfaces along with optical evaluation of the specimen edges via replica techniques were used to determine crack initiation locations and crack progression patterns. See Figure 4 for the specimen evaluation locations. For the second method, damage was defined as a function of the modulus change (determined from stress-strain test data) during the life of the specimen. Different damage modes were then determined based on the characteristics of the damage curves for each specimen. However, before these damage modes are discussed in this chapter, the composite material properties of fatigue strength, ultimate strength, and yield strength are presented.

##### *Cycles to Failure*

Fatigue strength values of these tests are plotted in Figures 7 and 8. These S-N curves also include fatigue strength values from Johnson et al. (7) for specimens of the same material and [0/90]<sub>1</sub> lay-up cycled at 10.0 cps at ambient temperature. Comparing these figures, it is clear that cyclic frequency, mean stress, and temperature influence the life of the composite. The S-N curves behave

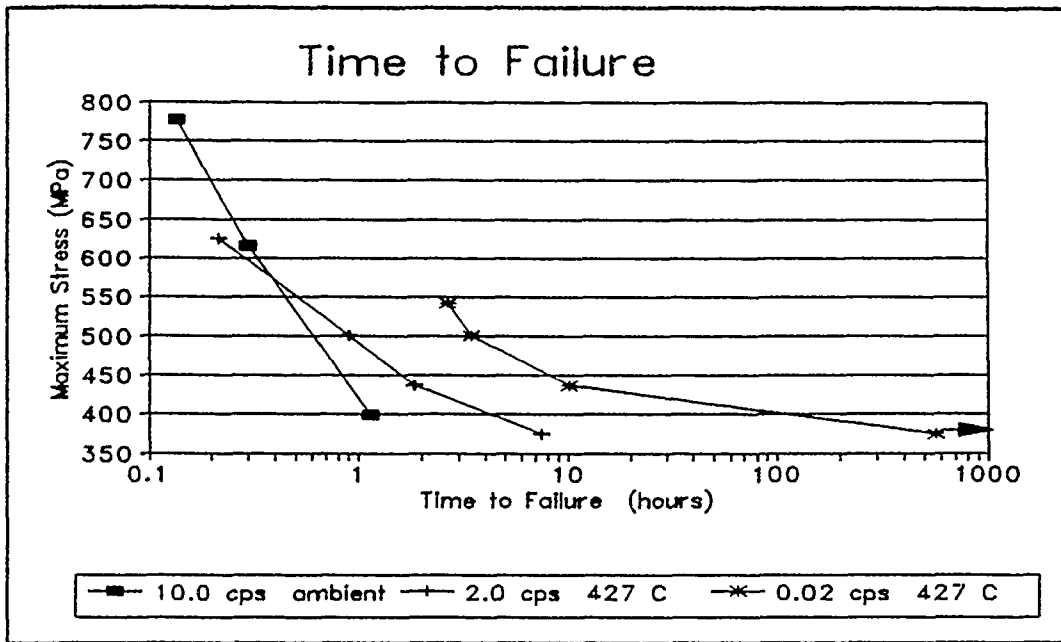


Figure 7. Time to Failure

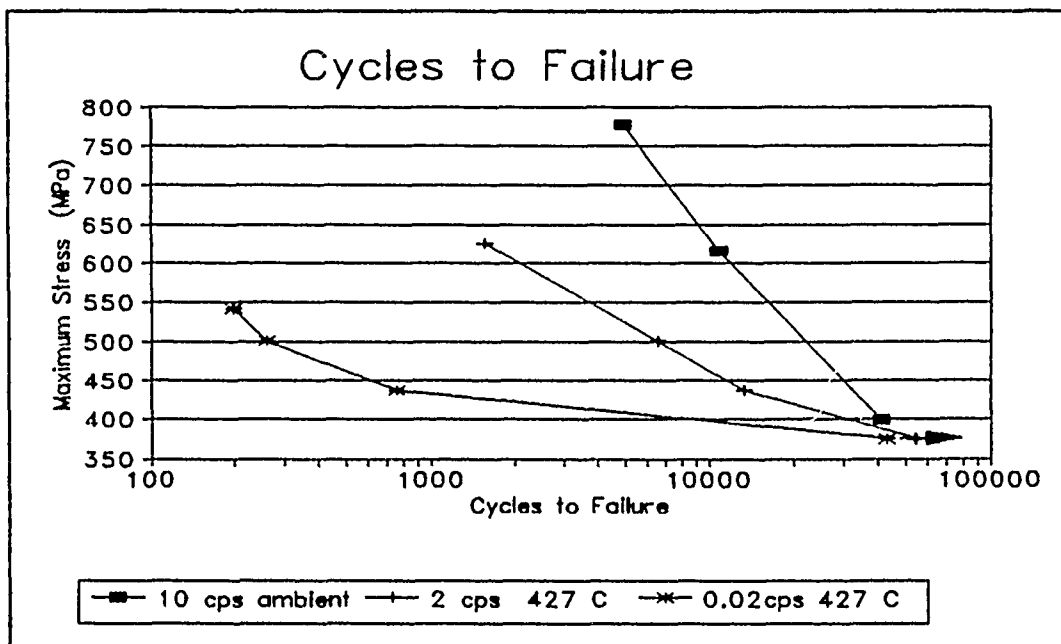


Figure 8. Cycles to Failure

differently for each test group. At a given stress level, the number of cycles to failure is greatest for the specimens tested at ambient temperature. Also, the number of cycles to failure is greater for the high frequency

specimens tested at 427°C than for the low frequency specimens. (compare the 2.0 cps and 0.0208 cps tests, Figure 8.) However, on a time exposure basis (Figure 7), the specimens cycled at lower frequencies endured longer life. The S-N curves in Figures 9 and 10 represent "best fit" curves of the values plotted on Figures 7 and 8 as well as fatigue strength values presented by Pollock et al. (5) for the same material and lay-up cycled at 10.0 cps and 650°C.

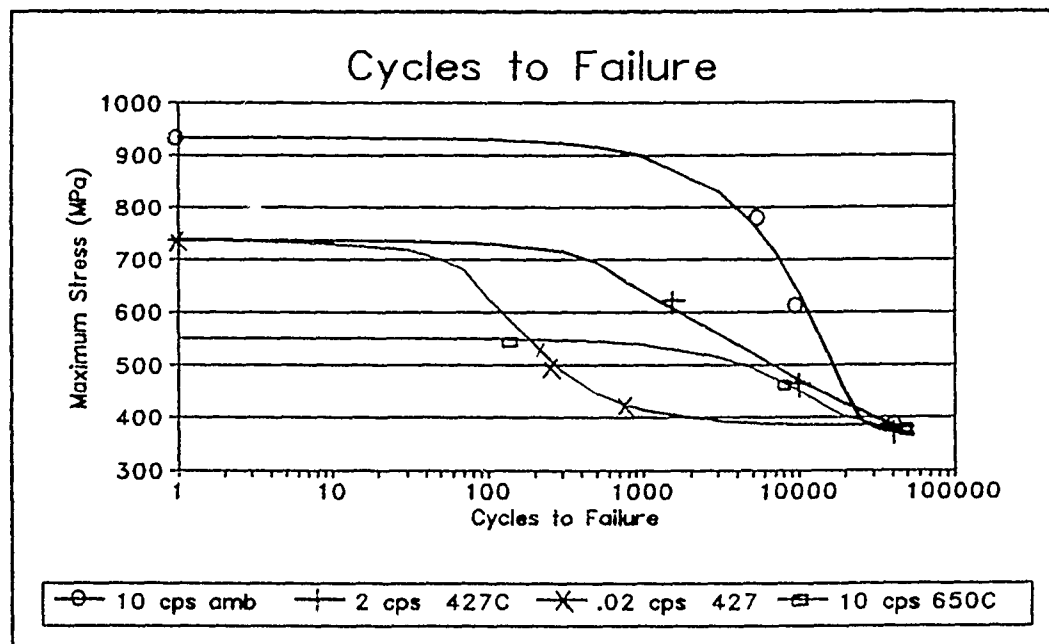


Figure 9. Cycles to Failure

Observe in Figure 10 that, below a maximum stress of about 370 MPa, temperature (ambient to 650°C) and frequency (0.0208 to 10.0 cps) no longer influence the cyclic life of this composite. In other words, for a maximum stress level below 370 MPa, this [0/90]<sub>1</sub> material can be predicted to fail well beyond 50,000 cycles providing the frequency range is between 10.0 and 0.0208 cps and the (isothermal)

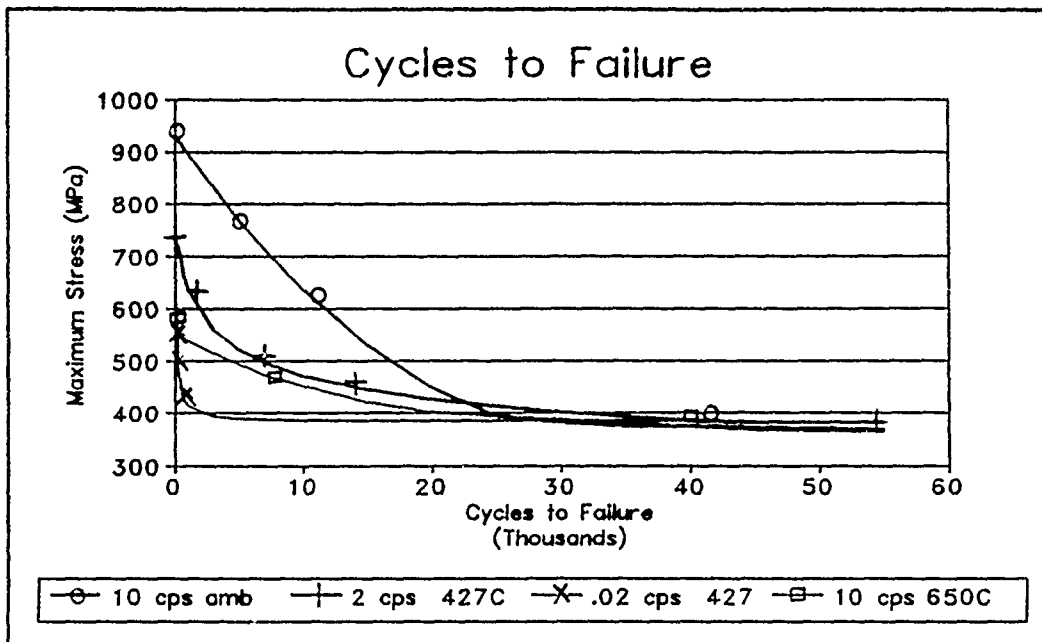


Figure 10. Cycles to Failure

temperature range is ambient to 650°C. Since all 4 curves have leveled off at 370 MPa, the endurance limit (fatigue limit) may have been reached at this stress level. Table II summarizes the fatigue test results.

#### *Tensile Tests*

Two specimens of the same nominal dimensions (Figure 4) were tensile tested. One specimen was tensile tested at ambient temperature and failed at 890 MPa. The knee of the stress-strain curve (Figure 11) occurs about 520 MPa which corresponds with the matrix yield point. The other specimen was tensile tested at a stabilized temperature of 427°C and failed at 740 MPa. The knee of this stress-strain curve (Figure 11) is about 451 MPa. This compares well with the cycle data collected from the fatigue test results. At the start of each fatigue test the maximum stress level

Table II. Fatigue Tests Failure Summary

Frequency (cps)	Maximum Stress Level (MPa)	Cycles to Failure	Time to Failure (hours)	Failure Strain (mm/mm)
2.0	375	54300	7.541	0.00568
	438	13300	1.847	0.00563
	500	6548	0.909	0.00555
	625	1561	0.217	0.00690
0.0208	375	52000+	600.0+	0.00756+
	438	760	10.15	0.00799
	500	260	3.47	0.00778
	542	199	2.65	0.00792
+ Specimen did not fail				

programmed for each test was actually higher than the maximum stress achieved over the first few cycles.

Typically, the maximum stress levels steadily increased over the first 5 to 10 cycles until the programmed value was reached. For example, the 2.0 cps 500 MPa specimen tested had a maximum stress of 280 MPa the first cycle, 320 MPa the second cycle, 360 MPa the third cycle, 403 MPa the fourth cycle, and 438 MPa the fifth cycle. The maximum stress level

# Tensile Test Ambient & Isothermal @ 427 C

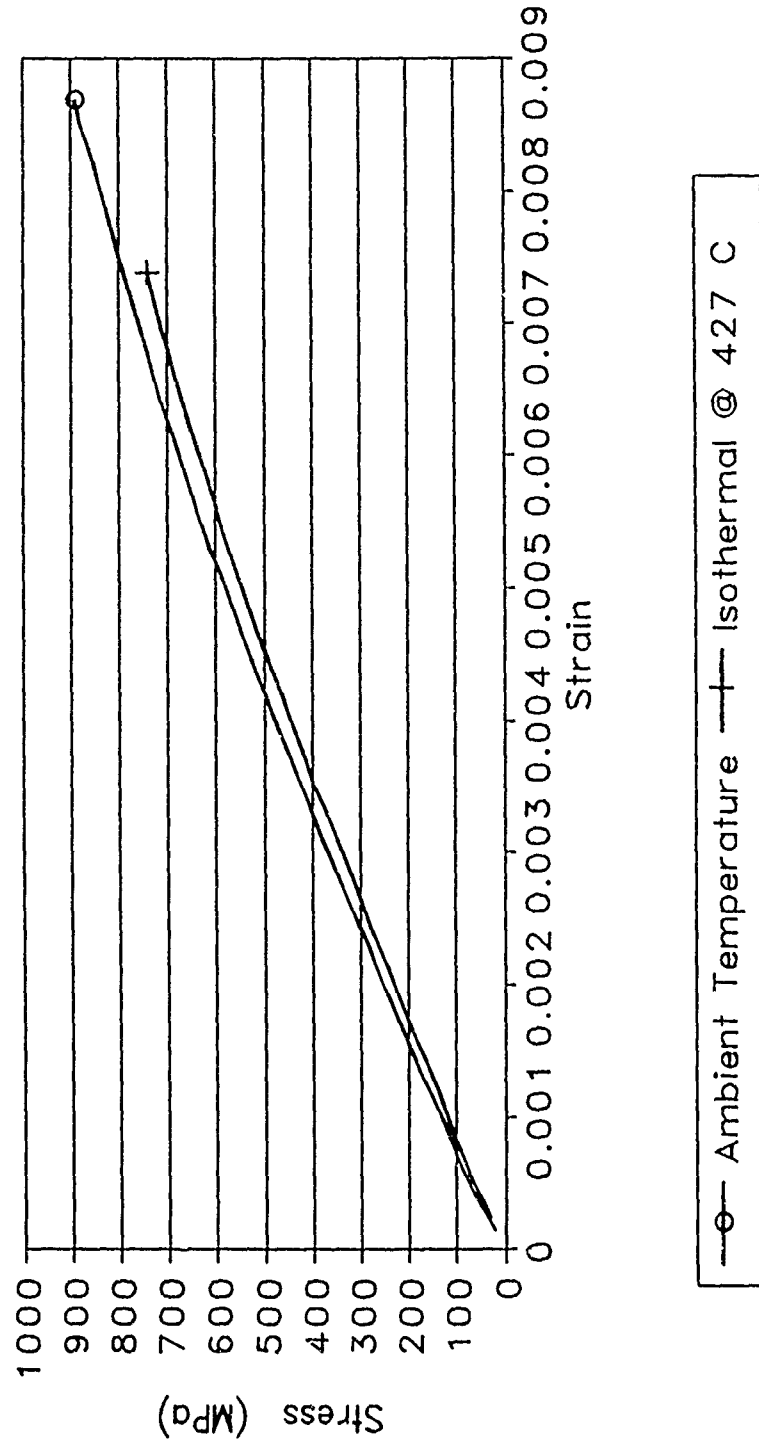


Figure 11. Tensile Tests at Ambient and 427°C

of 500 MPa was achieved at the seventh cycle. Each of the first 4 cycle hysteresis loops were closed, i.e., the strain was elastic. For the fifth cycle, however, the hysteresis loop shows nonrecoverable strain. Hence, the matrix yield point occurred at the point of nonrecoverable strain between 403 and 438 MPa. See the hysteresis loop, Figure 12.

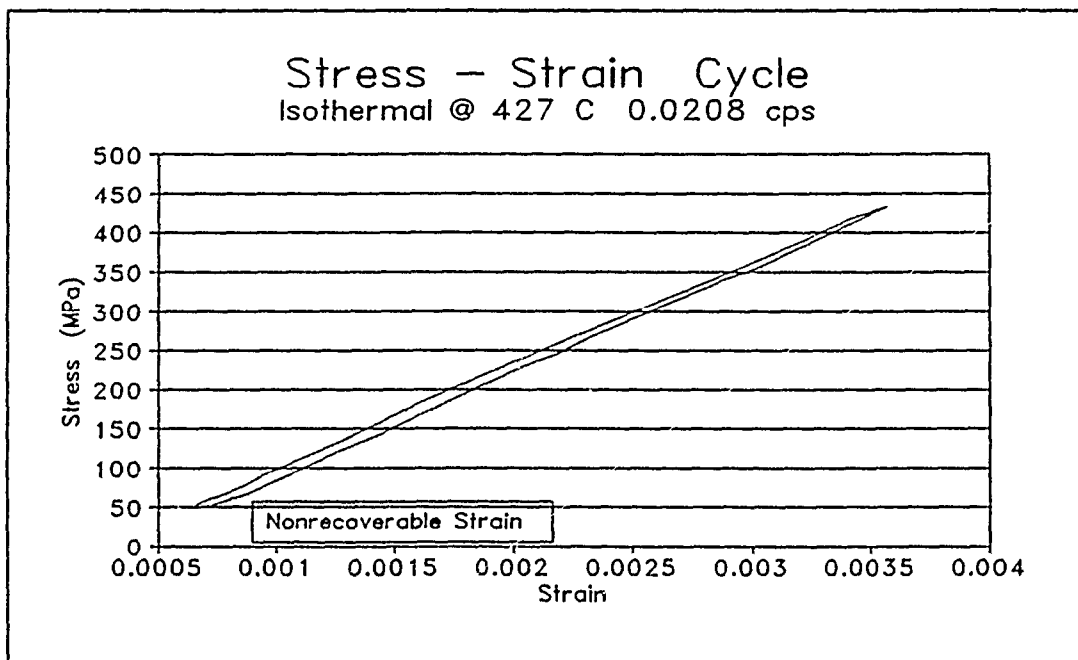


Figure 12. Yield Point at the Point of Nonrecoverable Strain.

Gayda et al. (2:11) presented matrix yield points of 695 MPa at 300°C and 450 MPa at 550°C. For comparison, linear interpolation of these values gives a yield point of 555 MPa at 427°C which is somewhat higher than obtained in the present study.

The Young's modulus for each of the curves in Figure 11 was determined from the initial slope to be 132 GPa and 122 GPa for the specimens tensile tested at ambient and 427°C respectively. Since a much larger sample is necessary to

determine the average Young's modulus of this material at specified temperatures, these values are not considered truly representative of the material. On the other hand, the initial modulus of the fatigue tested specimens stabilized at 427°C averaged about 135 GPa.

### *Evaluation Results*

In this section, the results of the microscopic replica examinations, metallographic evaluation of the sectioned surfaces, and fractographic analysis of the fracture surfaces are discussed. Figures 4 and 5 show the specimen locations selected for evaluation. Of course, the intent of these evaluations is to determine the locations of the crack initiation points and also to ascertain the nature of the crack propagation patterns under three different test conditions: stress levels, load frequency, and temperature exposure time. Here, crack initiation and growth comparisons are made between specimens tested at high stress levels with those under low stress. Failure modes of the high stress specimens are compared with the failure modes of the tensile tested specimens. Crack initiation and growth comparisons are also made between the specimens cycled at high frequency and low frequency. The third test condition, temperature exposure time, is an important parameter which changes a number of material characteristics and its effects are discussed throughout this report. However, in this section, discussion on the effects of temperature exposure time is

limited to the comparison of change in reaction zone (fiber-matrix interface region) characteristics with exposure time.

Crack initiation points of the fatigue tested specimens have been determined to occur in 5 separate locations: crack initiation at the fiber interface of the 90° fibers progressing transversely into the titanium matrix, crack initiation off the 0° fiber-matrix interface progressing into the matrix, transversely fractured 0° and 90° fibers, and crack initiation at the 0° and 90° fiber carbon core-SiC interface progressing both along the longitudinal axes of the fibers and across the bulk SiC to the fiber-matrix interface. Each of these types of crack initiation points are graphically illustrated in Figure 13.

As a result of replica examination, and metallographic and fractographic analysis, the nature of crack initiation and early propagation was found to depend on the test conditions of cyclic frequency and maximum load. Each type of crack initiation point has been categorized as having a low, moderate, or high rate of occurrence. A summary of this analysis is tabulated (Table III) for each specimen. This table will be a useful reference as the various test conditions are discussed.

Metallographic examination of the sectioned surfaces and evaluations of the specimen edges using replica techniques revealed that crack initiation and growth was profoundly different when comparing those specimens under high stress

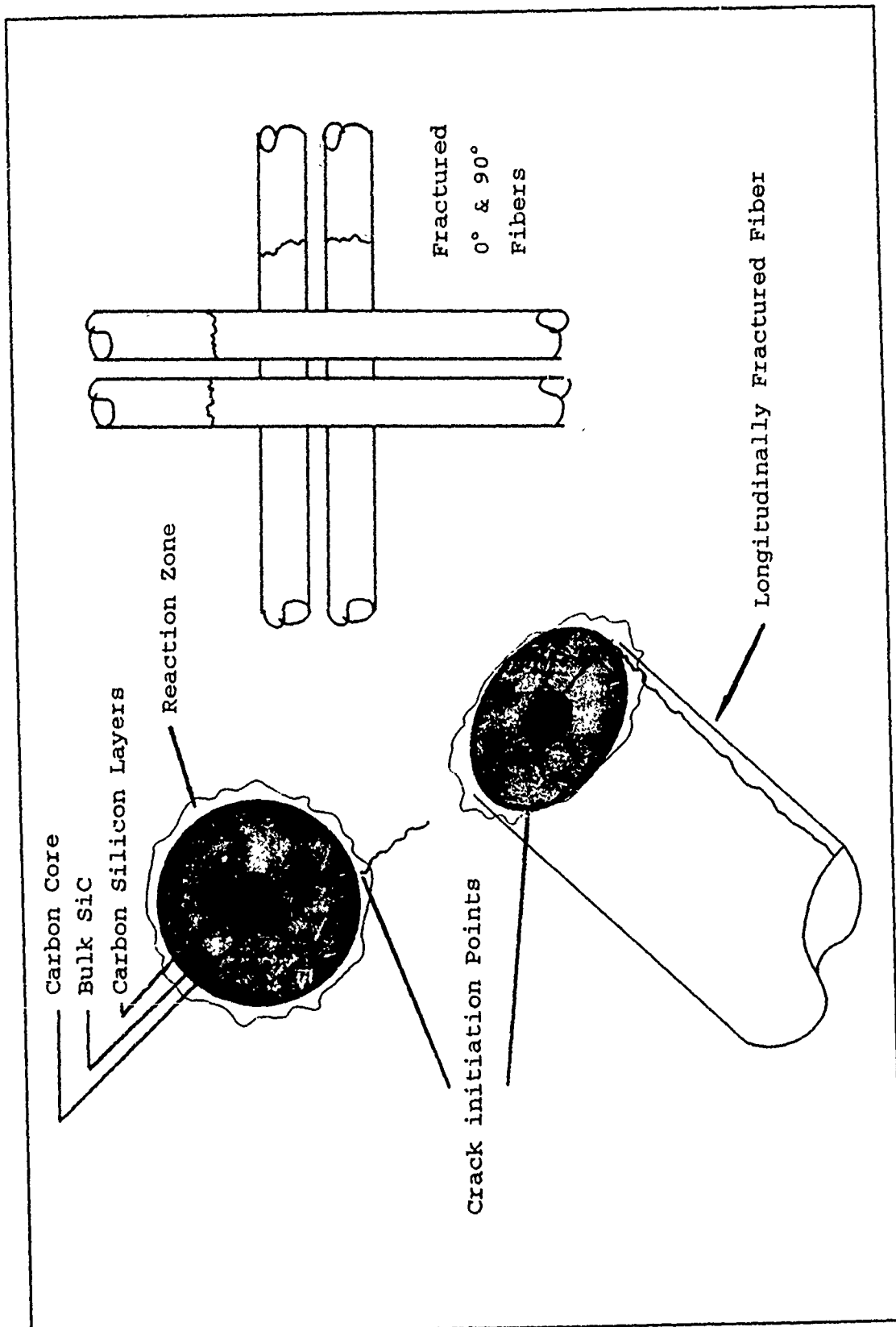


Figure 13. Locations of Crack Initiation Points

Table III. Incidence of Crack Initiation Points and Fiber Damage Locations

Crack Initiation/ Fiber Damage Locations	Low Frequency				High Frequency			
	Specimens				Specimens			
	*	438	500	542	375	438	500	625
Matrix Crack Initiation at Fiber-matrix Interface	H	M	M	M	H	H	M-H	M-H
Matrix Crack Initiation at 0° Fractured Fibers	L	L-M	L-M	H	L	L	L-M	M
Fractured 0° Fibers	L	M-H	H	H	L	L	L-M	M
Fractured 90° Fibers	L	L	L	L	L	L	L	L
Longitudinally Fractured Fibers	L	L	L-M	M	L	L	M	M

\* Specimen did not fail after 500 hours of test.

(500 to 625 MPa) with the crack progression of the specimens under low stress (54 to 438 MPa). Figures A-1 through A-7 in Appendix A are carefully drawn representations of crack sizes and orientations found through microscopic examination

of approximately 6.35 mm length of the specimen cross-sections.

Common to the low stressed specimens (at 375 MPa) of both frequencies were cracks initiating in the reaction zones of the 90° fibers then propagating transversely to the 0° fibers and, for the most part, stopping abruptly. Figure A-1 in Appendix A represents a cross-section of the 375 MPa 2.0 cps specimen depicting matrix crack termination at the 0° fibers. As the fatigue cycling progressed, more cracks initiated off the fiber reaction zones into the matrix until most reaction zones witnessed some cracking in the transverse direction. Many fiber-matrix interface cracks which initiated at the inner two 90° plies eventually coalesced by debonding within the reaction zones of these fibers. Figures 14 and 15 are photographs of the 375 MPa 0.0208 cps specimen edge at 42,000 cycles into the test. These pictures were obtained using replica techniques and clearly show this type of debonding of the 90° fiber-matrix interface region. The transverse matrix crack patterns seen in Figure 14 is representative of this specimen edge as a whole. Also, microscopic examination of the fracture surface shows cracks propagating to the surface by first debonding with the 90° fibers then coalescing at the surface (Figures 16 and 17). Figure 17 (magnification of Figure 16, top, right) shows crack initiation at the 90° fiber, propagating between the two 0° fibers, then to the specimen surface. The



Figure 14. Fiber-Matrix Initiated Cracks Coalescing about a Fiber (375 MPa 0.0208 CPS @ 42,000 cycles)

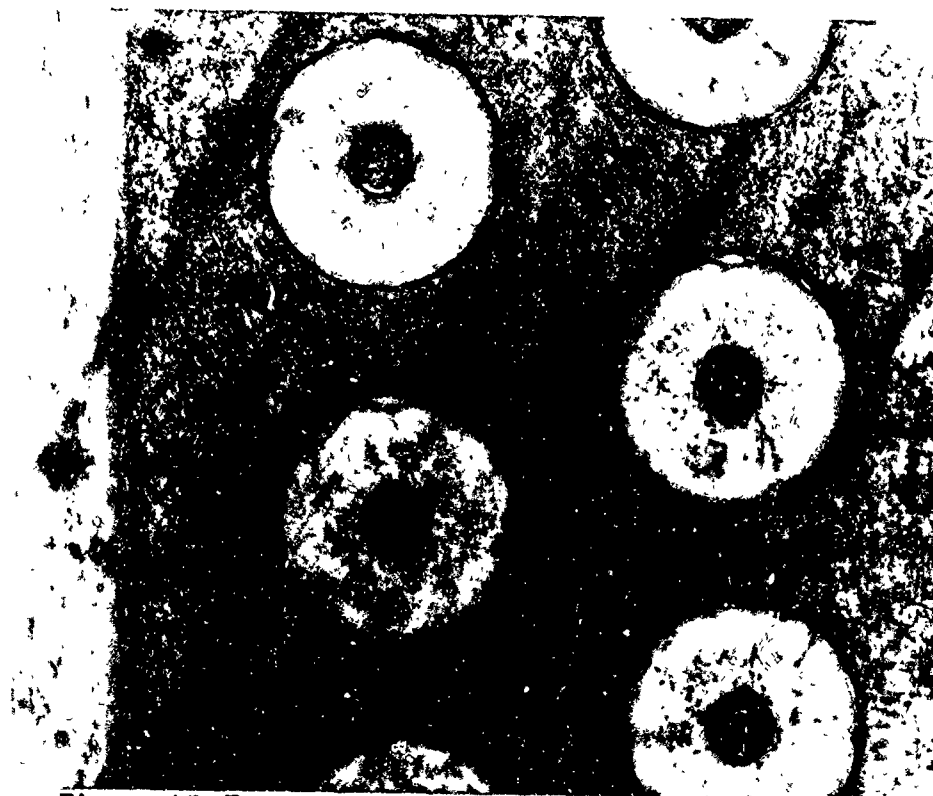


Figure 15. Transverse Cracking Between 90° Fibers and to 0° fibers. (375 MPa 0.0208 CPS, 42000 cycles )



Figure 16. Fracture Surface of the 2.0 cps, 375 MPa Specimen



Figure 17. Matrix Crack Initiating at the 90° Fiber-Matrix Interface Then Propagating to the Surface. (Magnification of Figure 16, Center)

increase in the number of cleavage lines in the vicinity of the surface indicates the rate of propagation increases toward the surface. In the outer plies, the cracks began "jumping" by passing around the 0° fibers without cracking the stiffer fibers and then propagating to the surface. The final crack pattern is clearly characterized in Figure A-1.

At the higher stress levels, 438 to 625 MPa, crack initiation commonly occurred at 2 locations depending upon the frequency of the test. The reaction zones were one of the locations of crack initiation. However, higher stresses increased the amount of fiber damage within the specimen. At the higher stresses, extreme stress concentration may exist between transverse matrix cracks and fractured fibers causing longitudinal cracking along the 0° fiber-matrix interface. In addition, higher stresses and longer exposure times to temperature are expected to cause degradation of the fiber-matrix interface region setting a path of least resistance between fractured fibers and transverse matrix cracks. This type of crack progression pattern can be seen at 2 locations along the 0° fiber on the left side of Figure 18. (Figure 18 also shows a number of 90° transverse matrix cracks coalescing.) Figure 19 is a photograph of a cross-section of the 0.0208 cps, 438 MPa specimen depicting transverse cracking initiated at the 90° fiber (bottom left), propagating to the 0° fiber, then propagating longitudinally along the 0° fiber to coalesce



Figure 18. Coalescing of 0° and 90° Fiber Interface Initiated Cracks. (500 MPa 0.0208 CPS)



Figure 19. Transverse and Longitudinal Cracking Between 0° and 90° Fibers. (438 MPa 0.0208 CPS)

with the damaged 0° fiber. This type of crack propagation can also be seen in Figure 20. While the cracks are propagating outward from the 2 inner 90° fibers there are also cracks progressing between these plies and eventually coalescing. The SEM micrographs in Figures 21 and 22 show inner ply cracks coalescing combined with debonding between the fiber-matrix interface.

As the maximum stress was increased to, say 500 to 542 MPa, crack progression from the 0° fractured fibers became more frequent. Figure 23 is a photograph of a cross-section of the 0.0208 cps, 542 MPa specimen showing transverse matrix cracking initiated at the fractured 0° fiber in a region where extensive fiber damage has occurred. This type of crack initiation was uncommon at the lower stresses.

The discussion of crack progression patterns at different stress levels was, for the most part, pictorially represented by the low frequency specimens. However, the high frequency specimens generally witnessed the same type of crack progression patterns but with significantly fewer 0° fractured fibers at all stress levels. Though these crack progression patterns were similar between the high and low frequency tests, a distinction was made (Figure 24) between the number of occurrences of crack initiation types at specified stress levels. Note that for moderate to high stress levels, the high frequency specimens had a large number of matrix cracks initiating off the 90° fibers but

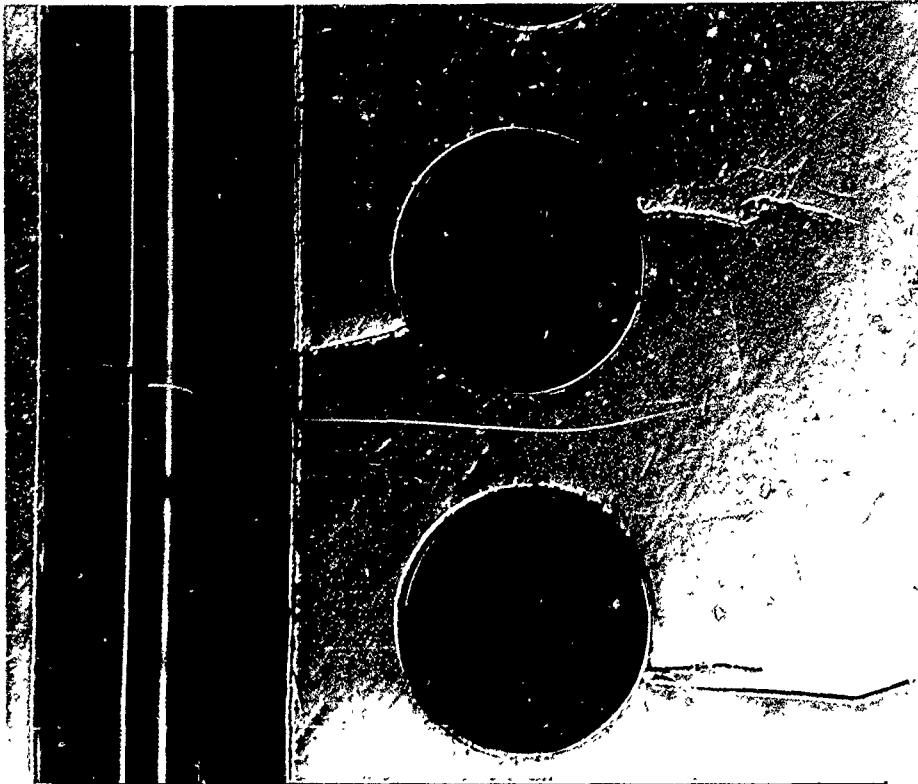


Figure 20. Coalescing of 0° and 90° Fiber Initiated Cracks. (542 MPa 0.0208 CPS)

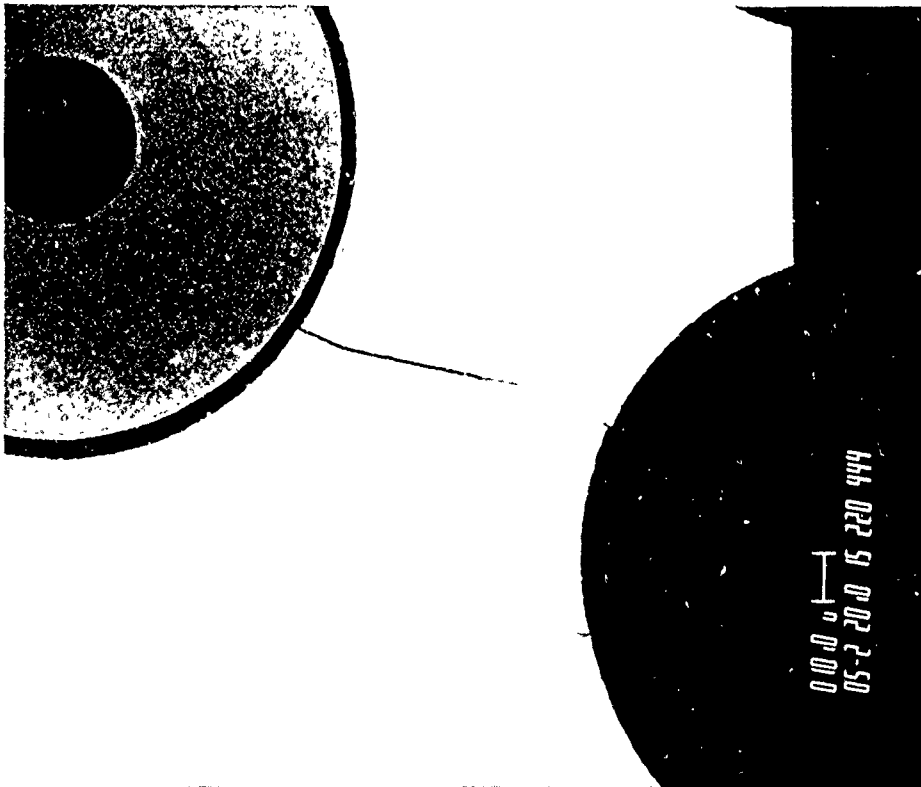


Figure 21. Inner Ply Cracks Coalescing and Debonding of 90° Fiber-matrix Interface. (438 MPa 0.0208 CPS)



Figure 22. 90° Fiber-matrix Interface Separation.  
(438 MPa 0.0208 CPS)



Figure 23. Transverse Matrix Cracks Initiated off the  
0° Reaction Zone. (542 MPa 0.0208 CPS)

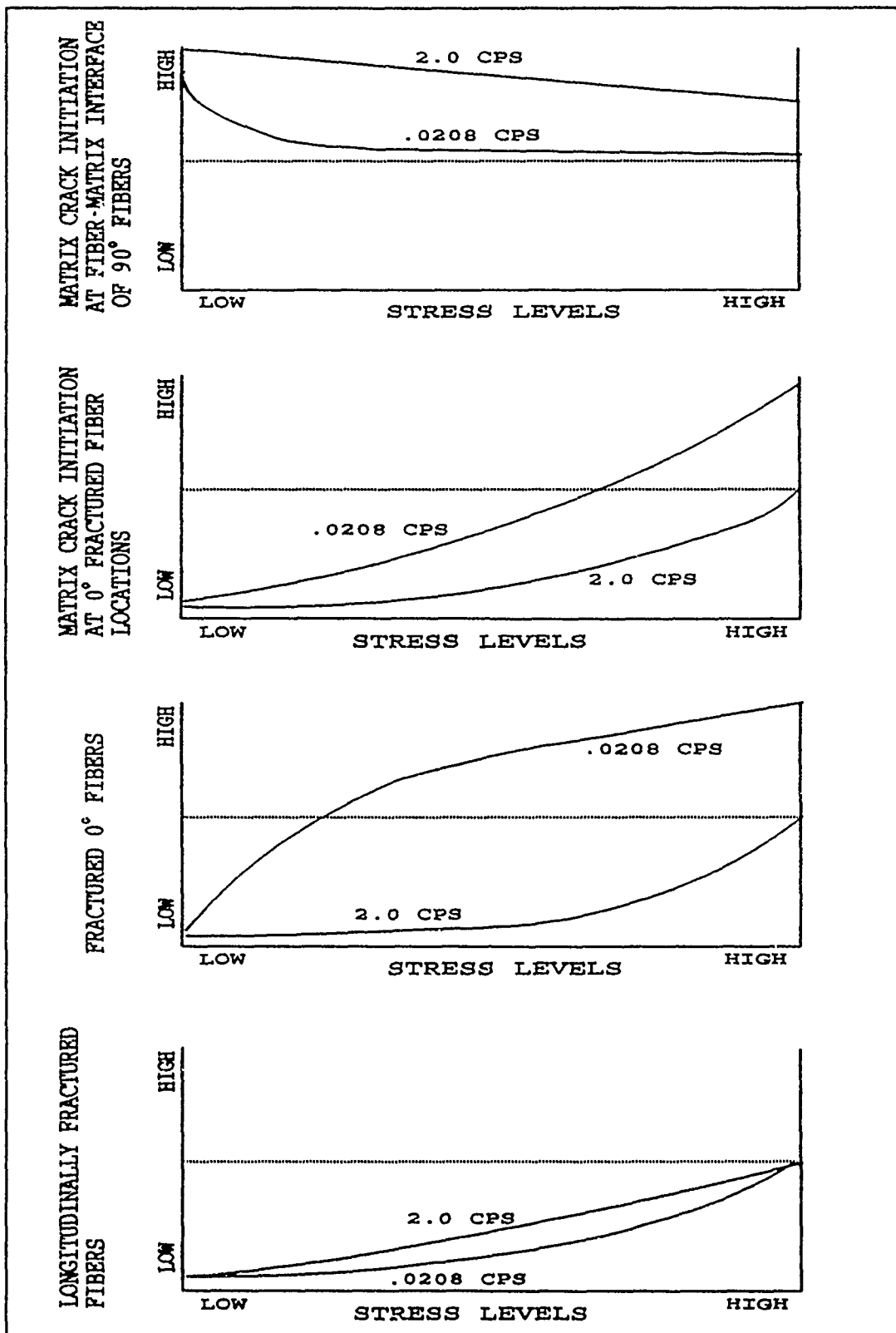


Figure 24. Frequency of Crack Initiation and Fiber Damage.

had relatively fewer fractured fibers when compared with the low frequency tests. In contrast, at moderate to high stress levels, the low frequency specimens endured a much greater number of 0° fractured fibers with a relatively lower quantity of fiber-matrix crack initiation at the 90° fibers. Obviously, since the low frequency specimens had a greater number of fractured fibers, the number of cracks initiating out of the fractured fiber region is larger than what was observed on the 2.0 cps specimens. However, metallographic analysis revealed that these particular cracks generally progressed over a much shorter distance causing less damage to the matrix than the cracks propagating off the 90° fibers.

Another type of crack initiation and growth mentioned previously was crack initiation off the inner carbon core of the fibers then propagation through the bulk SiC and along the longitudinal axis of the fiber. In Appendix A, Figures A-3, A-4, and A-7 show a number of longitudinally fractured 0° and 90° fibers for the high frequency 500 and 625 MPa specimens and the low frequency 542 MPa specimen.

These types of fractures were revealed during microscopic examination of the sections. Eventually, these longitudinally fractured fibers initiate some matrix cracking. Figure 25 shows such a crack propagating through about 80% of the bulk SiC. Figures 26 and 27 also show crack propagation from the carbon core through the fiber-matrix

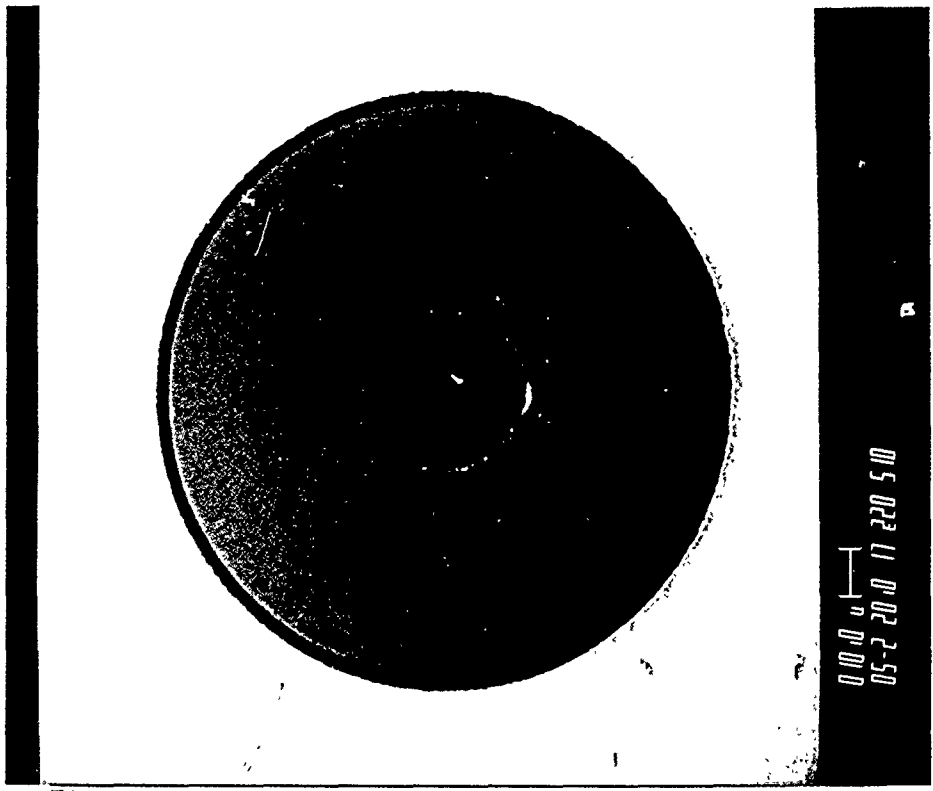


Figure 25. Crack Propagating From Inner Carbon Core of 0° Fiber. (500 MPa 2.0 CPS)



Figure 26. Crack Propagating From Inner Carbon Core of 90° Fiber to Titanium Matrix. (500 MPa 2.0 CPS)

interface. Figure 27 is a SEM micrograph of higher magnification of the right portion of the fiber in Figure 26. Analysis of the fracture surfaces also revealed that 90° fiber fractures along the longitudinal axis occurred more often with the higher stressed specimens and possibly was a mechanism to induce failure.

One of the most clear distinctions that could be made of crack initiation to failure mechanisms was in a comparison of the fracture surfaces of the specimens cycled at high frequency with those cycled at low frequency.

For the high frequency group of tests, crack initiation points were primarily at the 90° fiber-matrix interface. Fractured fibers occurred infrequently up to the point of specimen failure -- even at the higher maximum stress levels. Figures 28 and 29 are SEM micrographs of the fracture surface of a 2.0 cps specimen. This fracture surface indicates cleavage fracture of a matrix in the brittle mode. The high frequency fatigue cycling possibly work hardened the titanium matrix and caused it to become more brittle. Unlike the low frequency specimens, these specimens were not exposed to high temperatures long enough to initiate much crystalline restructuring from beta to alpha by way of age hardening. However, the strain hardening along with exposures to high temperatures possibly induced some alpha precipitates to occur. At the molecular level, This crystalline restructuring to a more compact hexagonal

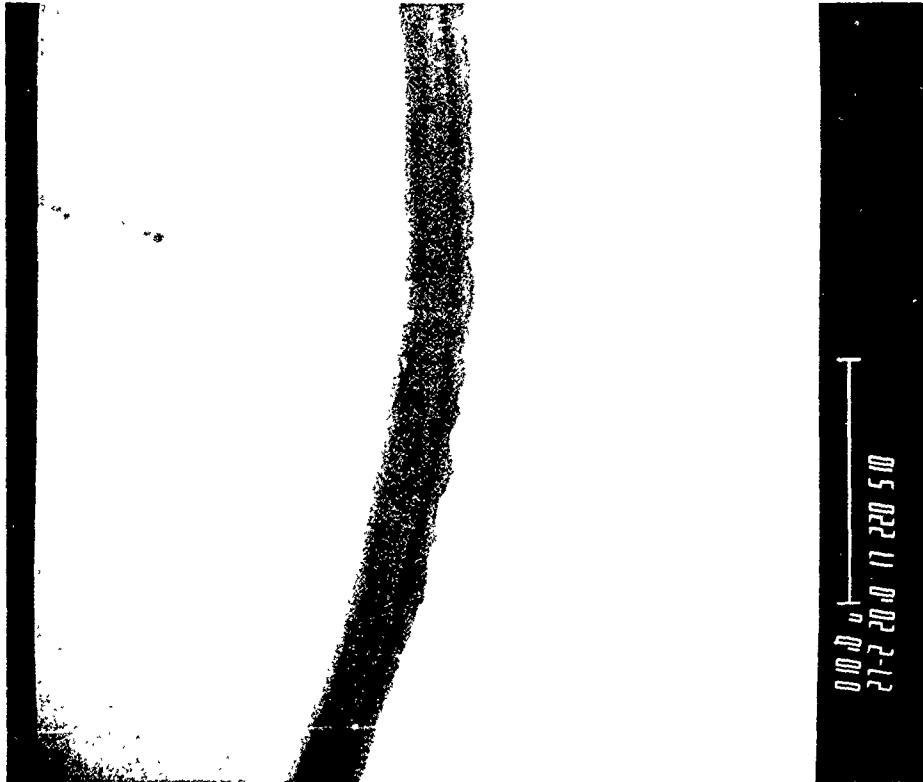


Figure 27. Magnification of Figure 26 (Right).  
(500 MPa 2.0 CPS)

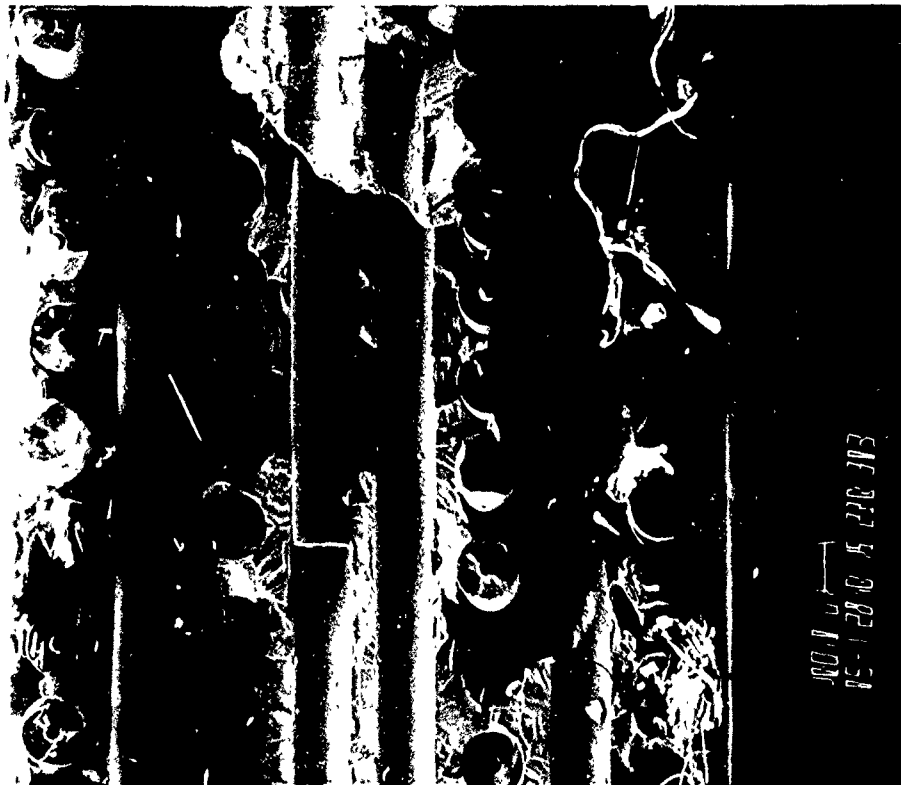


Figure 28. Cleavage Fracture of Matrix in the Brittle  
Mode. (375 MPa 2.0 CPS)

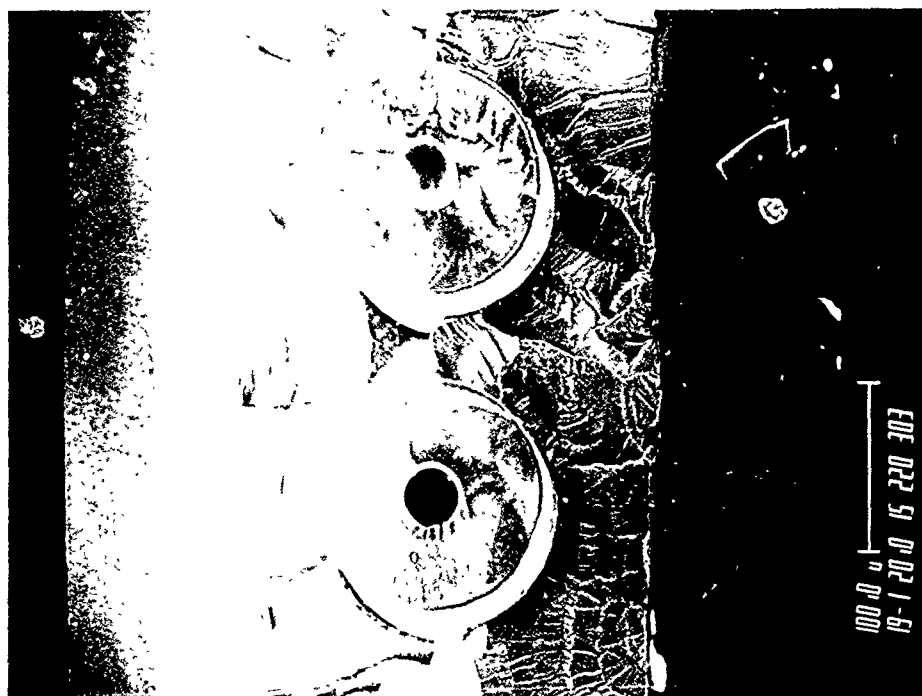


Figure 29. Magnification of Figure 28 (Center).  
(375 MPa 2.0 CPS)

closed-packed structure over a lattice network is expected to cause slip planes. The high frequency fatigue process induces more favorably oriented planes for slip to occur and eventually, dislocation tangles form. These tangles make it more difficult for slip to take place as the dislocation sites are used up. Consequently, this process causes the titanium matrix to become much more brittle. In Figure 29, the actual fracture follows cleavage planes with some plastic deformation distinguishable by step formations. These step formations are a measure of the limited amount of plastic deformation taking place during crack propagation.

This strain hardening phenomenon of the matrix limited the amount of strain imposed on the  $0^\circ$  fibers until the

matrix essentially failed. At this point, the fibers began to fracture. Castelli et al. (3:13) suggested the possible occurrence of matrix strain hardening during out-of-phase thermomechanical fatigue testing of uniaxial SCS6/Ti-15-3 at 427°C and 0.167 cps.) Hence, the matrix failure preceded the 0° fiber failure. Periodic replica evaluations of the high frequency specimen edges also revealed very little fiber damage during the duration of the tests. The highest stressed (625 MPa) specimen was the exception. Initial matrix failure for these high frequency specimens was also determined when analyzing the test strain data. See the section titled *Strain to Failure*.

On the other hand, the low frequency group of fatigue test specimens witnessed a considerable number of fractured 0° fibers along with fiber-matrix interface initiated matrix cracks. For this group of tests, primary failure was due to ductile void coalescence preceded by fractured fibers. Figure 30 depicts the type of matrix deformation (necking) due to fractured fibers common with this group of specimens. Figure 31 is a SEM micrograph of a fractured surface showing this type of ductile void failure. This figure also indicates that substantial plastic straining has occurred over a "large" volume of material (the matrix surrounding the fiber). This ductile fracture region is characterized by dimples. Since plastic straining predominated, as opposed to the brittle cleavage type fracture that occurred with the

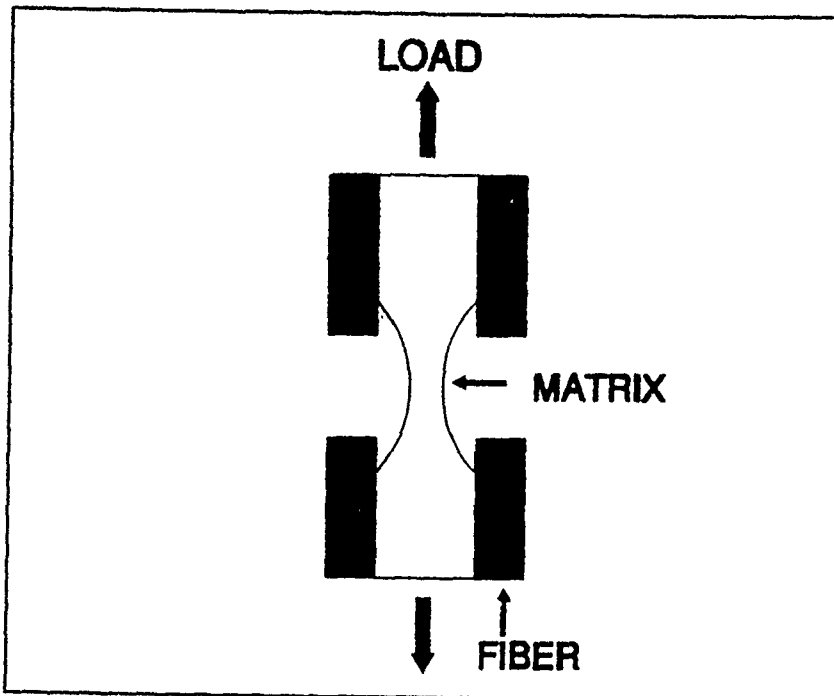


Figure 30. Matrix Necking (Plastic Deformation) Due to Fractured Fibers

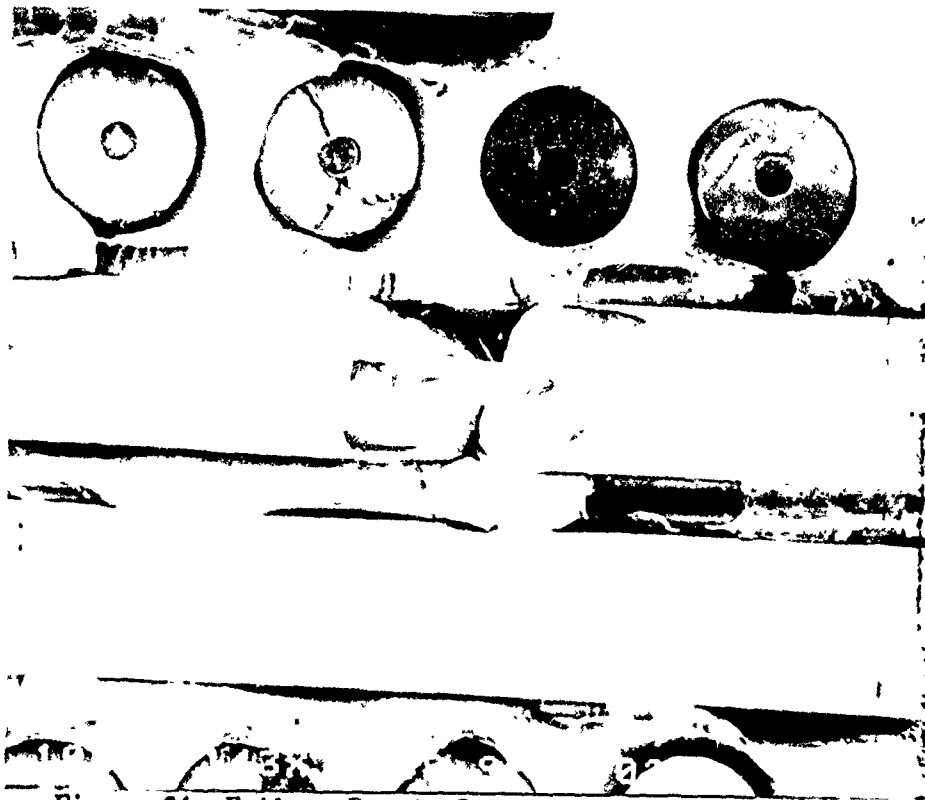


Figure 31. Failure Due to Ductile Void Coalescence.  
(500 MPa 0.0208 CPS)

high frequency specimens, final failure can be presumed to be caused by ductile void coalescence failure. In addition, sectioned surface evaluations revealed extensive fiber fracture with much less matrix damage than occurred with the high frequency specimens. The exceptions are the 375 MPa specimens as discussed previously. Compare the matrix crack sizes and incidence rate of fiber damage of both 438 MPa specimens (Appendix A, Figures A-2 and A-5) and both 500 MPa specimens (Appendix A, Figures A-3 and A-6).

Similarly, the 427°C tensile tested specimen failed in this manner. A section of the fracture surface for this specimen is presented in Figures 32 and 33. Pollock and Johnson (5:9-11) have also observed this type of ductile void failure of tensile tested (at 650°C)  $[0/90]_2$  lay-up of SCS6/Ti-15-3 composite. For load controlled fatigue tests at 10.0 cps of  $[0]_1$  unidirectional composites, they made a distinction between matrix fatigue cracking inducing failure and ductile matrix failure. They determined that the likelihood of ductile void failure increased with increasing stress levels, i.e., reducing the number of fatigue cycles increased the amount of ductile failure.

As previously mentioned, the primary mode of matrix failure of the high frequency specimens was cleavage fracture in the brittle mode. the exception was the specimen tested at 625 MPa. The fracture surface of this specimen exhibited a combination of ductile matrix failure and

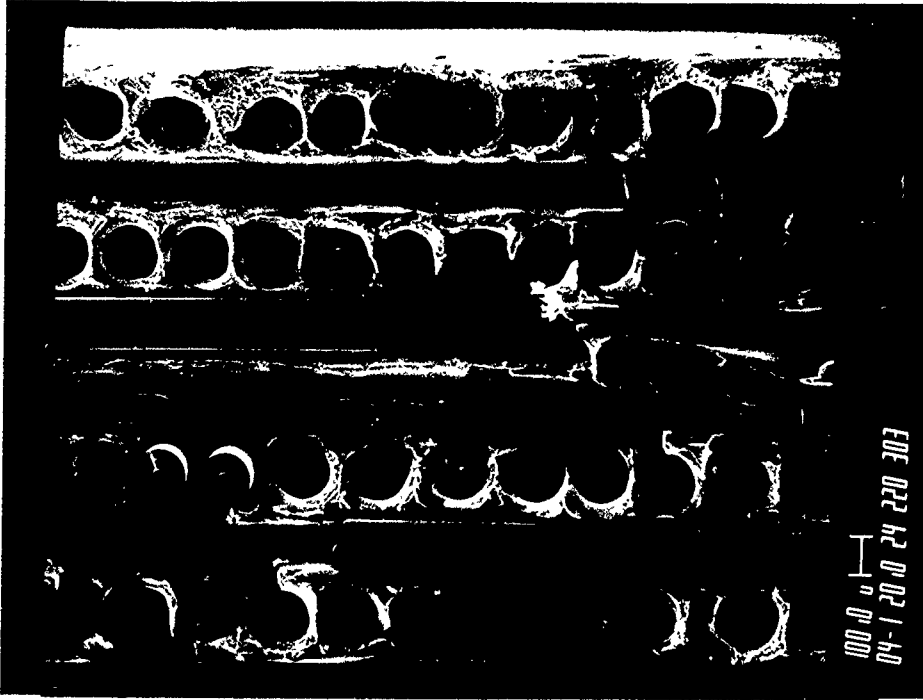


Figure 32. Fracture Surface of 427°C Tensile Tested Specimen

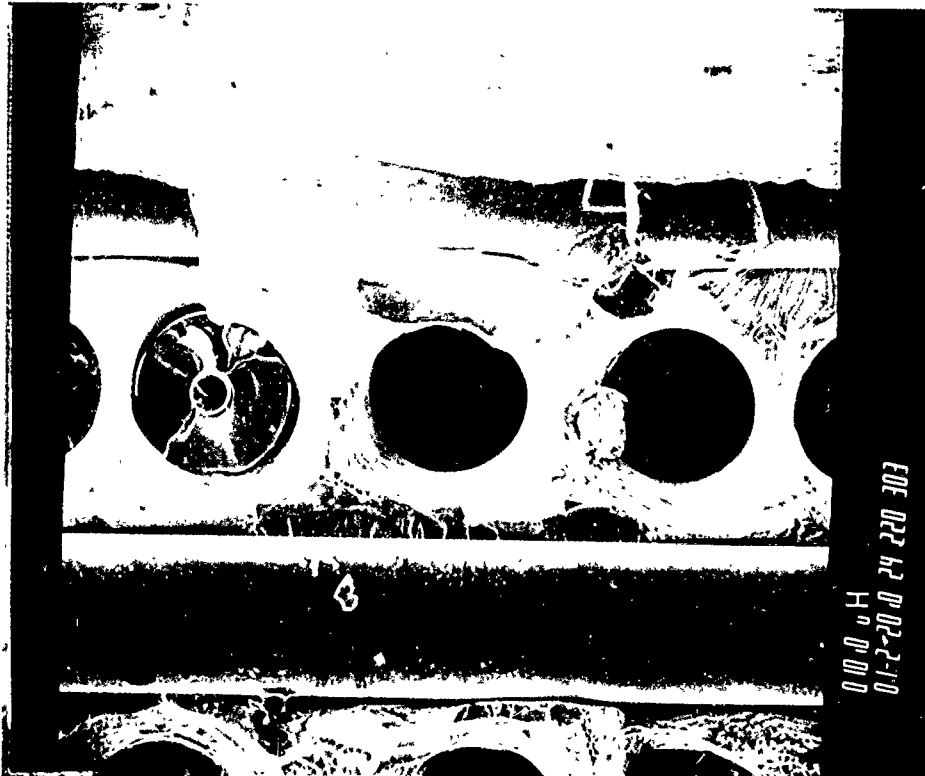


Figure 33. Magnification of Figure 32. Failure by Ductile Void Coalescence.

cleavage fracture. The types of matrix failure modes, based on the fracture surface evaluations of each specimen, is presented in Table IV.

Table IV. Matrix Failure Modes

TEST CONDITION	Ductile Void Coalescence	Cleavage Fracture
2.0 CPS		
375 MPa	Low	High
438 MPa	Low	High
500 MPa	Low-Moderate	Moderate-High
625 MPa	High	Low
0.0208 CPS		
438 MPa	High	Low
500 MPa	High	Low
542 MPa	High	Low

The specimen tensile tested at room temperature exhibited a slightly different type of fracture surface than the specimen tensile tested at 427°C. This matrix failure mode was primarily ductile void coalescence failure. Figures 34 and 35 are SEM micrographs of the fracture surface of this tensile tested (ambient temperature) specimen. Figure 35 is a magnification of Figure 34, bottom right. These micrographs show less debonding of the fiber-matrix interface: therefore, less fiber pullout as compared to the specimen tensile tested at 427°C. The micrographs also

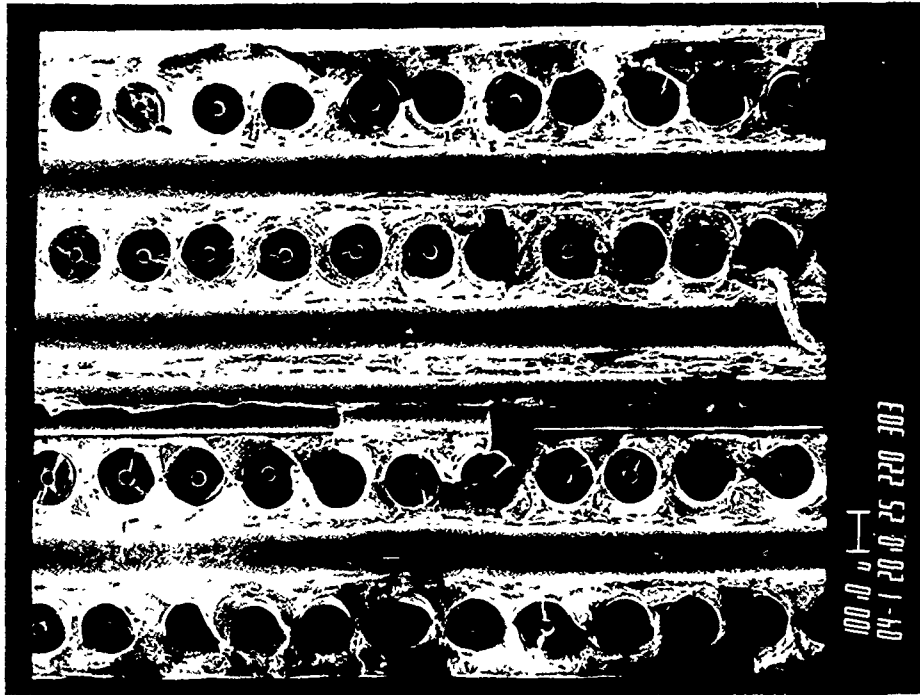


Figure 34. Fracture Surface of Specimen Tensile Tested at Room Temperature

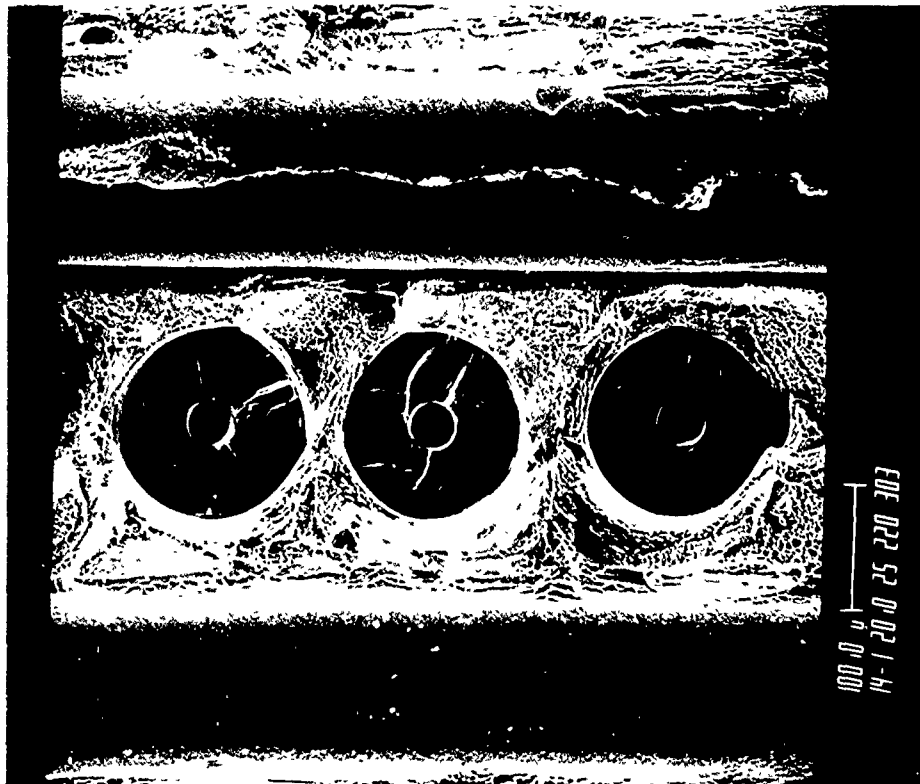


Figure 35. Magnification of Figure 34. Failure by Ductile Void Coalescence.

show that fracture occurred at the location of cross weave ribbons which hold the fiber mats together during the fabrication process.

The strategy of taking edge replicas during the course of the tests seemed to be a valid approach to assess the internal damage of specimens. No distinct differences were observed between the micrographic analysis of the fracture surface crack initiation points and matrix crack modes of the edges of any of the specimens with the analysis of the inner portion of the fracture surfaces. However, replica evaluations could not reveal fractured 90° fibers and debonding of 0° fiber-matrix interfaces. They did expose transverse matrix cracking of the 0° and 90° fibers, debonding of the 90° fiber-matrix interfaces, and fractured 0° fibers. In each case, crack initiation points and crack progression determined by replica evaluation compared well with the fractographic analysis of the fracture surfaces.

In several instances, transverse matrix crack progression was monitored during the fatigue testing at the precise location where the composite eventually failed. For example, on the 438 MPa high frequency specimen, transverse matrix cracking was observed via replica examination to initiate off the inner 90° fiber-matrix interface at 7500 cycles, Figure 36. Between 7500 and 10000 cycles (Figure 37), this crack propagated transversely across the 2 inner 90° plies to both of the 2 inner 0° plies and began

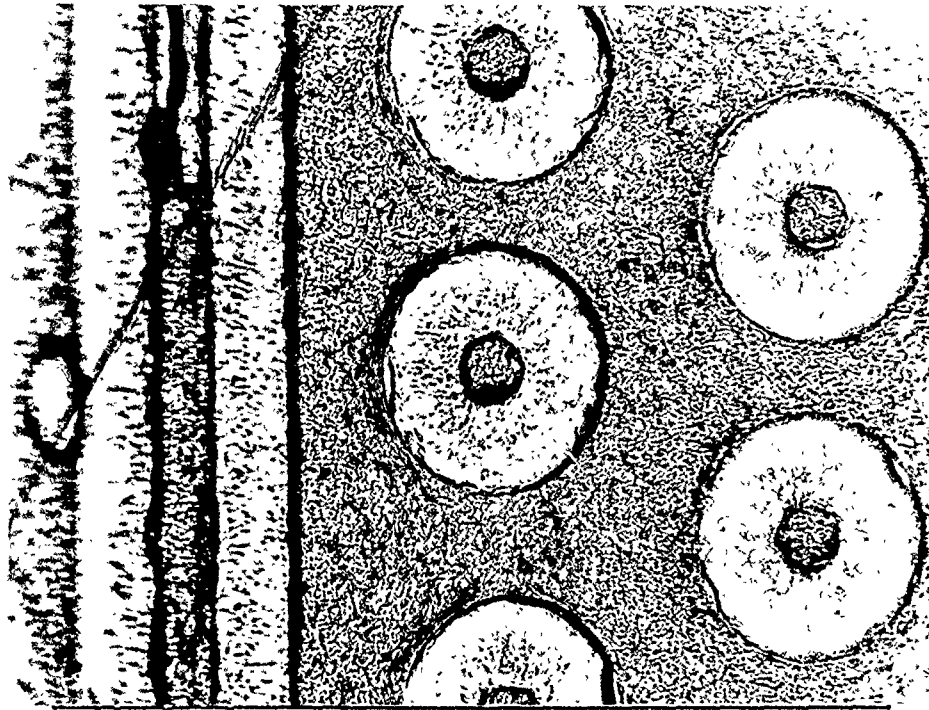


Figure 36. Matrix Crack Propagating to the Left of the Center 90° Fiber (438 MPa 2.0 CPS at 7500 Cycles)

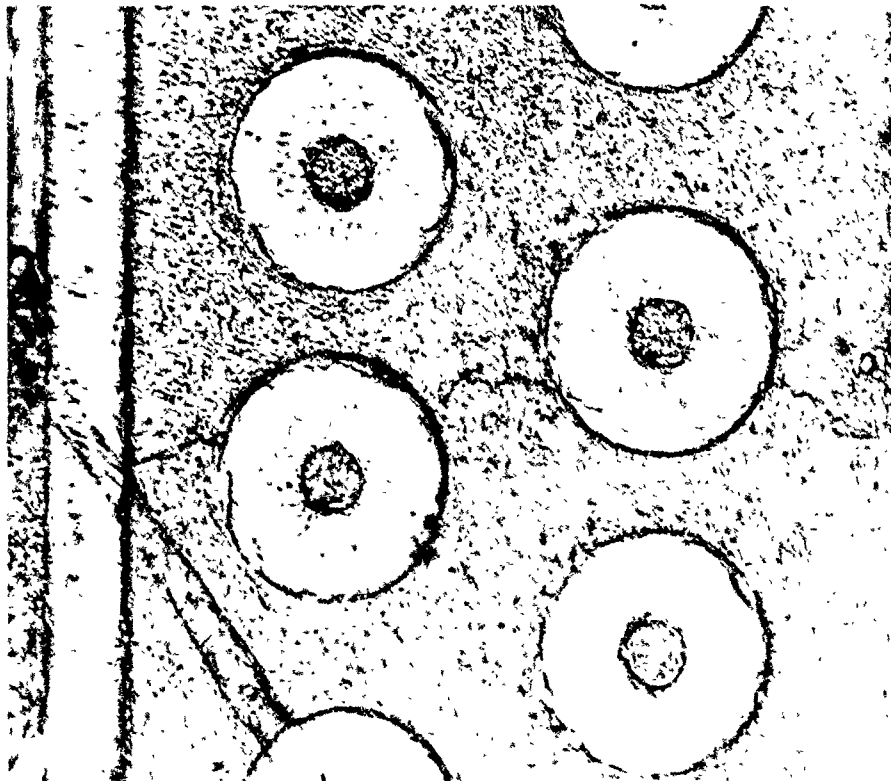


Figure 37. Crack Progressed Across the Inner 90° Fibers to Both Inner 0° Fibers (438 MPa 2.0 CPS at 10,000 Cycles)

debonding with the 90° fibers. At 12,500 cycles, the fiber-matrix interface region witnessed more severe degradation, Figure 38. At 13300 cycles the specimen failed at this same location, Figure 39. Therefore, the edge replicas were reflective of the composite damage as a whole.

The fiber-matrix interface zone was a common location of crack initiation. Figures 40 and 41 are SEM micrographic cross-sections of a fiber of the high frequency 500 MPa specimen. The black area in the center is the carbon core. The dark grey region surrounding this core is bulk SiC. The black outer ring around the SiC consists of alternating layers of carbon and silicon. Beyond this outer ring is the fiber-matrix interface or reaction zone. In Figure 41, the reaction zone can clearly be identified by its light (almost white) color and the irregular shaped edges. This reaction zone is formed by the interaction between the titanium matrix constituents and the fiber elements during the fabrication process. Within the reaction zone, the titanium matrix constituent is mostly titanium while the fiber constituents are primarily silicates and carbides.

Ermer (10:86-98) investigated the failure modes of several unidirectional SCS6/Ti-15-3 composites under thermal cycle conditions. He found that the thermal effects increased the irregularity and size of the edges of the reaction zones. Eventually, the reaction zones became extensively damaged with numerous microscopic cracks

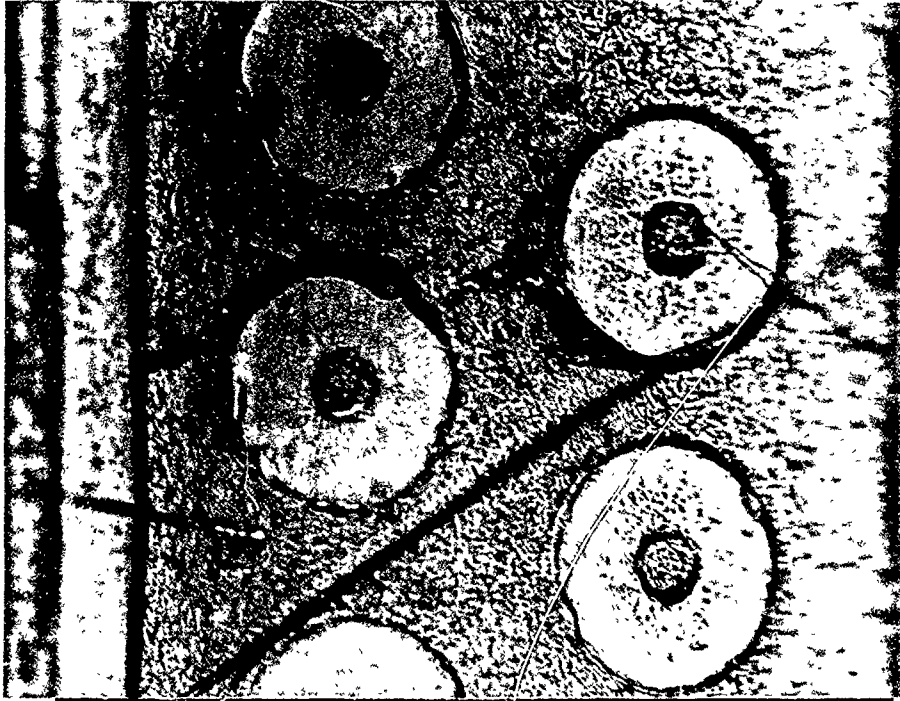


Figure 38. Damaged Fiber-Matrix Interface Zone. 90°  
Fibers Debonding with Matrix (438 MPa 2.0 CPS at 12,500  
Cycles)

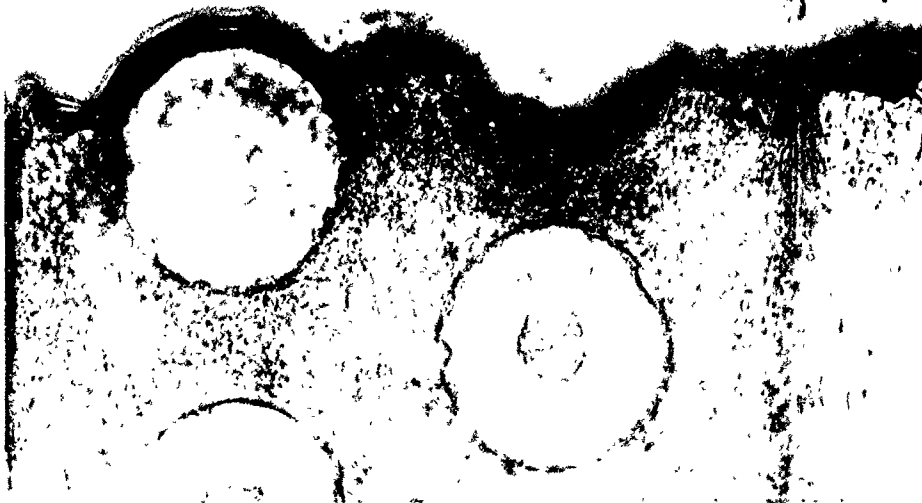


Figure 39. Edge at Final Fracture at 13,300 Cycles.  
Compare Fracture with Cracks on Figures 36 through 38  
(438 MPa 2.0 CPS)

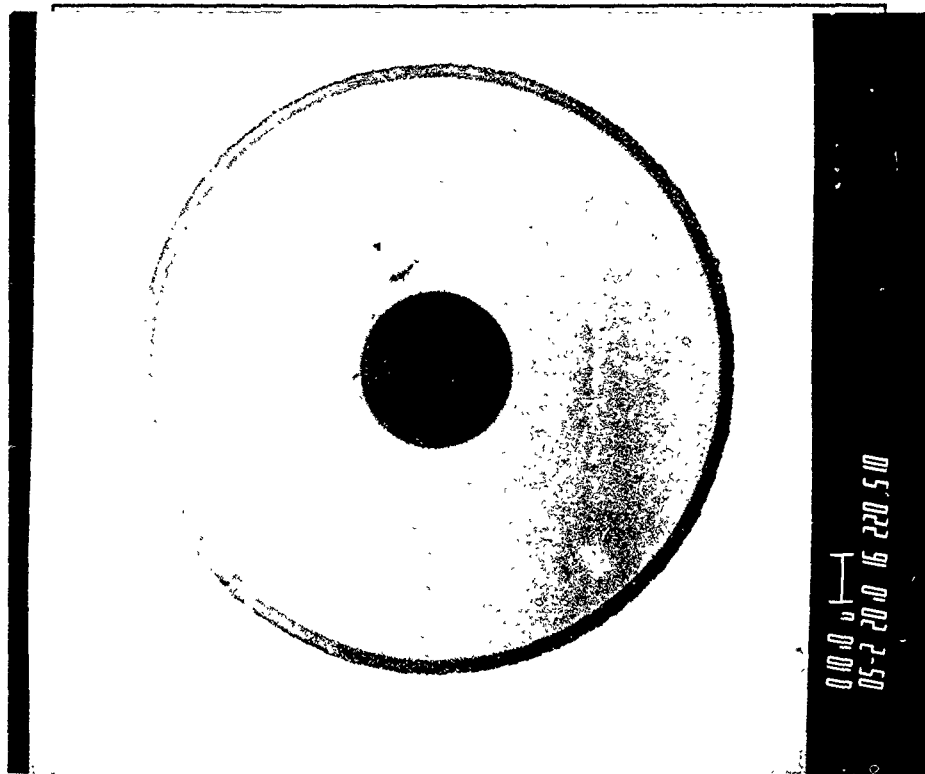


Figure 40. Micrograph of a 90° Fiber with Etched Surface Revealing Reaction Zone (500 MPa 2.0 CPS)



Figure 41. Magnification of Figure 40. Damaged Reaction Zone in the Region of the Crack

propagating both circumferentially around the fibers and perpendicular to the fibers.

The reaction zones of the isothermal fatigue tested specimens, which are the subject of this analysis, were not extensively damaged. However, the zone edges did become more irregular and increased in size with increased exposure time at 427°C. Figures 40 and 41 (as well as Figures 25 through 27) are SEM micrographs of the high frequency 500 MPa specimen fiber ends. During the duration of the test, the specimen was exposed to 427°C for about 1 hour. The reaction zones of these micrographs are less irregular and have about 1/2 of the depth of the reaction zones on the low frequency 542 MPa specimen. Compare the micrographs for the 542 MPa specimen, Figures 42 and 43, which was fatigued cycled at 427°C for 3 hours. On the other hand, the low frequency 438 MPa specimen had a life of about 10 hours at 427°C. The reaction zone depth of this specimen (Figure 44) averaged about 3 times that of the low frequency 542 MPa specimen.

The average reaction zone sizes were estimated for each fatigue tested specimen and are summarized in Table V. Figure 45, based on this tabulated data, identifies reaction zone sizes of selected fibers verses temperature exposure time. The zone dimensions appear to be approximately the same for the 0° and 90° fiber-matrix regions of a given specimen.

Table V. Fiber-Matrix Reaction Zone Sizes of Selected Specimens

STRESS LEVEL (MPa)	REACTION ZONE SIZE ( $10^{-5}$ mm)				TIME @ 427°C
	2.0 cps		0.0208 cps		
	0° fiber	90° fiber	0° fiber	90° fiber	
625	89.9	79.7			0.217
500	99.8	96.8			0.909
542			130	125	2.63
375		176			7.54
438			300	320	10.15

*Strain to Failure*

Maximum strain during the life of each specimen is plotted in Figure 46. The maximum strain at failure of the composite,  $\epsilon_{\text{CBIT}}$ , was 0.008 mm/mm for the specimens tested at 0.0208 cps. The maximum strain at failure for the high frequency specimens (excluding the 625 MPa specimen which failed at a strain of .007 mm/mm) was considerably lower at 0.0057 mm/mm. As was previously mentioned, the matrices of the high frequency 375, 438, and 500 MPa specimens were extensively damaged but with low fiber damage. These damage conditions can be a consideration for the theoretical calculations of the maximum composite strain at failure. The comparisons made here will be limited to the maximum strains obtained experimentally and the theoretical values of

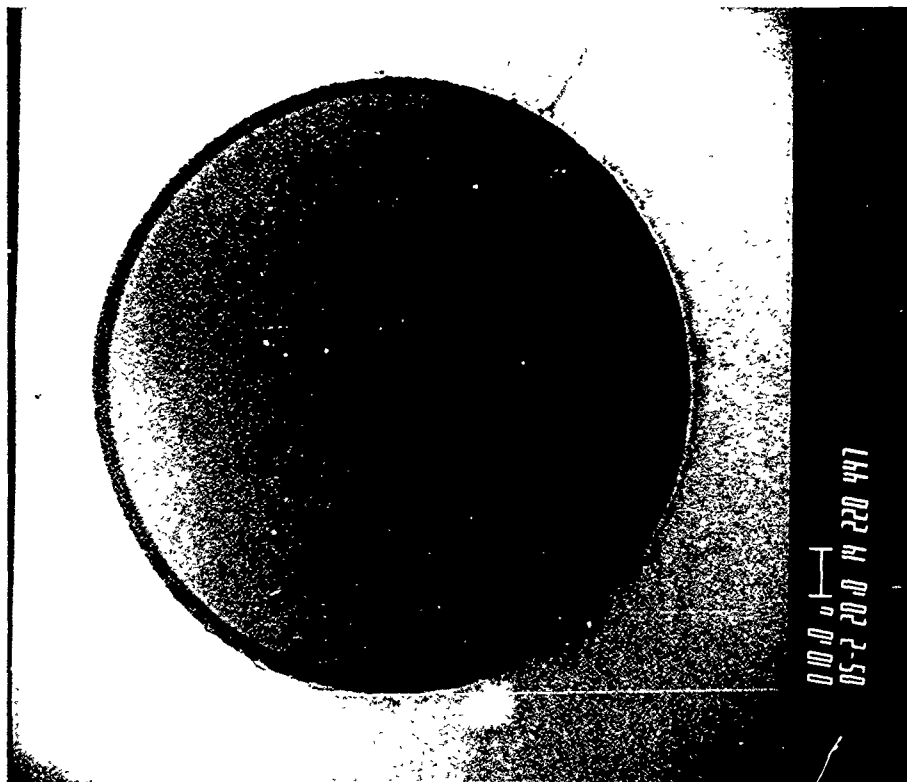


Figure 42. Micrograph of the 0° Fiber Reaction Zone of the Low Frequency 542 MPa Specimen Exposed to Temperature for 3 Hours

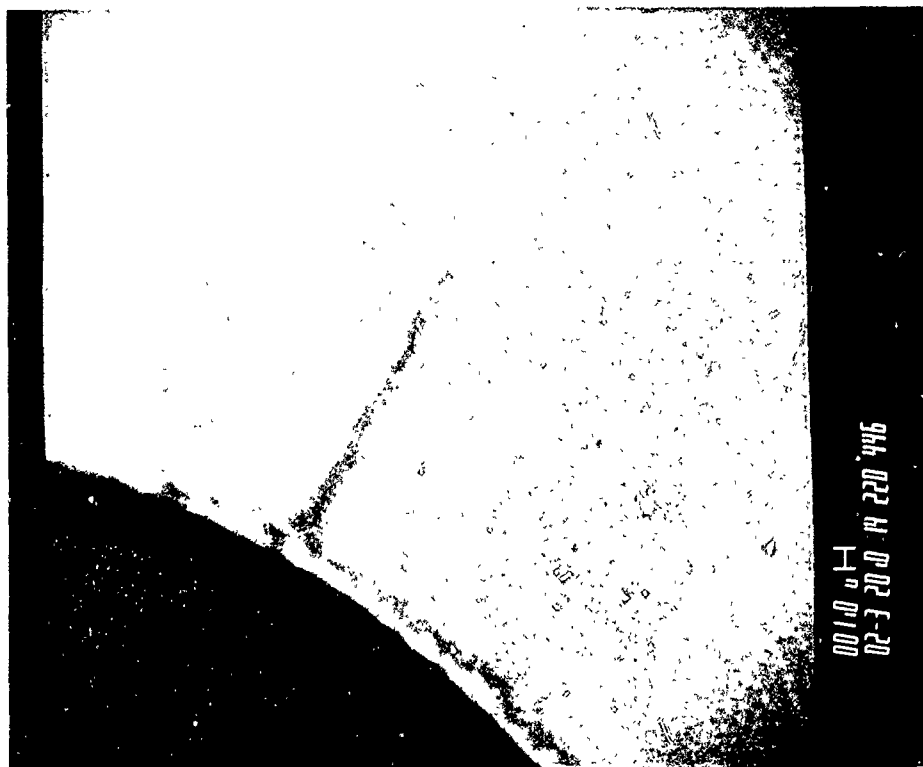


Figure 43. Magnification of Figure 42 (upper right)

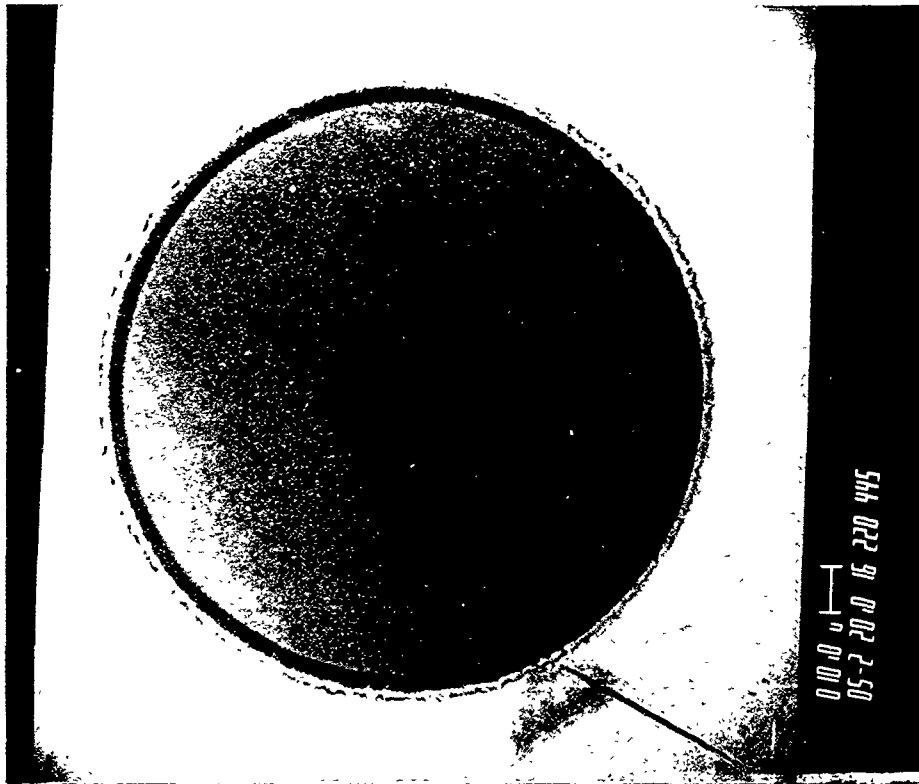


Figure 44. Micrograph of the 90° Fiber-Reaction Zone of the Low Frequency 438 MPa Specimen Exposed to Temperature for 10 Hours

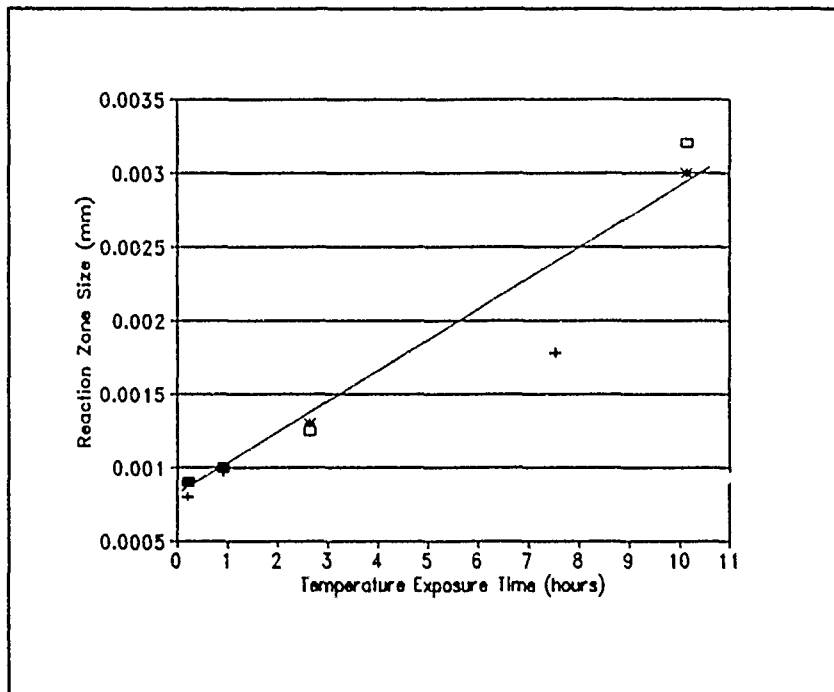


Figure 45. Reaction Zone Sizes Increase with Increasing Exposure to Temperature

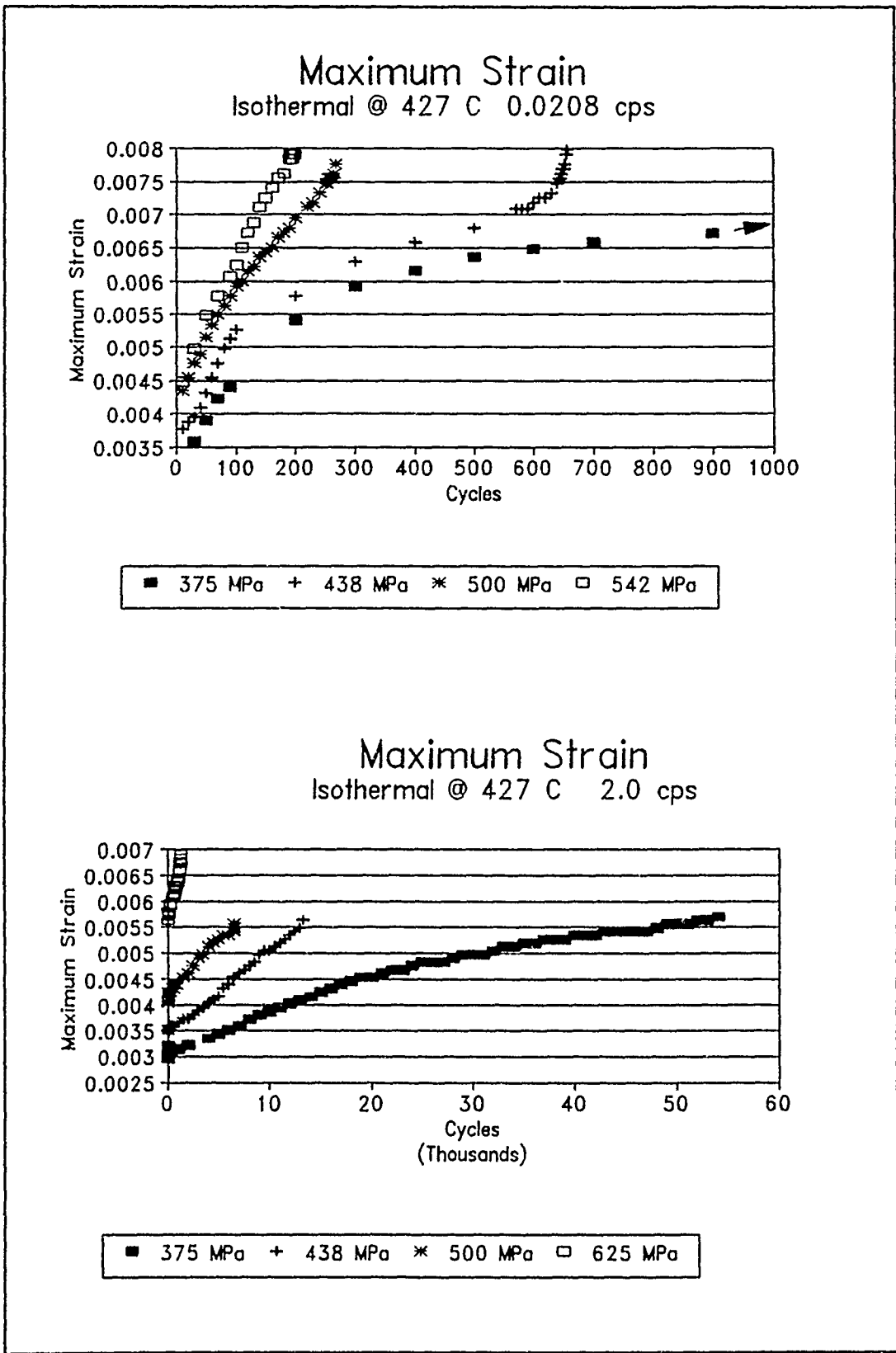


Figure 46. Maximum Strain to Failure

maximum tensile strains under specified damage conditions.

Just prior to the failures of the high frequency specimens, the fibers deformed elastically while the matrix deformed plastically. Since the fibers are relatively brittle as compared to the matrix, the fiber failure strain may be approximated to be equal to the matrix failure strain (11:128):

$$\epsilon_{cmax} = \epsilon_{fmax} = \epsilon_{mmax} \quad (1)$$

or:

$$\frac{\sigma_{cmax}}{E_c} = \frac{\sigma_{fmax}}{E_f} = \frac{\sigma_{mmax}}{E_m} \quad (2)$$

$$\epsilon_{cmax} = \frac{\sigma_{cmax}}{E_c} \quad (3)$$

where  $\sigma_{cmax}$  is the maximum composite strength. The maximum strength of the composite material was found to be 736 MPa from the 427°C tensile test results. (See the tensile test results in the section titled *Tensile Tests*.) The initial modulus of the composite,  $E_c$ , was determined from the experimental results of the high frequency fatigue tests. Using these values in Eq (3) and assuming elastic behavior,  $\epsilon_{cmax}$  is 0.00544 mm/mm. This is within 5% of the actual failure strain for the high frequency specimens.

Though the actual composite strength of fatigued specimens would be lower than the tensile strength, the intent here is to determine maximum tensile strains under

specific damage conditions. Micrographic analysis of the high frequency specimens has revealed low fiber damage and moderate to high matrix damage just prior to failure. Therefore, the maximum composite strain should be slightly higher than the maximum fiber strain.

From the rule of mixtures for a composite material where both the fibers and matrix deform elastically:

$$E_c = E_f \cdot V_f + E_m (1 - V_f) \quad (4)$$

These relationships were developed for a unidirectional composite material. They can be applied to a [0/90] lay-up which behaves elastically if the mechanical properties of the 90° fiber plies are assumed to approximate the matrix properties. (The load direction is in the direction of the 0° fibers.) Accordingly, only the 0° fibers are considered when determining the volume fraction of the fibers. Though the actual volume fraction is 38%, the effective volume fraction is 38%/2 for this [0/90]<sub>1</sub> lay-up.

But the matrix of the high frequency specimens deformed plastically and Eq (3) assumed elastic strain. A closer approximation of the rule of mixtures considering matrix plasticity:

$$E_c = E_f \cdot V_f + (d\sigma_m / d\epsilon_m)_{\epsilon_{max}} (1 - V_f) \quad (5)$$

where  $(d\sigma_m / d\epsilon_m)_{\epsilon_{max}}$  is the slope of the stress-strain curve of the matrix just prior to failure. Generally, composites which have brittle fibers, fracture at the fracture strain

of the fibers. Failure initiation occurs when the fibers are strained to their fracture strain such that the ultimate strength of the composite can be predicted. From Eqs (1) and (5):

$$\sigma_{cmax} = \sigma_{fmax} \cdot V_f + (\sigma_m)_{e_{fmax}} \cdot (1 - V_f) \quad (6)$$

where  $\sigma_{cmax}$  is the maximum composite stress.

$\sigma_{fmax}$  is the maximum fiber stress.

$(\sigma_m)_{e_{fmax}}$  is the matrix stress at a strain equal to the maximum strain of the fiber.

or:

$$\sigma_{cmax} = E_f \cdot e_{cmax} [V_f + E_m/E_f (1 - V_f)] \quad (7)$$

$$e_{cmax} = \frac{\sigma_{cmax}}{E_f [V_f + \frac{E_m}{E_f} (1 - V_f)]} \quad (8)$$

The modulus values for the matrix  $E_m$ , and fibers  $E_f$ , are 86.6 GPa and 360 GPa respectively. These modulus values were linearly interpolated for 427°C from values at 300°C and 550°C presented by Majumdar et al. (4:15) and Gayda et al (2:11).

Using these values in Eq (8),  $e_{cmax}$  is 0.0053 mm/mm which compares within 7% of the actual maximum strain value for the high frequency fatigue tests. Therefore, the elastic deformation assumption (Eq (3)) is applicable for estimating the maximum failure strain. Also, since the calculated results using Eq (8) were close to the actual failure

strain, the assumption that the composite failure strain is approximately equal to the fiber fracture strain for the high frequency fatigue tests holds true.

Fracture surface evaluation of the specimen tensile tested at 427°C indicated extensive fiber damage preceding matrix failure. Similarly, for the low frequency fatigue tested specimens with predominant fiber damage and low to moderate matrix damage prior to failure. Since the fibers broke first followed by matrix failure, the volume fraction of the fibers is assumed to be approximately zero just prior to composite fracture. Using the relationships of Eqs (2) and (3) for an elastic matrix strain assumption:

$$\epsilon_{\text{cmax}} = \frac{\sigma_{\text{cmax}}}{E_m} = 0.0085 \quad (9)$$

This maximum strain value is within 12% of the actual failure strain of the tensile tested specimens and within 6% of the failure strain of the low frequency specimens. Therefore, the assumption that fiber fracture preceded matrix failure yields a value close to the actual failure strain.

#### *Average Strain*

The cyclic mean strain for both groups of fatigue tests is plotted in Figure 47. The initial slopes of these curves are, for the most part, linear. This indicates that little ratcheting (due to creep) has occurred during the early life

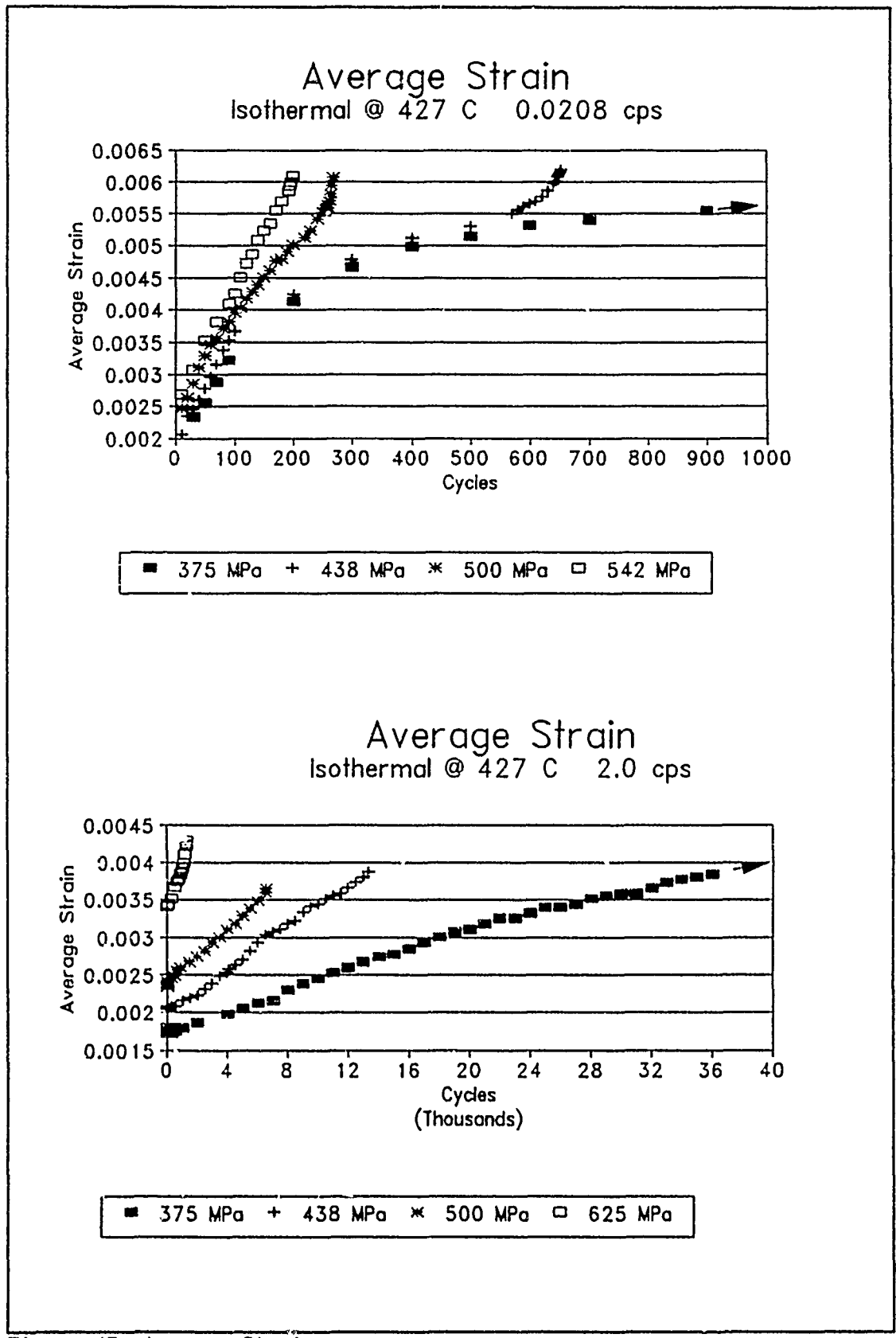


Figure 47. Average Strain

of the fatigue tested specimens. The exception is the high frequency 625 MPa specimen which has a high initial creep rate up to about 100 cycles.

### *Strain Range*

Though modulus degradation (based on stress-strain data) was used in this analysis to determine cyclic damage, strain range is also suitable for measuring modulus degradation. The calculated strain range for the 8 specimens fatigue tested is presented in Figure 48. As will be discussed in detail in the section titled *Modulus Curves*, the low frequency specimens began to age harden at about 60 to 100 cycles. This age hardening is also evident on the strain range curves.

### *Modulus Curves*

Modulus trends during the life of a material are useful for assessing damage in composites. In this section, modulus degradation is expressed in terms of damage. In the next section, the damage modes are then determined for each specimen tested and compared with the specimen failure mechanisms from fracture surface evaluation results discussed previously.

The modulus was calculated over the lives of the specimens from stress-strain cycle data collected during the tests. These modulus curves are characteristically different for each of the two groups of tests at high and

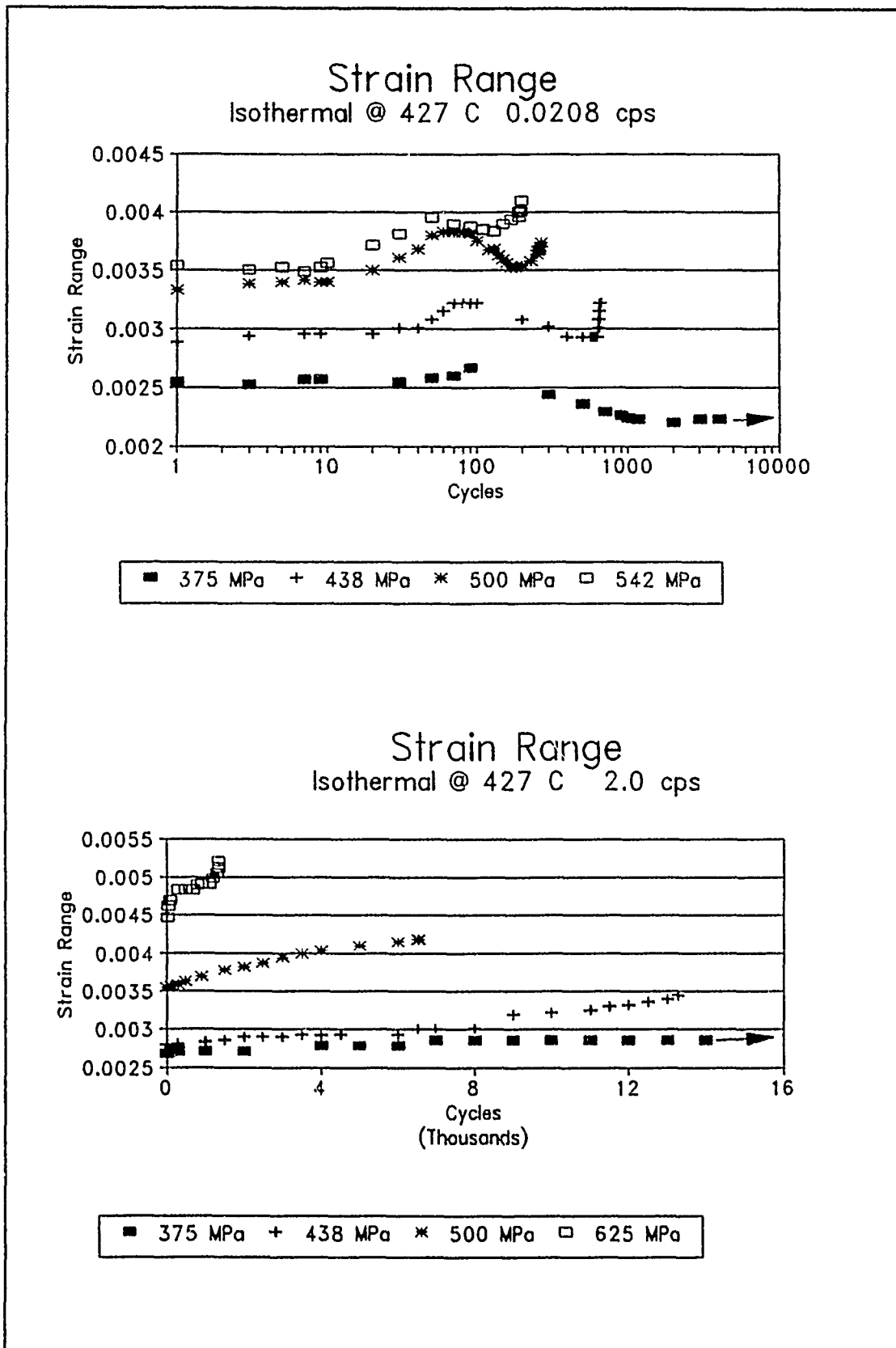


Figure 48. Strain Range

low frequencies (Figure 49). The high frequency modulus values continually decrease while the low frequency values decrease to about 60 to 80 cycles then begin to increase to a point followed by rapid modulus degradation. One major reason for the differences is due to dramatically different exposure times to high temperature for each group of tests. Therefore, modulus verses exposure time is plotted in Figure 50 for comparison over the life of each specimen. The low frequency curves in this figure also show that the same three trends in modulus.

For the 4 specimens tested at 0.0208 cps, modulus degradation over the first 80 cycles (1 hour) is probably caused by creep of the matrix and fiber damage; with minimal creep rates typically expected at the lower loads but increasing at the higher loads. Virtually no fiber damage is expected at the lower loads but increases at the higher loads. At about 80 cycles, the onset of age hardening begins to cause the modulus of these four specimens to increase. This age hardening is due to the titanium matrix phase change from beta (body centered cubic crystal structure) to alpha (hexagonal close-packed structure) and continues to a point of rapid modulus degradation. This trend is more clearly evident with the specimen tested at 0.0208 cps, 375 MPa maximum stress (Figure 49 top). For this specimen, the age hardening begins at about 80 cycles and continues over the next 3,000 cycles. At about 3,000 cycles rapid modulus

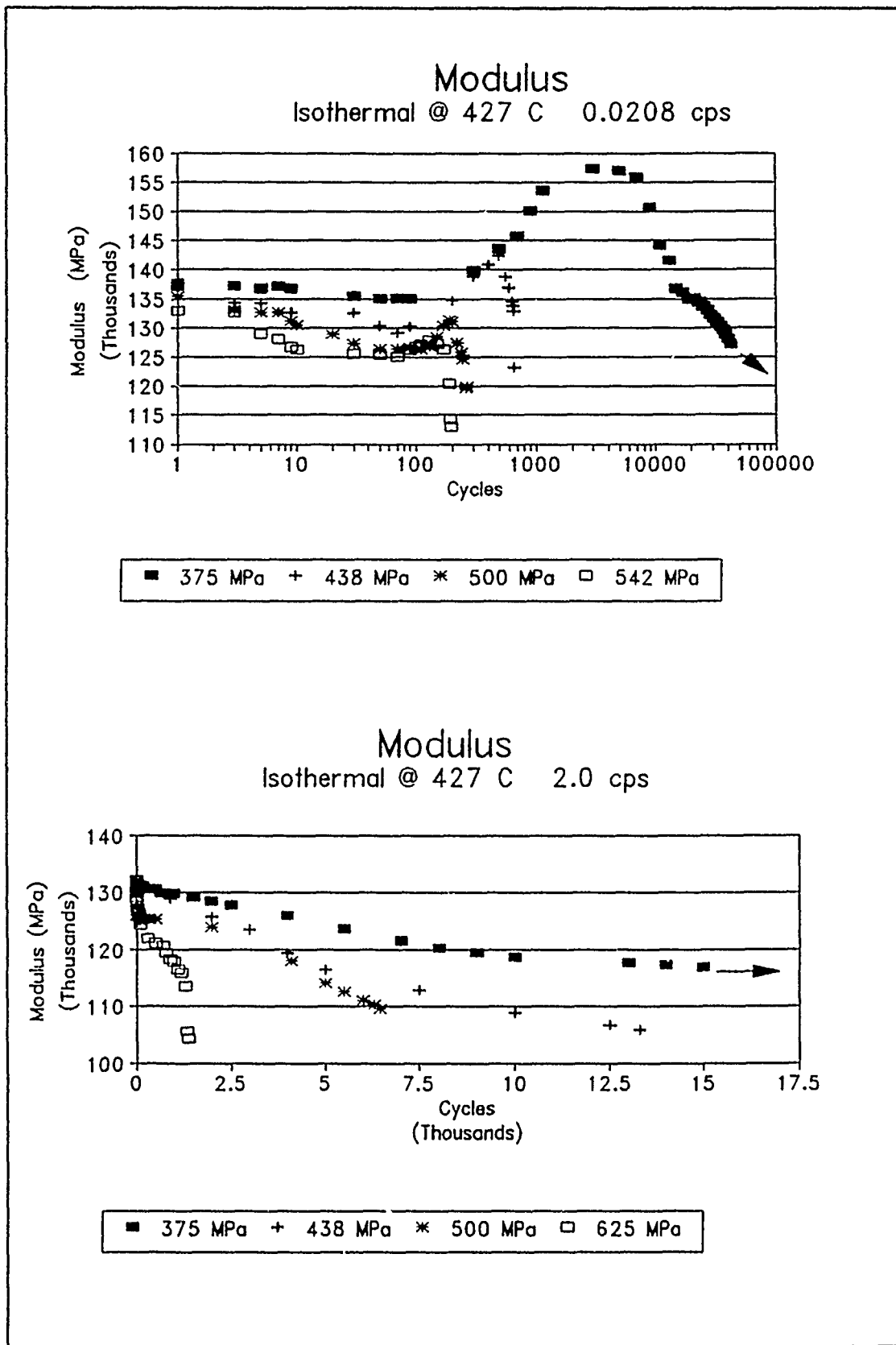


Figure 49. Changing Modulus Over Cycles

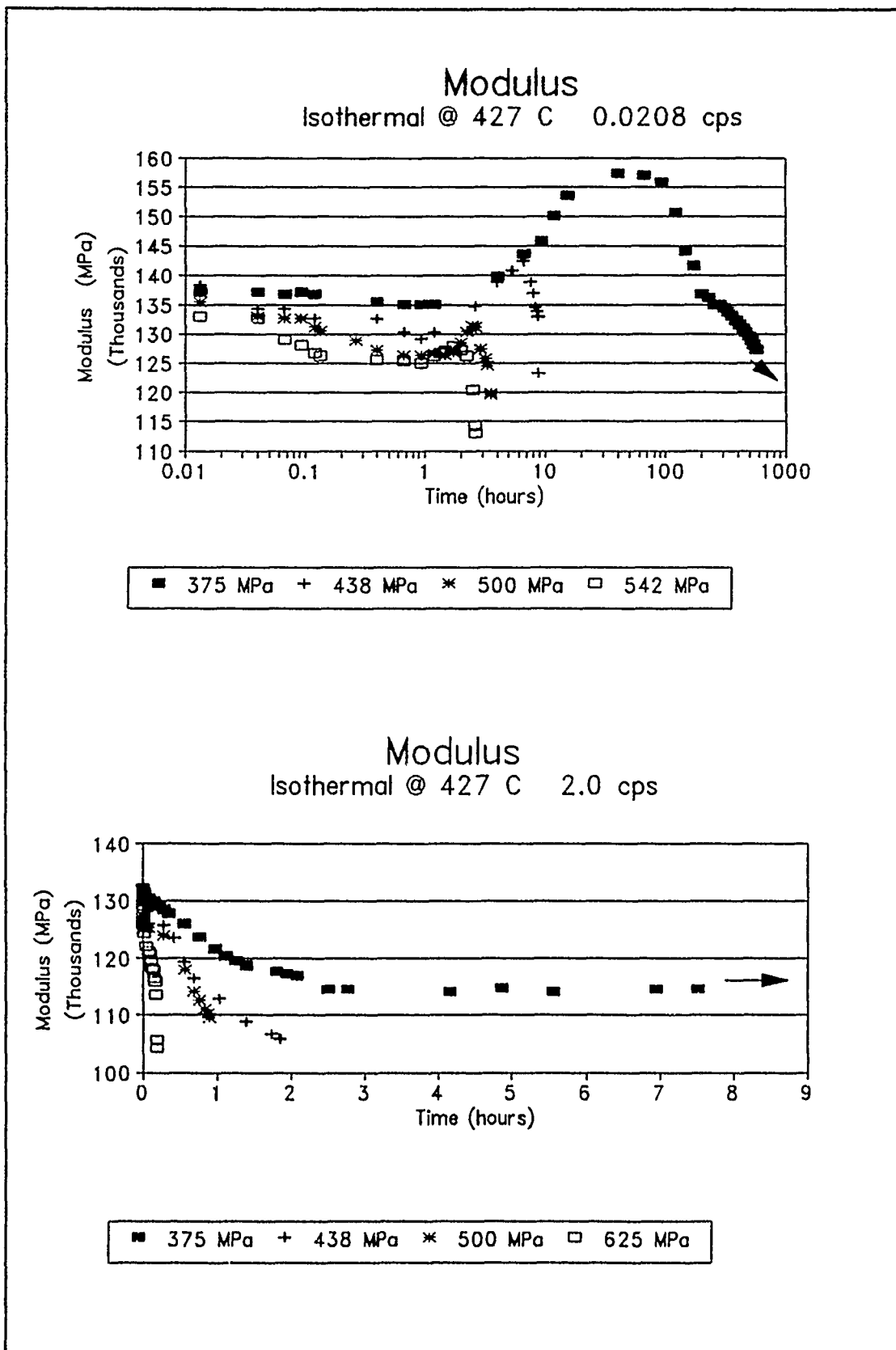


Figure 50. Changing Modulus Over Time

degradation starts and continues to specimen failure.

To assess the fatigue damage over the life of each specimen, the modulus increase due to age hardening needs to be eliminated as a variable. This is accomplished in 3 parts. First, the modulus behavior of each curve over the first 80 cycles is determined in the form of an equation for each curve. Second, each of these equations are extrapolated to the point of rapid modulus degradation, i.e., to the point where age hardening is no longer the dominant factor effecting the modulus. This is 3,000 cycles for the 375 MPa curve, Figure 49. Third, the rapid modulus degradation portion of each curve is shifted downward to its respective point which was extrapolated out from the first 80 cycles.

This approach to eliminate age hardening is appropriate if the dominating factors which influence the modulus still prevail on the revised curves. Since there is potential for masking changes in material characteristics which effect the modulus over the extrapolated region (from 80 cycles to the point of rapid modulus degradation), further discussion of the characteristic changes taking place in this region is warranted.

The three factors which influence the behavior of the modulus over this region are age hardening, fatigue damage, and creep and are depicted in Figure 51. Though age hardening dominates in the change in modulus behavior, damage due to creep and fatigue does occur. The fatigue

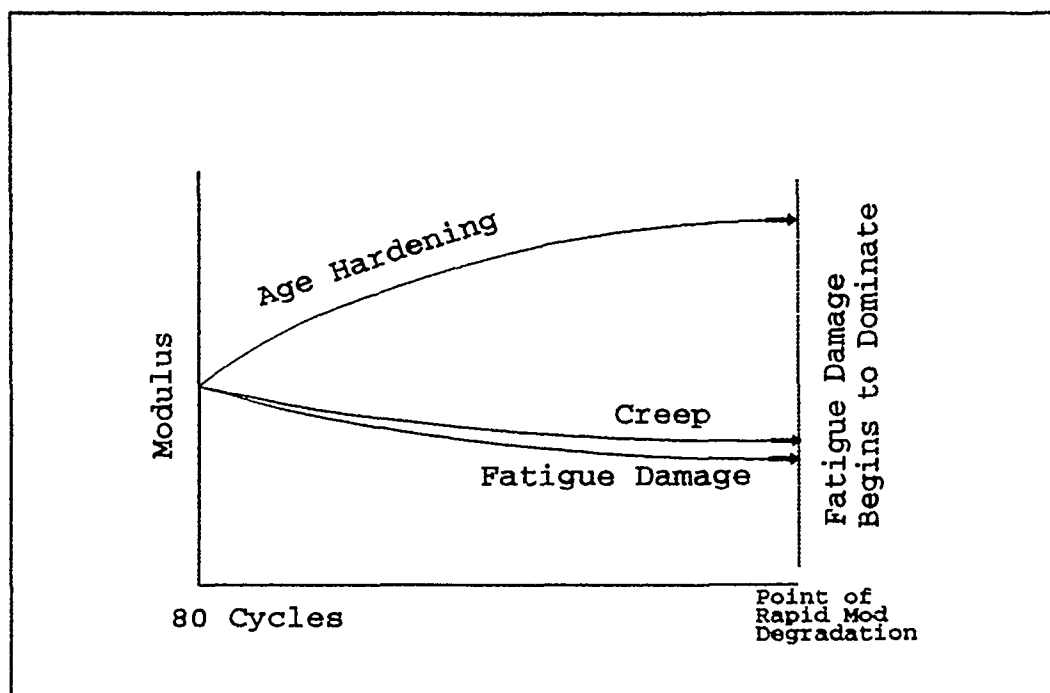


Figure 51. Factors Influencing Modulus Behavior

damage is due to fractured fibers or matrix cracking or both. If fractured fibers are assumed to be the predominant damage mechanism over the first 80 cycles, this damage will eventually saturate and matrix cracking will then dominate. As a result, the third region of the modulus curve will be reflective of matrix cracking (and possibly creep). The reverse can be said if matrix cracking is the initial predominant damage mechanism. Consequently, neither damage modes can be masked by the extrapolation process.

For a closer look at material characteristic changes caused by creep, Rogacki and Tuttle (12:89-94) conducted creep tests on Ti-15-3 under test conditions which happen to be useful for determining creep trends of these specimens. Figure 52 represents creep response over time to the

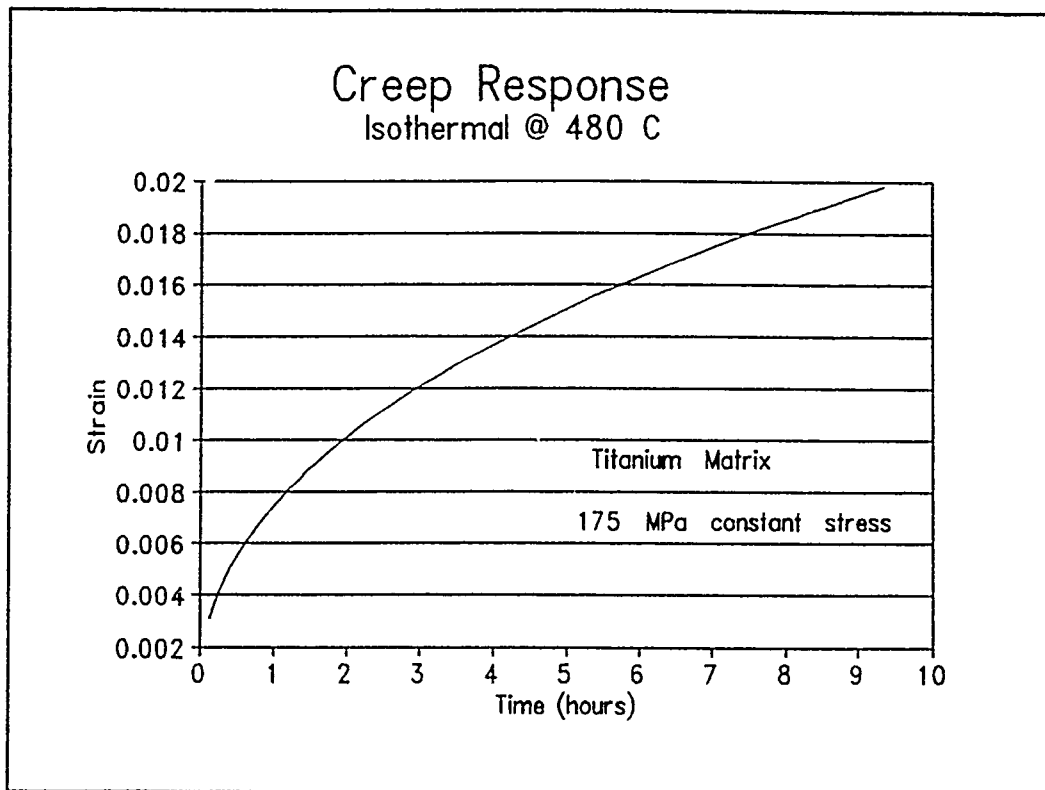


Figure 52. Creep Response of the Ti-15-3 Matrix material (12:92)

equation:

$$\epsilon = 2.14 \cdot 10^{-4} \cdot t^{0.434} \quad (10)$$

This relation was developed from data presented by Rogacki and Tuttle for Ti-15-3 at 480°C with a constant load of 175 MPa,  $\epsilon$  is the strain and  $t$  is time (seconds). This curve is comparable to what would be expected for creep response of the titanium matrix for the 375 MPa maximum stress (i.e., 187 MPa mean stress) specimen. The curve shows that the creep rate decreases fairly rapidly within the first hour then is mostly linear beyond the first hour. Therefore, any trends due to creep damage of the 375 MPa specimens should be established within the first hour of

test. Hence, linearly extrapolating the creep rate beyond 1 hour should represent a close approximation of creep damage within the second region (from 80 cycles to the point of rapid modulus degradation) of the modulus curves. In Figure 53, the dominant causes of changing modulus are described for the low frequency 375 MPa specimen over the 3 regions.

For the other three low frequency specimens creep and fatigue damage can be expected to be higher than the 375 MPa specimen over the first hour with creep rates approximately linear beyond one hour. Fatigue damage is also expected to increase for the higher stressed specimens. Specifically, the 542 MPa specimen is expected to have dominant fatigue damage compared to creep beyond the first hour. Also, damage trends beyond the first hour are assumed to be linear to the point of rapid modulus degradation.

The approach used to eliminate the age hardening from the 0.0208 cps 375 MPa modulus curve is presented here. This curve, Figure 53, was partitioned into 3 regions. The first region, 0 to 80 cycles, behaves according to the equation:

$$E_n^1 = E_o - 0.21 \cdot C_n \quad (11)$$

where  $E_n$  is the instantaneous modulus at a given cycle  $c_n$ , and  $E_o$  is the initial modulus.

The modulus increases over the second region, 80 to 3,000 cycles, can be expressed as the following equation:

$$E_n^2 = 19285 + 3.19 \cdot C_n - 0.0007 \cdot C_n^2 \quad (12)$$

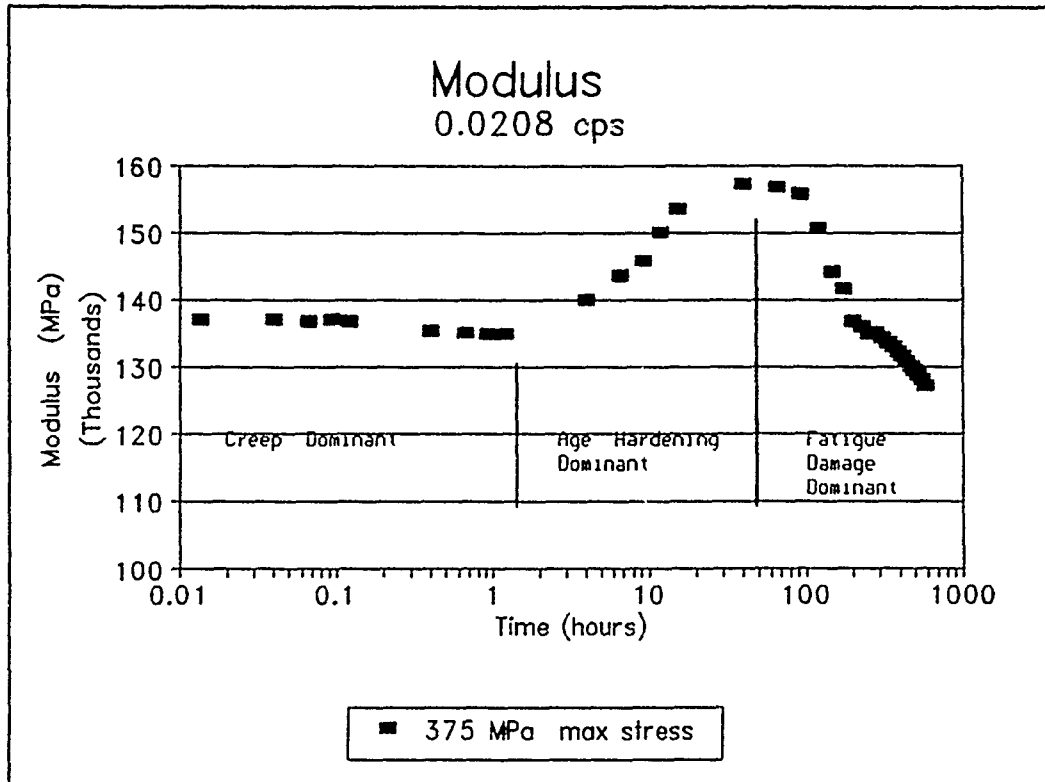


Figure 53. Dominant Influences on the modulus Over the Life of the 375 MPa Specimen

Eq (12) is the characteristic hardening curve which applies to all four low frequency specimens.

Over the third region, 3,000 to 40,000 cycles, the modulus decreases to the equation:

$$E_n^3 = 17350 + 4.41 \cdot 10^7 / c_n - 8.65 \cdot 10^{10} / c_n^2 \quad (13)$$

The reduced modulus curve for this specimen is obtained by extrapolating Eq (11) to 3000 cycles then translating Eq (13) to the modulus at 3,000 cycles obtained from Eq (11).

For 3,000 to 40,000 cycles:

$$E_n = E_n^3 - (E_n^2 - E_n^1) \quad (14)$$

where  $E_n$  is the instantaneous modulus after taking into

account the effects of creep and age hardening.

For the remaining three low frequency modulus curves, the hardening effects were eliminated in the following manner. Since Eq (12) is representative of age hardening for all four specimens from 80 cycles to failure:

$$E_n = E_i + E_{nc}^1 - E_n^2 \quad (15)$$

where  $E_i$  is the instantaneous modulus after the age hardening  $E_{nc}$  are extrapolated modulus values for each curve based on linear "best fit" equations linearly extrapolated beyond 80 cycles. These are:

$$E_{nc}^1 = E_o - 2.75 \cdot C_n \quad (16)$$

for 0.0208 cps 438 MPa

$$E_{nc}^1 = E_o - 3.06 \cdot C_n \quad (17)$$

for 0.0208 cps 500 MPa

$$E_{nc}^1 = E_o - 4.59 \cdot C_n \quad (18)$$

for 0.0208 cps 542 MPa

where  $E_o$  is the initial modulus which was averaged over these specimens to be 135 GPa. The group of fatigue tests conducted at 2.0 cps were not appreciably effected by age hardening with the exception of the 375 MPa specimen beyond 8,000 cycles. The modulus curve for this specimen has a prominent "knee" at about 3,000 cycles (Figure 49) or about 1.5 hours (Figure 50) which may be caused by the onset of age hardening. The reduced modulus curves representing the

damage without age hardening are presented in Figures 54 and 55.

#### *Modulus Degradation as Fatigue Damage*

The next step to determine quantitatively the fatigue damage over the life of each specimen is to define damage, D

$$D=1-E/E_0 \quad (19)$$

where E is the instantaneous modulus represented on Figures 54 and 55 and E<sub>0</sub> is the initial modulus.

Since fatigue damage is time dependent (time exposure to temperature) as well as cycle dependent, damage was also plotted as a function of time, Figures 56 and 57. Damage was then expressed based on the percent of life of each specimen. Here, the life of the 375 MPa low frequency specimen was assumed to be equal to 720 hours (54,000 cycles), although this specimen did not fail.

Comparing the low frequency and high frequency tests on Figure 58, it is clear that damage progression is considerably different for each of the two groups of tests with the exception of the 375 MPa maximum stress specimens. The initial faster rate of increase in damage (Figure 58) for the two 375 MPa specimens and the 438 MPa high frequency specimen, is indicative of transverse matrix cracking and minimal fractured fibers during the duration of the tests. The microscopic and SEM micrographic evaluation results of the sectioned and fracture surfaces for these tests

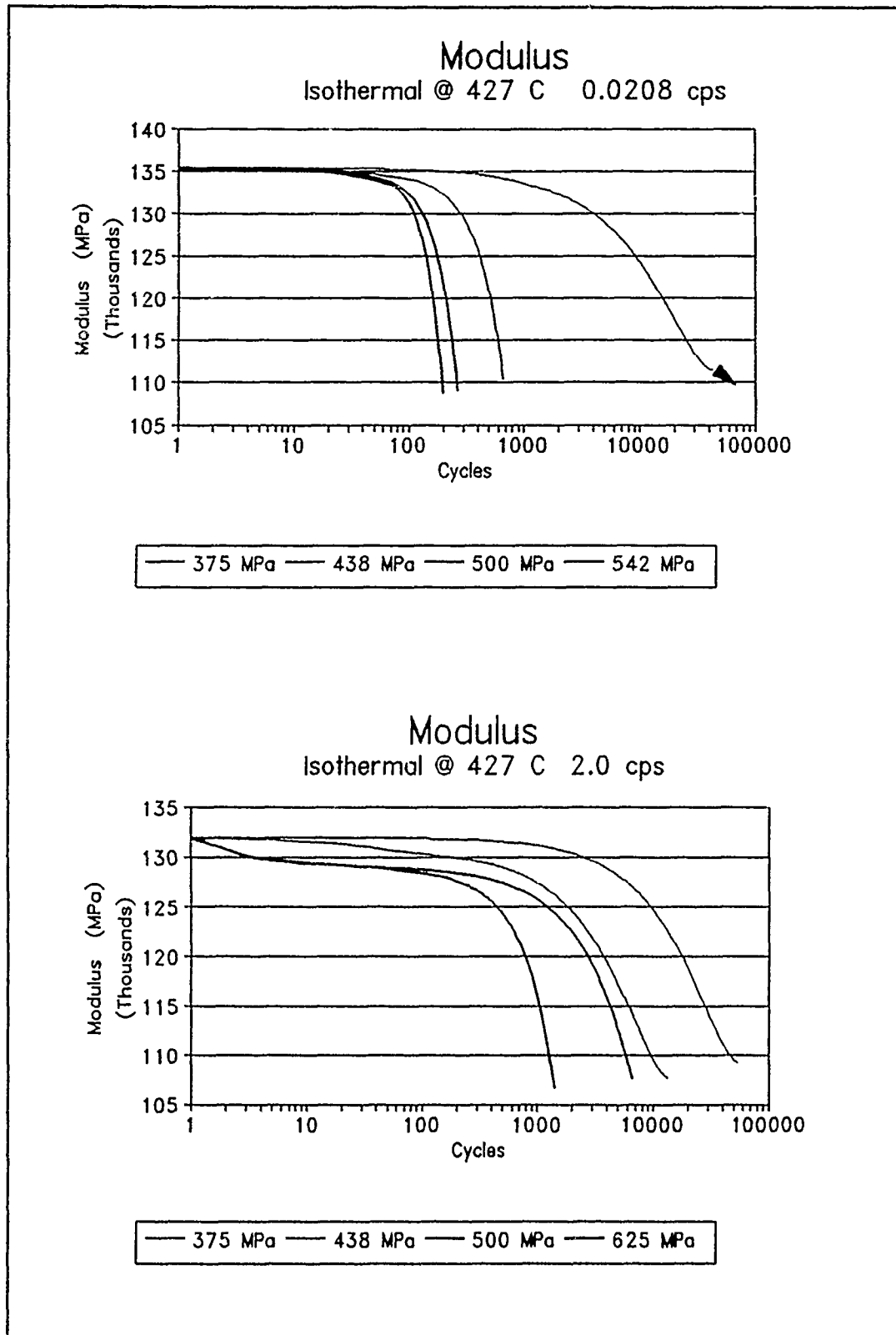


Figure 54. Modulus Curves with Age Hardening Eliminated as a Variable

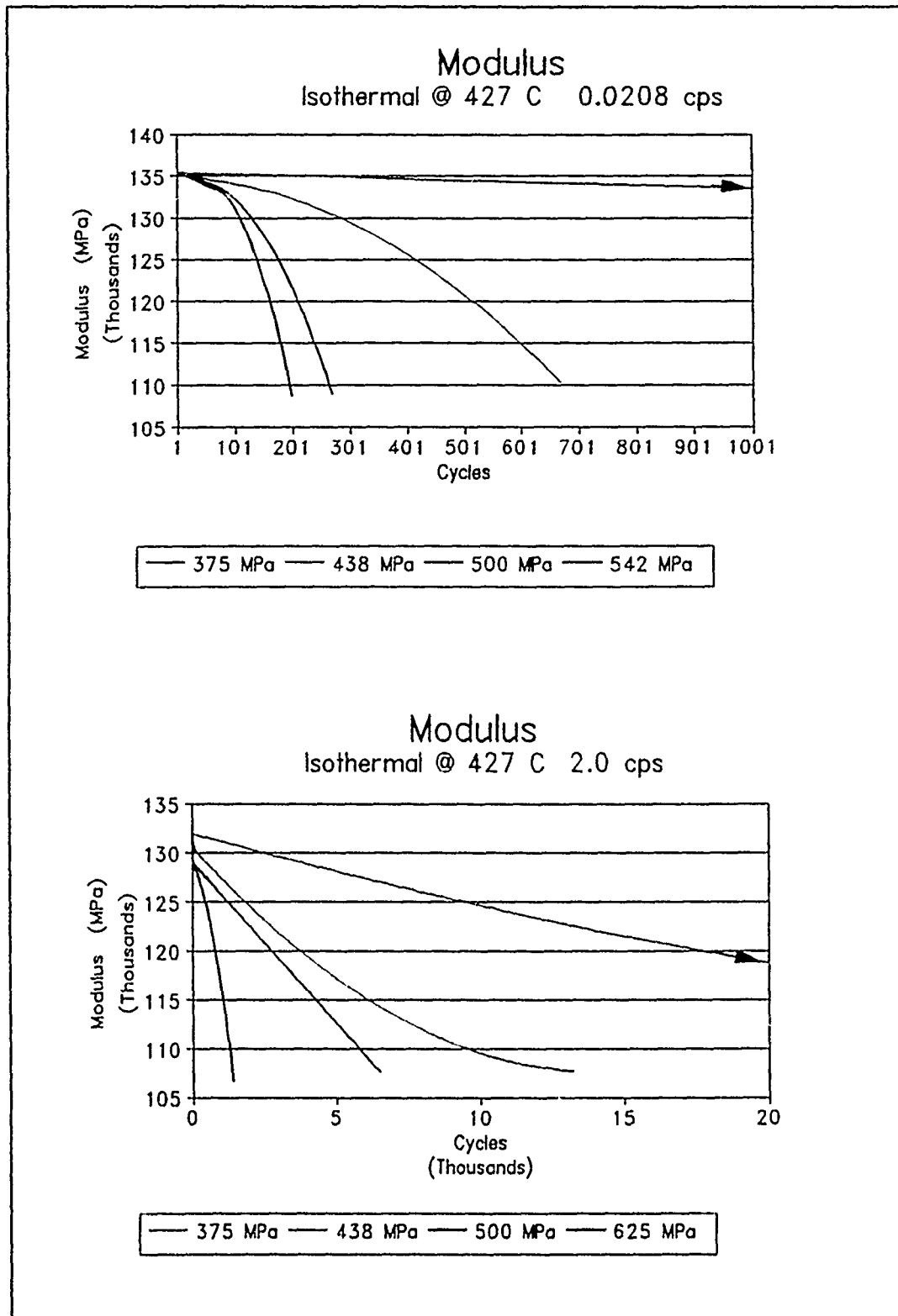
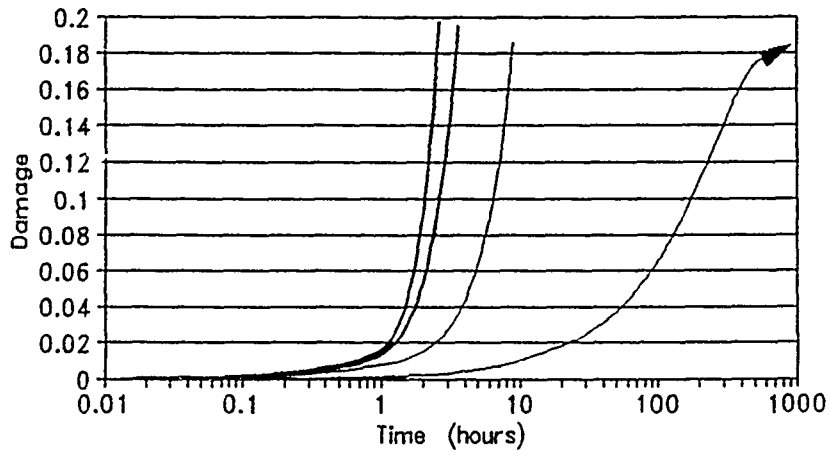


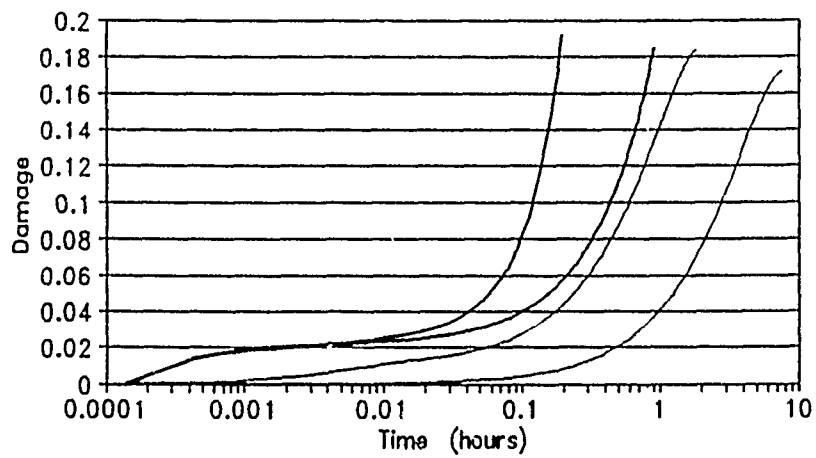
Figure 55. Modulus Curves with Age Hardening Eliminated as a Variable

Damage  $D = 1 - E/E_0$   
isothermal @ 427 C 0.0208 cps



— 375 MPa — 438 MPa — 500 MPa — 542 MPa

Damage  $D = 1 - E/E_0$   
isothermal @ 427 C 2.0 cps



— 375 MPa — 438 MPa — 500 MPa — 625 MPa

Figure 56. Specimen Fatigue Damage

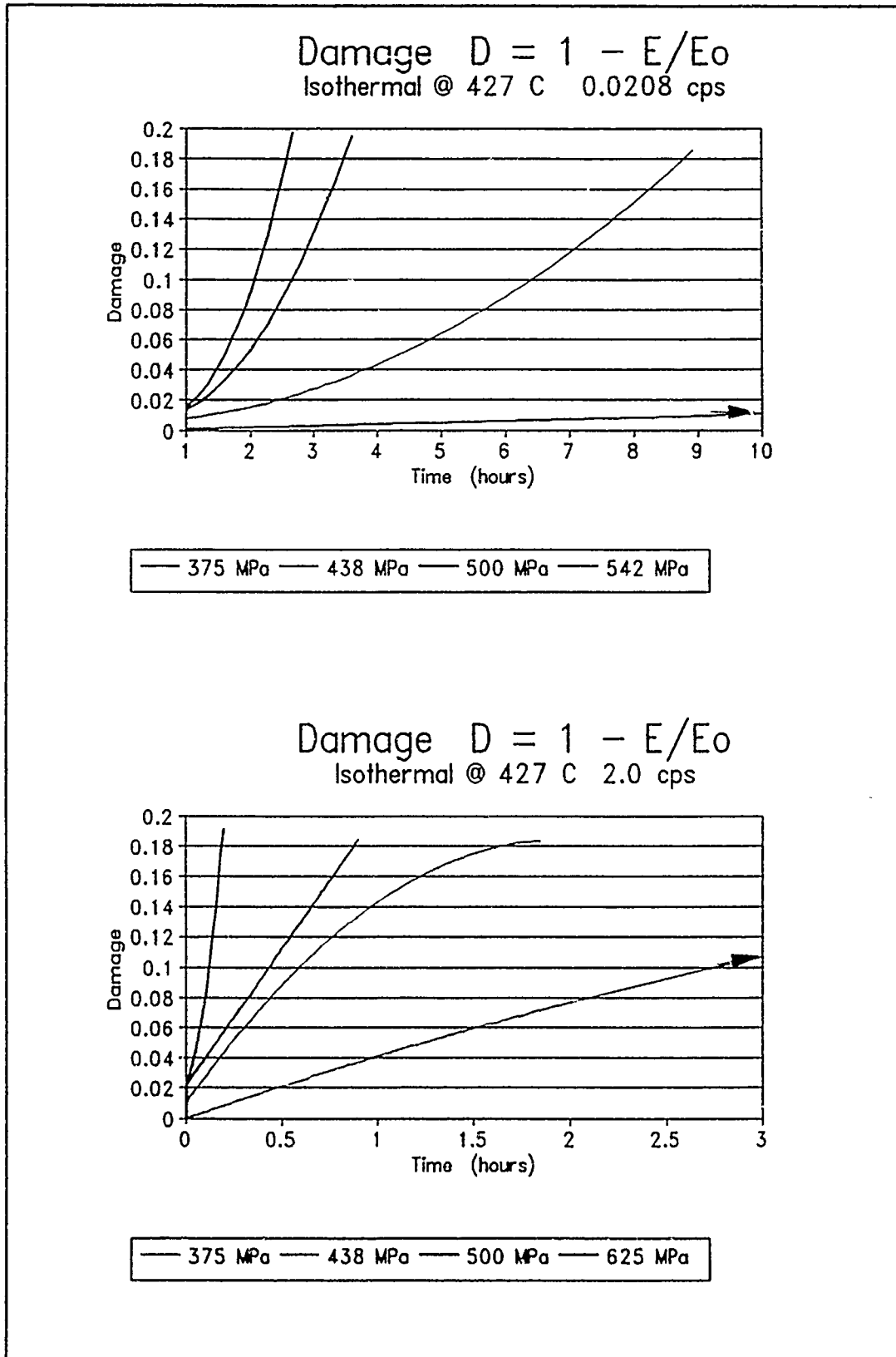


Figure 57. Specimen Fatigue Damage

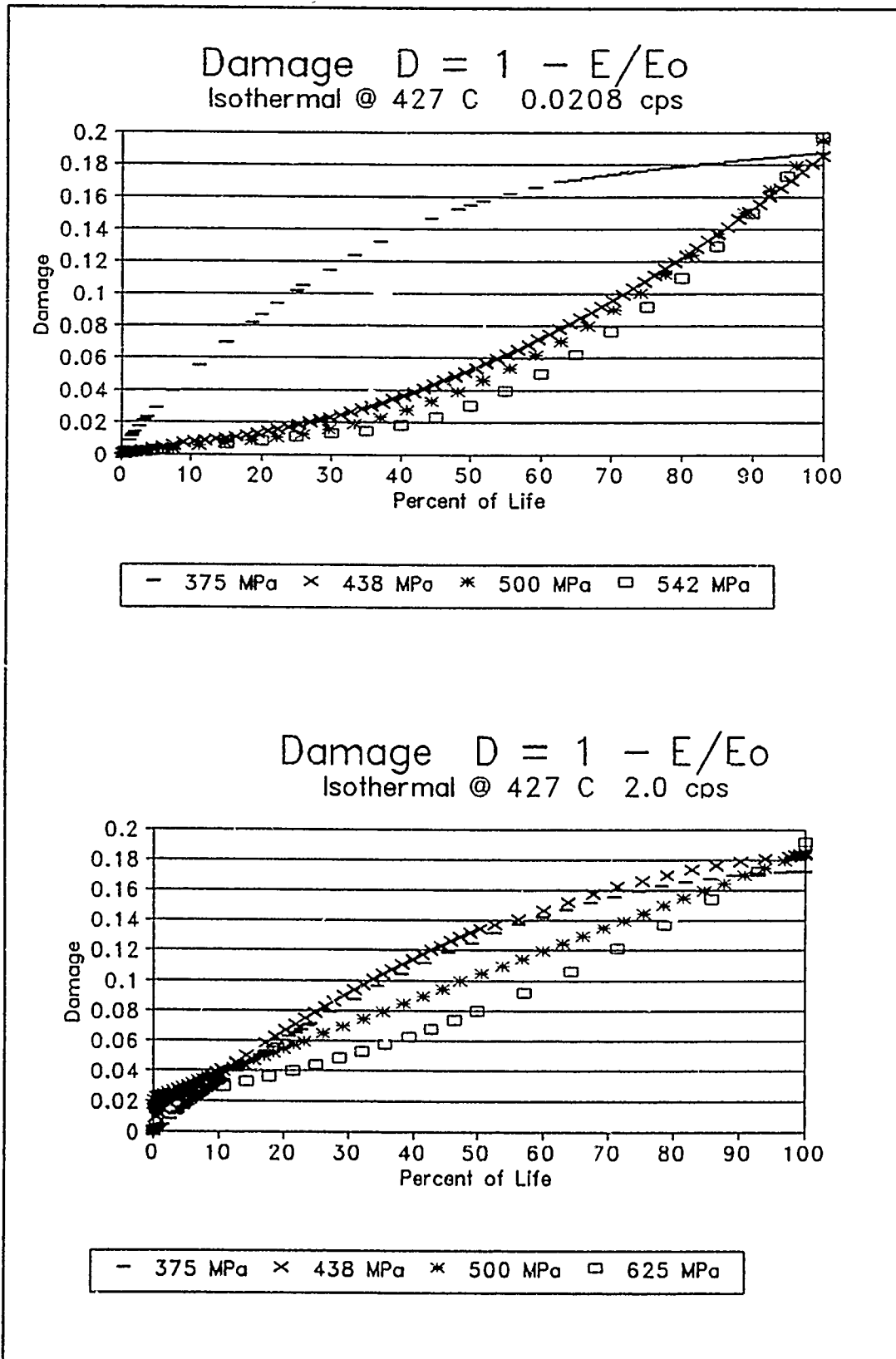


Figure 58. Specimen Fatigue Damage Based on Percent Life

(Appendix A, Figures A-1 through A-7) support this assessment. As was previously discussed, For both the 375 MPa specimens, the predominant crack initiation locations were at the 90° fiber-matrix interfaces. The cracks then progressed transversely through the matrix material.

Quite the reverse is true for the low frequency 63,72, and 542 MPa specimens. The initial low increase in damage (Figure 58) for these specimens indicate the damage mode is predominately fractured fibers with minimal transverse matrix cracking. This compares well with the microscopic and micrographic evaluation results where fractured 0° fibers, initiating matrix cracking, predominated through the life though some transverse cracking initiating off the 90° fiber-matrix interfaces did occur. Compare Figures A-5 and A-7 with Figures A-2 and A-3.

For the high frequency, 500 and 625 MPa specimens, both types of damage are common through the lives of the specimens. Thus, fractured fibers are more common at lower frequencies as compared with the higher frequencies. This was an important correlation when the strain data results of both groups of tests were evaluated. Damage initiation and progression is discussed further in the section titled *Evaluation Results*.

## *V. Conclusions and Recommendations*

Because of the statistical nature of fatigue strength and damage, a considerable number of tests are necessary to complete the characterization of fatigue behavior. This study represents a small part of what is necessary for full characterization before this particular metal matrix composite can be used in critical applications where design safety margins are minimal.

The results of this study substantiated trends in damage initiation and progression found by others who tested the same composite of different construction under similar test conditions of temperature and frequency. This study also revealed which conditions cause specific damage patterns.

One interesting comparison of previous studies shows that an endurance limit (fatigue limit) may occur at 370 MPa for the  $[0/90]_{1,1}$  lay-up. This conclusion resulted from a compilation of fatigue life data from 4 different test conditions [10 cps at ambient (7:11), 10 cps at 650°C (5:7), 2 cps at 427°C, and 0.0208 cps at 427°C] for a  $[0/90]_{1,1}$  lay-up. This would be a revelation for designers who are more comfortable with designing structures with an infinite life within this temperature range. Of course, more tests must be performed to confirm this.

Another noteworthy mention, is that the approach of using modulus degradation, based on actual test stress-strain data to determine damage modes, proved to be a viable

method of confirming the results of physical fractographic and metallographic analysis.

A summary of other results of these tests are as follows:

1. The strain at failure for each group of tests were considerably different -- representing two different failure modes. For the 2.0 cps group of tests, except for the highest stressed 625 MPa specimen, matrix failure preceded fiber failure. The strain at failure was approximately that of the maximum strain of the 0° fibers. The high frequency cycling caused the matrix to become strain hardened. The final failure mode of the matrix was primarily brittle cleavage fracture. For the 0.0208 cps group of tests, where the specimens had more exposure to temperature, fiber failure preceded matrix failure. Though the matrix did age harden considerably (due to alpha precipitates), the matrix was strained beyond the maximum 0° fiber strain. The final failure mode for these tests was due to ductile void coalescence.

2. The tensile test (at 427°C) also failed by ductile void coalescence with fiber fracture preceded by matrix failure.

3. Transverse matrix cracking initiating out of the fiber-matrix interfaces was more common with specimens cyclically stressed at the lower load levels than at the higher load levels. This trend was apparent with both

frequency groups. Although, the low frequency specimens had less transverse matrix cracking. At the higher load levels, matrix cracking initiating out of the regions of fractured fibers was more prevalent.

4. Fibers, fractured along their longitudinal axis, occurred at the highest stress levels. Fracture surface evaluations also revealed this type of damage which is possibly a mechanism to induce failure.

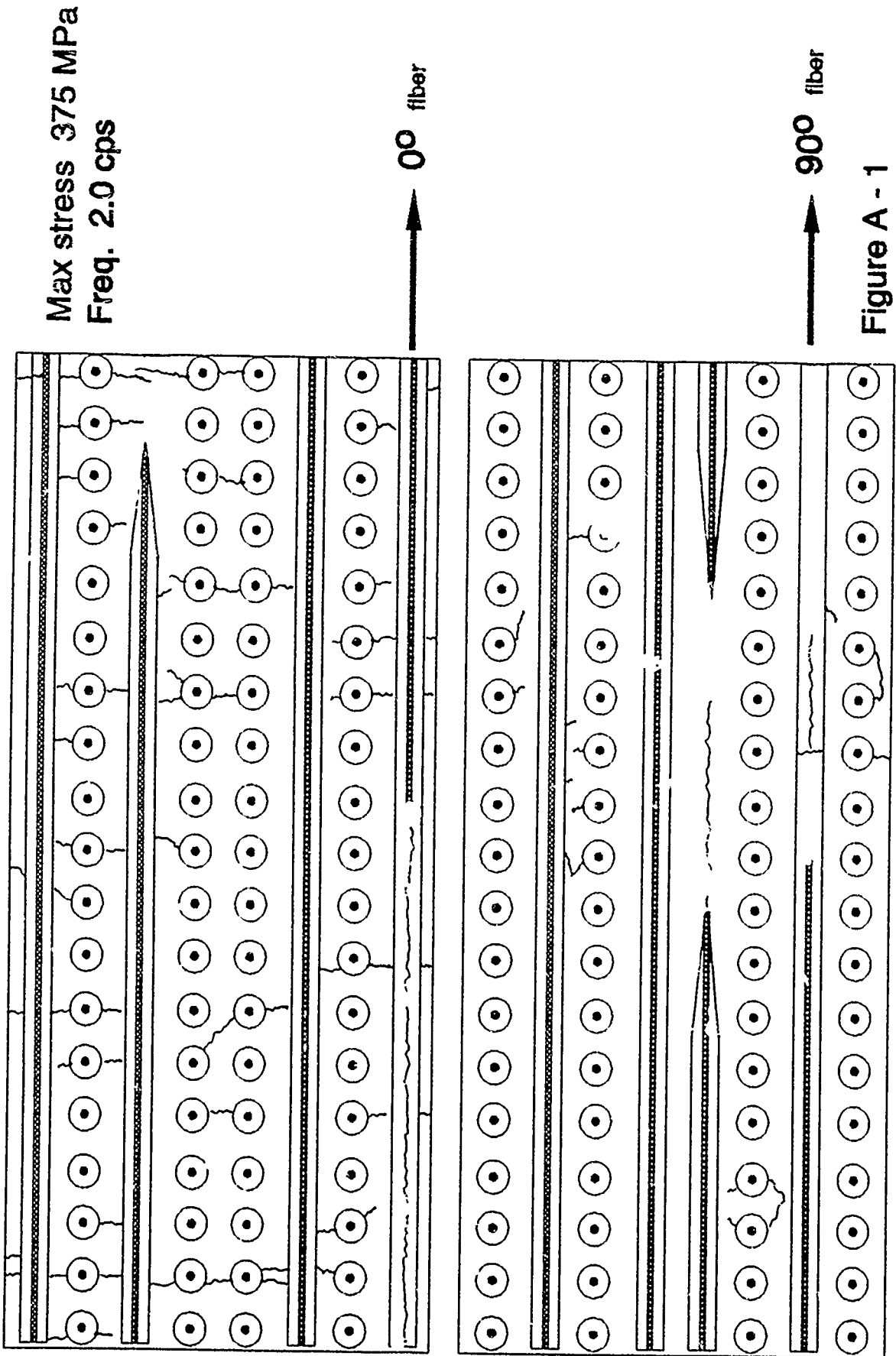
5. No evidence of ply delamination was found in any of the fatigue tested specimens.

To better understand the fatigue behavior of this material, the work hardening (due to strain hardening) aspect of the titanium matrix in a high frequency environment needs to be investigated more closely. Specimens, which are tested in the "as fabricated" condition at elevated temperatures, will undergo a phase change within the titanium matrix. This age hardening is, quite possibly, masking any strain hardening that may be taking place.

The simple solution is to test 2 groups of specimens at a moderately high frequency and temperature, say 1.0 cps at 427°C. All test conditions being the same except, of course, one group of specimens is fully aged prior to fatigue testing. Strain data and fracture surface analysis should ascertain the extent of strain hardening taking place. Fatigue damage characterization can also be done on both groups of tests to compare damage mechanisms.

*Appendix A:*

*Sectioned Surface Crack Patterns*



Max stress 438 MPa  
Freq. 2.0 cps

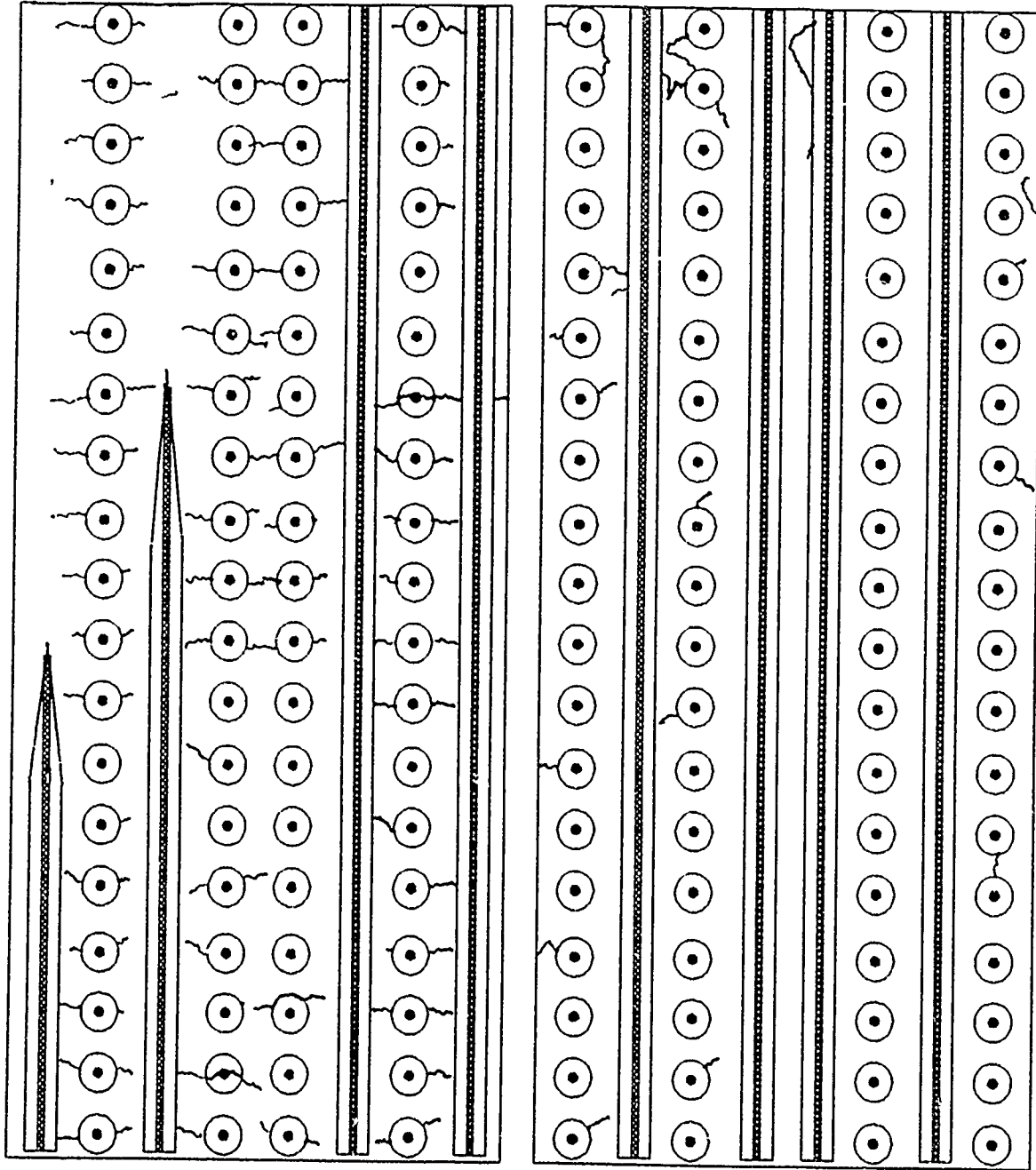
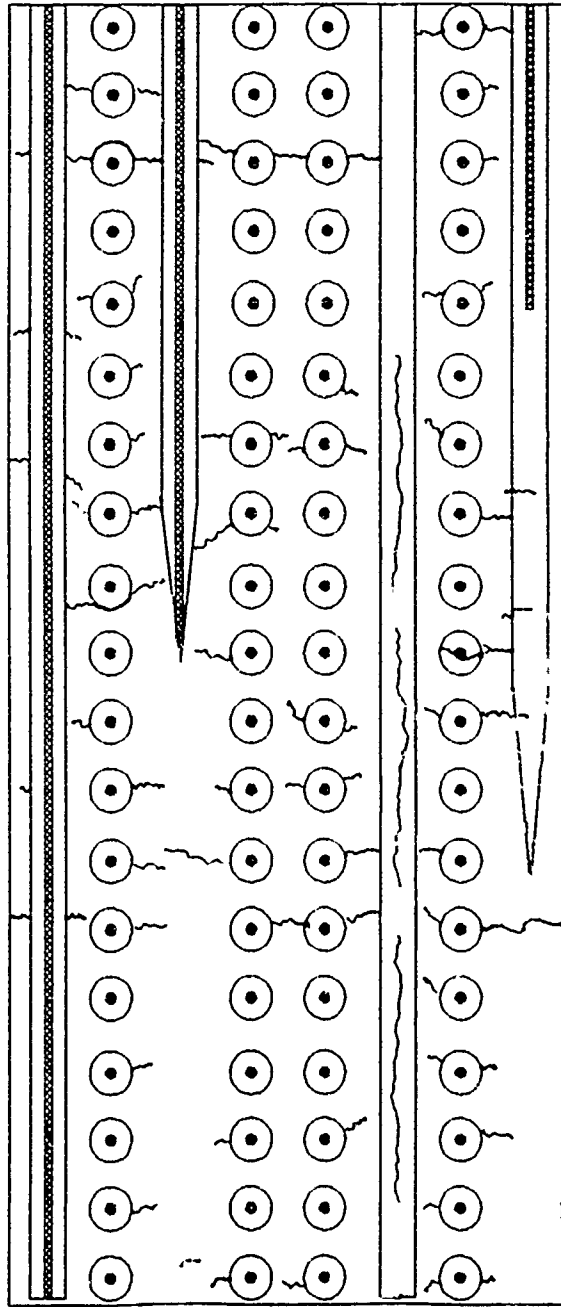


Figure A - 2

Max stress 500 MPa  
Freq. 2.0 cps

0° fiber



90° fiber

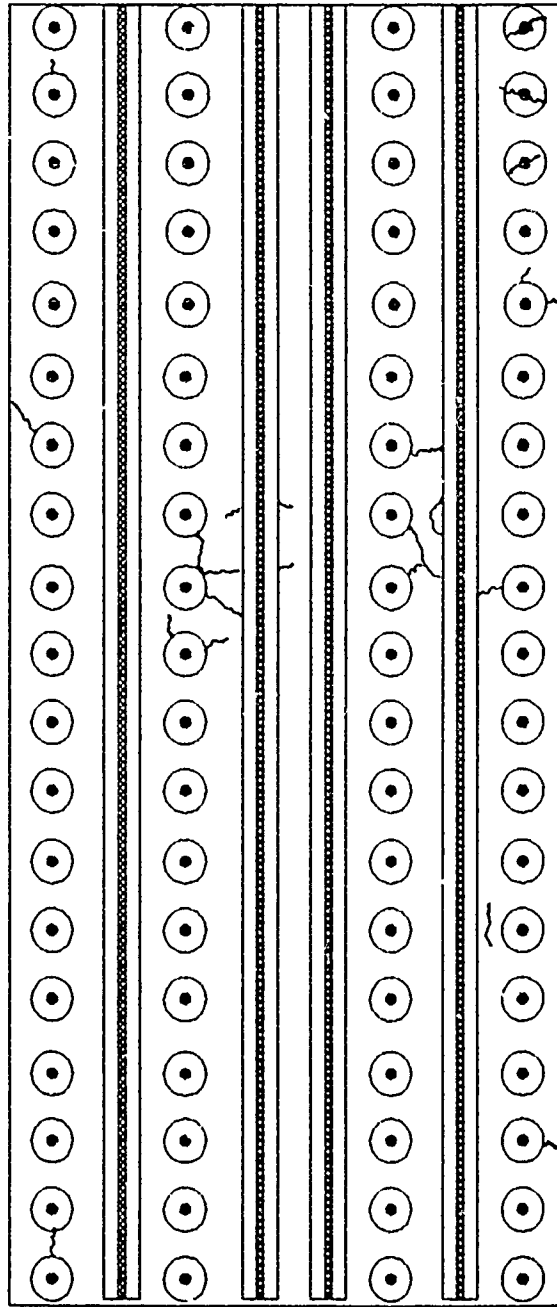
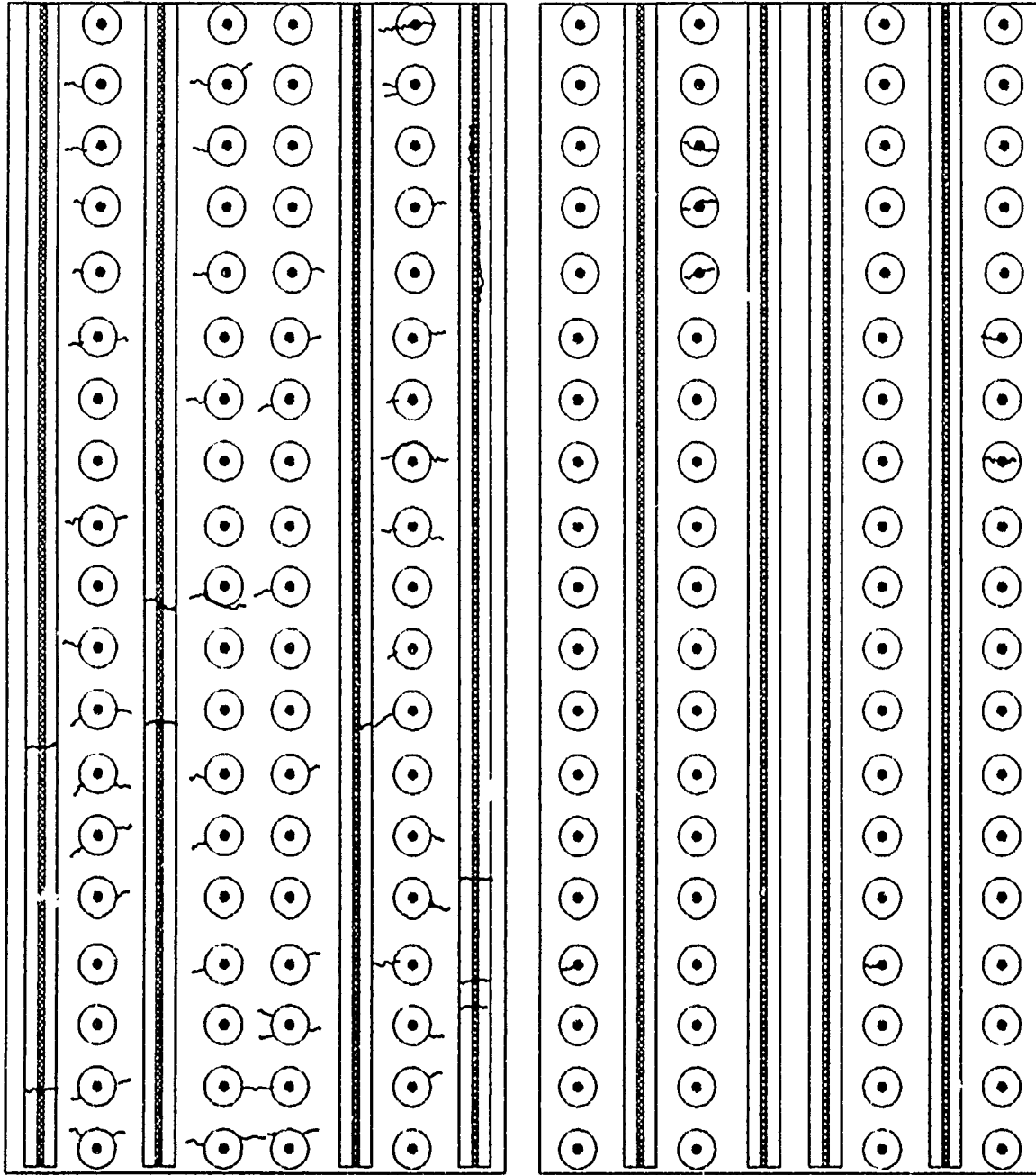


Figure A - 3

Max stress 625 MPa  
Freq. 2.0 cps

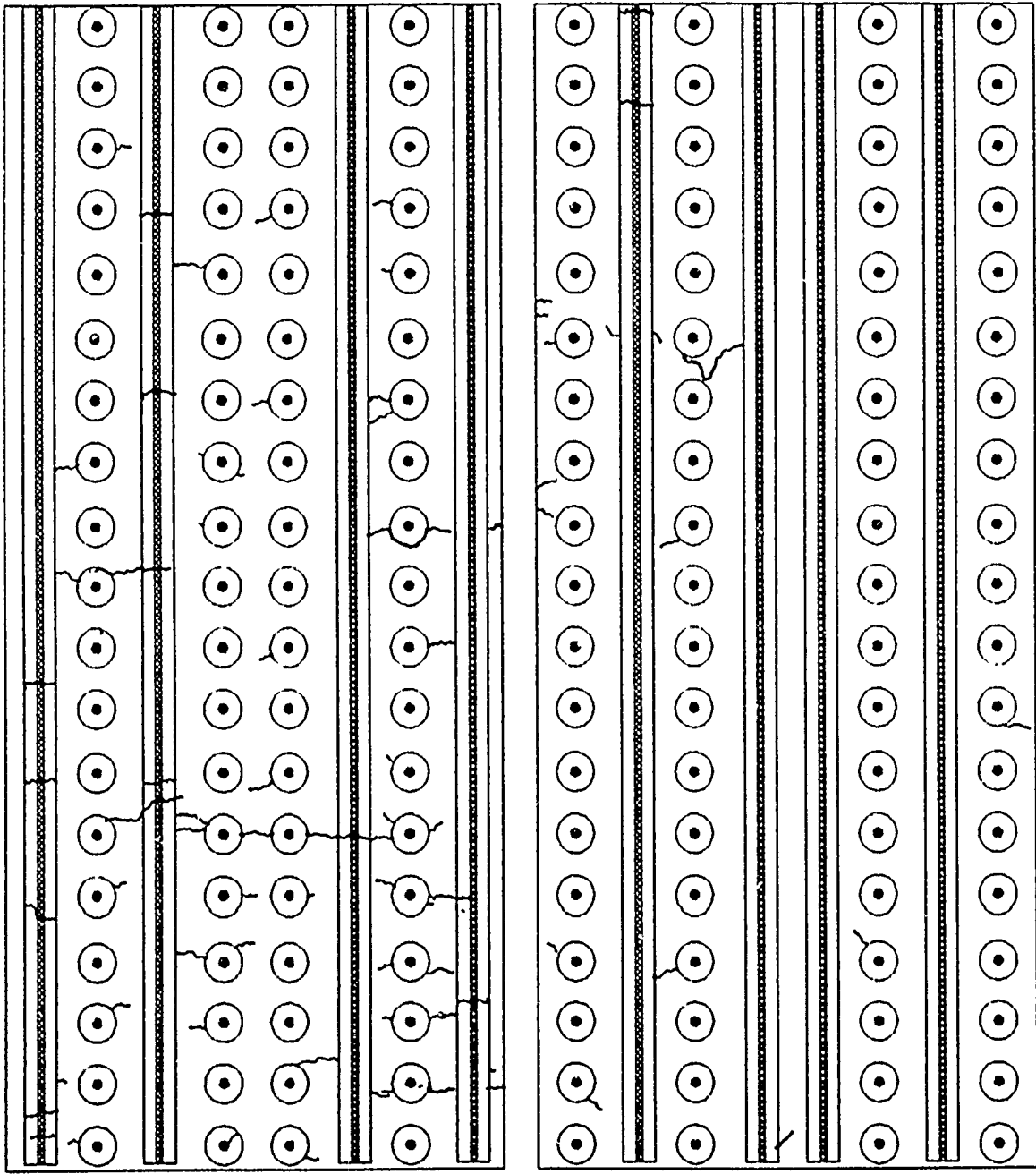


0° fiber

90° fiber

Figure A - 4

Max stress 438 MPa  
Freq. 0.0208 cps



0° fiber

90° fiber

Figure A - 5

Max stress 500 MPa

Freq. 0.0208 cps

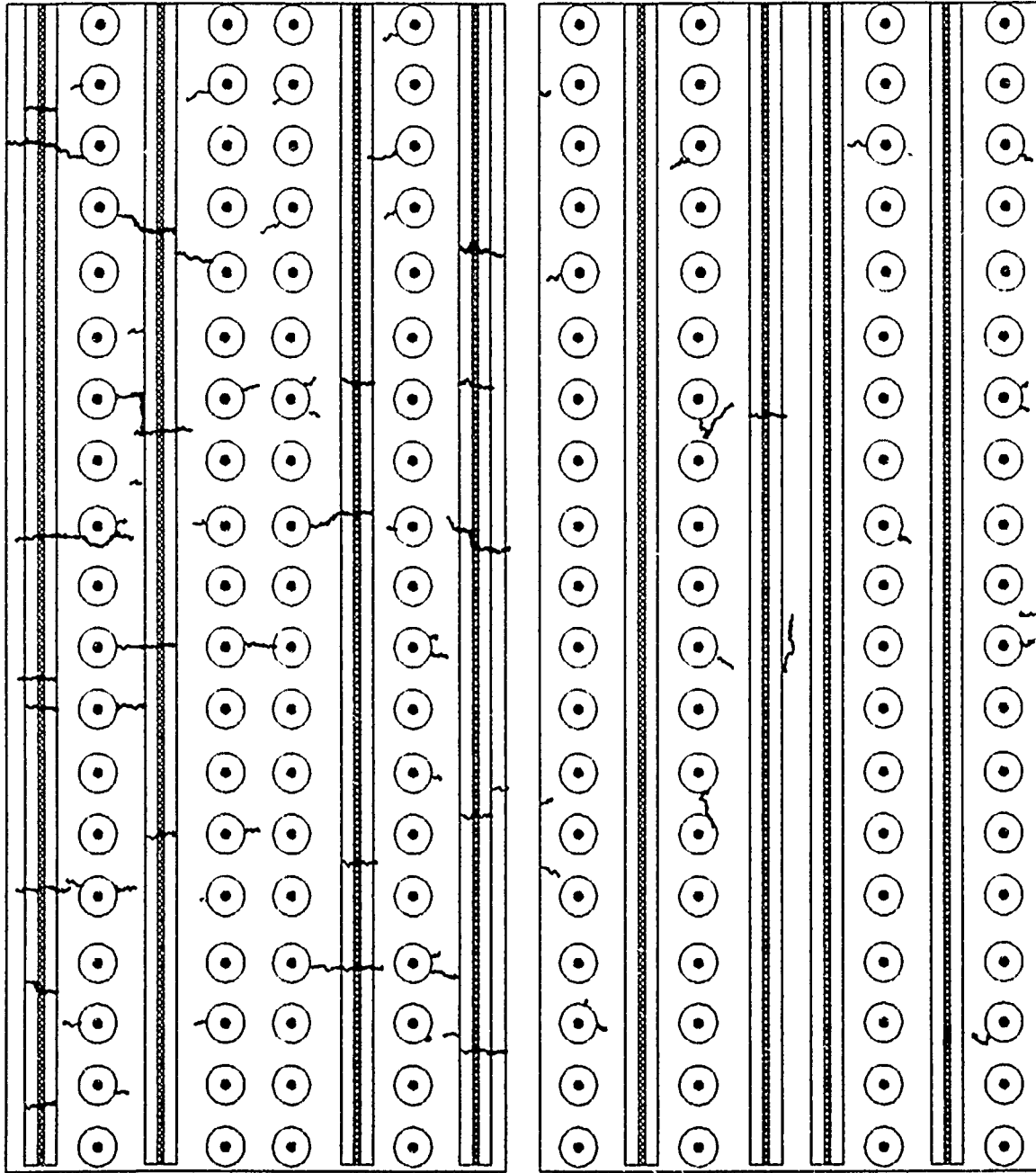
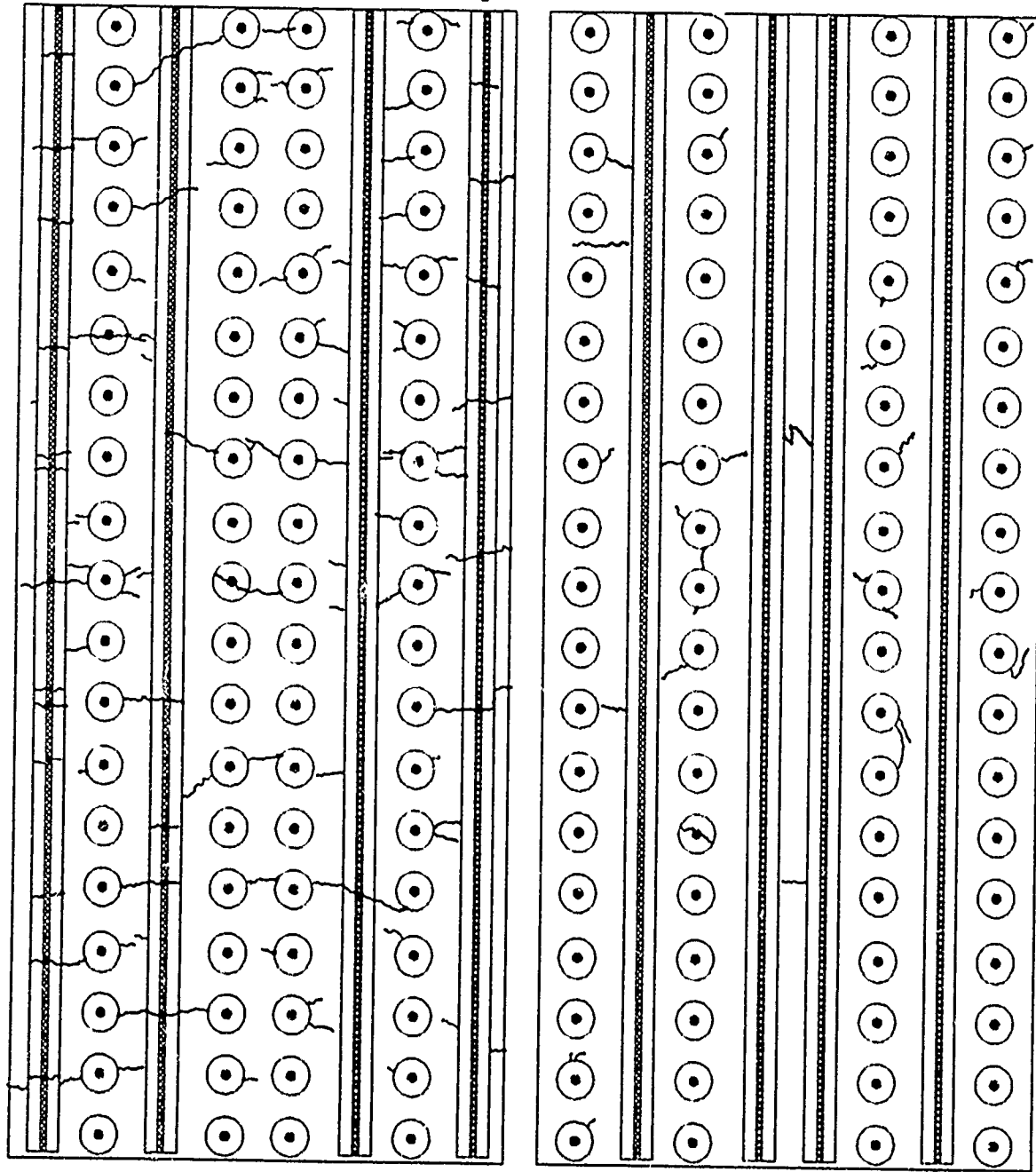


Figure A - 6

Max stress 542 MPa

Freq. 0.0208 cps



0° fiber

90° fiber

Figure A - 7

### *Bibliography*

1. Britannica, *Science and the Future*, Encyclopedia Britannica, Inc., 1990.
2. Gayda, J., Jr., Gabb, T. D., and Freed, A. D., : The Isothermal Fatigue Behavior of a Unidirectional SiC/Ti Composite and the Ti Alloy Matrix, "NASP TM-101084, April 1988.
3. Castelli, M. G., Ellis, J. R., and Bartolotta, P. A., "Thermomechanical Testing Techniques for High Temperature Composites: TMF Behavior of SiC (SCS6)/Ti-15-3," Sverdrup Technical Publication, 1990.
4. Majumdar, B. S. and Newaz, G. M., *Thermal-Mechanical Response and Damage in an Angle-Ply Metal Matrix Composite*, Submitted to the journal: Engineering Materials and Technology ASME, October 1989.
5. Pollock, W. D., and Johnson, W. S., "Characterization of Unnotched SCS6/Ti-15-3 Metal Matrix Composites at 650°C," NASP TM 102699, September 1990.
6. Agarwal, B. D. and Broutman, L. T., *Analysis and Performance of Fiber Composites*, John Wiley and Sons, New York, 1980.
7. Johnson, W. S., Lubowinski, S. J., and Highsmith, A. L., "SCS6/Ti-15-3 Metal Matrix Composites at Room Temperature," NASP TM-1014, April 1988.

8. Wawner, F. E. Jr., *Boron and Silicon Carbide/Carbon Fibers*, Fiber Reinforcements for Composite Materials, Ed. Bunsell, A. R., Elsevier Science Publishers, Amsterdam, The Netherlands, 1988.
9. Harmon, D. M., Saff, C. R., and Sun, C. T., "Durability of Continuous Fiber Reinforced Metal Matrix Composites," *AFWAL-TR-87-3030*, October 1987.
10. Ermer, P. G., *Investigation of the Failure Modes in a Metal Matrix Composite Under Thermal Cycling*. MS Thesis, AFIT/GAE/AA/89D, School of Engineering, Air Force Institute of Technology (AU), Wright-Patterson AFB, Ohio, December 1989.
11. Jones, R. M., *Mechanics of Composite Materials*, Hemisphere Publishing Corporation, New York, 1975.
12. Rogacki, J. and Tuttle, M., *Thermoviscoplastic Behavior of SCS6/Ti Metal Matrix Composites*. Unknown.

REPORT DOCUMENTATION PAGE			Form Approved OMB No. 0704-0188	
Public reporting burden for this collection of information is estimated to average 1 hour per response, including the time for reviewing instructions, searching existing data sources, gathering and maintaining the data needed, and completing and reviewing the collection of information. Send comments regarding this burden estimate or any other aspect of this collection of information, including suggestions for reducing this burden, to Washington Headquarters Services, Directorate for Information Operations and Reports, 1215 Jefferson Davis Highway, Suite 1204 Arlington, VA 22202-4302, and to the Office of Management and Budget, Paperwork Reduction Project (0704-0188), Washington, DC 20503				
1. AGENCY USE ONLY (Leave blank)	2. REPORT DATE December 1990	3. REPORT TYPE AND DATES COVERED Master's Thesis		
4. TITLE AND SUBTITLE INVESTIGATION OF FATIGUE DAMAGE MECHANISMS IN A METAL MATRIX COMPOSITE UNDER ELEVATED TEMPERATURES			5. FUNDING NUMBERS	
6. AUTHOR(S) Barry D. Portner, Captain, USAF				
7. PERFORMING ORGANIZATION NAME(S) AND ADDRESS(ES) Air Force Institute of Technology, WPAFB OH 45433-6583			8. PERFORMING ORGANIZATION REPORT NUMBER AFIT/GAE/ENY/90D-20	
WRDC/POTC Mr. Fecke Wright-Patterson AFB Oh 45433			10. SPONSORING/MONITORING AGENCY REPORT NUMBER	
11. SUPPLEMENTARY NOTES				
12a. DISTRIBUTION / AVAILABILITY STATEMENT Approved for public release: distribution unlimited			12b. DISTRIBUTION CODE	
13. ABSTRACT (Maximum 200 words) This study investigated the fatigue damage initiation and progression in SCS-6/Ti-15-3 under an environment of fatigue loading at isothermal temperature. This program included two parts. First, an 808 Ultimate Tensile Strength system was set up to accommodate testing at two frequencies of 2.0 and 0.0208 cps at a constant temperature of 427°C. Second, at intervals during the load cycle process, the test specimens were characterized by establishing damage parameters based on changing modulus of elasticity, average strain, strain range, and ultimate tensile strength. Damage progression was documented in the form of failure of the fiber-matrix interface, matrix cracking, fiber breaking, and debonding of the fibers. Crack initiation locations and growth patterns were peculiar to specific test conditions of frequency and stress level. Also, analysis of the fatigued specimens and test data revealed matrix failure mechanisms ranging from ductile failure to cleavage fracture. The results of this study clearly show that temperature, frequency as well as stress levels are important design considerations for this composite in fatigue loading applications. <i>Keywords</i>				
14. SUBJECT TERMS Fatigue, Damage, Failure, Strain, Stress, Composites, Cracks, Fracture, <i>Theses (T&amp;D)</i>			15. NUMBER OF PAGES 115	16. PRICE CODE
17. SECURITY CLASSIFICATION OF REPORT Unclassified	18. SECURITY CLASSIFICATION OF THIS PAGE Unclassified	19. SECURITY CLASSIFICATION OF ABSTRACT Unclassified	20. LIMITATION OF ABSTRACT UL	